

Marie Mathiasson

NTNU
Norwegian University of
Science and Technology
Faculty of Engineering
Department of Mechanical and Industrial Engineering

Marie Mathiasson

An In-Depth Analysis of the Bond Strength of a Dissimilar Al-Fe HYB (Hybrid Metal Extrusion & Bonding) Joint

June 2019



Norwegian University of
Science and Technology

An In-Depth Analysis of the Bond Strength of a Dissimilar Al-Fe HYB (Hybrid Metal Extrusion & Bonding) Joint

Marie Mathiasson

Mechanical Engineering

Submission date: June 2019

Supervisor: Filippo Berto

Co-supervisor: Lise Sandnes & Øystein Grong

Norwegian University of Science and Technology
Department of Mechanical and Industrial Engineering

Preface

The present master thesis is written during the spring of 2019 in accordance with the requirements for a Master of Science, MSc, in Mechanical Engineering at the Norwegian University of Science and Technology (NTNU) in Trondheim, Norway. The report is carried out at the Department of Mechanical and Industrial Engineering (MTP) within the specialization field Product Development and Materials Engineering. The research project is supervised by Professor Filippo Berto and linked up to the company HyBond AS.

Marie Mathiasson
Trondheim, 2019-06-11

Abstract

The patented Hybrid Metal Extrusion & Bonding (HYB) process enables joining of aluminium and steel components by the use of filler material addition in the solid state. In the present report, an in-depth analysis of the bond strength and structural integrity of a 4 mm AA6082-T6 and S355 butt weld produced using this method is given. The experimental trial includes tensile testing using digital image correlation (DIC) analysis, microscopic examination of the joint and the base materials, together with scanning electron microscope (SEM) examination of the bond line and selected fracture surfaces. In addition, a more extensive finite element (FE) model has, for the first time, been developed to simulate the behavior of the weld during tensile testing.

The main results from the DIC analysis revealed that most of the principal strains in the specimen during tensile testing start to concentrate in the heat-affected zone (HAZ). However, a root crack is gradually forming in the root region at the aluminium-steel interface due to insufficient bonding in this region, causing a competition between the two weak zones (i.e., the HAZ and root crack) before final fracture occurs along the aluminium-steel interface. Despite of this, a relatively high joint efficiency of 75% is reached. From the FE simulations, it was found that the insufficiently bonded region in the root has a depth of about 0.03 mm and that it does not compromise the overall joint strength significantly. Moreover, a potential strength contribution caused by mechanical interlocking was observed. From this, it is concluded that the HYB process is well suited for dissimilar welding of aluminium and steel. However, there is a need for further optimization of the process in order to reach the forefront of aluminium-steel welding technology. This work is now in progress.

Sammendrag

Den patenterte Hybrid Metal Extrusion & Bonding (HYB) sveiseprosessen muliggjør sammenføyning av aluminium og stålkomponenter ved bruk av tilsettmateriale og plastisk deformasjon i fast fase. I denne rapporten er det gitt en grundig analyse av bindestyrken og den strukturelle integriteten til en 4 mm AA6082-T6 og S355 buttsveis, produsert ved hjelp av denne metoden. De eksperimentelle forsøkene inkluderer DIC-analyse (eng: digital image correlation analysis) og mikroskopiske undersøkelser av grunnmaterialene og sveisen. SEM (eng: scanning electron microscope) har også blitt benyttet for å se på utvalgte bruddflater og bindingen mellom stål og aluminium. I tillegg har en omfattende FE (eng: finite element) modell blitt utviklet for å simulere sveisens oppførsel under strekkprøving, noe som aldri har blitt gjennomført tidligere.

Resultatene fra DIC-analysen viste at tøyningene hovedsakelig samlet seg i den varmpåvirkede sonen under strekkprøving. En rotsprekk oppsto imidlertid under testingen i overgangen mellom aluminiumet og stålet på grunn av utilstrekkelig binding i dette området. Det oppstod en konkurranse mellom de to svake områdene, før bruddet gikk langs grensesnittet mellom aluminium og stål. Til tross for sprekken oppnådde sveisen en høy styrke på 75% av styrken til aluminium grunnmateriale. Fra FE-simuleringen ble det oppdaget at området med dårlig binding er på omtrent 0.03 mm, og at dette området ikke har en stor påvirkning på den resulterende styrken til sveisen. Videre ble det også observert et potensielt styrkebidrag fra mekanisk låsing. Fra dette kan det konkluderes med at HYB prosessen er godt egnet for sveising av aluminium og stål. Det er imidlertid et behov for ytterligere videreutvikling og optimalisering av prosessen for å bli fremtidens sveiseprosess for aluminium og stål. Dette arbeidet er nå påbegynt.

Acknowledgment

I would like to express my gratitude to my supervisor Filippo Berto, Professor at the Department of Mechanical and Industrial Engineering NTNU, for his contributions and encouragement throughout the work of this master thesis. I appreciate you giving me the freedom to shape the task myself, but also guiding me through, and discuss problems that arose.

I also especially want to thank my co-supervisor Lise Sandnes. Your door is always open, and I am so grateful for your excellent support and guidance during the last year. Several hours of valuable consulting and discussion, and help with the experimental work have been of great value for this research project.

Additional appreciations go to Profeser Øystein Grong, the founder of HyBond AS, for all information provided regarding the HYB technology. Your insight and information have been of great importance for the writing of the report. Finally, I would like to thank the OPTIMALS research project (Optimal design and production of lightweight and high-performance aluminium-steel structural components) for including me in their meetings and taking the time to discuss challenges that came up during the scope of the project.

Contents

Preface	i
Abstract	iii
Sammendrag	v
Acknowledgement	vii
List of Figures	xii
List of Tables	xix
Abbreviations	1
1 Introduction	2
1.1 Motivation	2
1.2 Objectives	3
1.3 Scope	4
2 Theory and literature review	6
2.1 Aluminium alloys	6
2.1.1 Overview	6
2.1.2 Al-Mg-Si alloys	6
2.1.3 Welding of Al-Mg-Si alloys	8
2.2 Steel	8
2.2.1 Overview	8
2.2.2 High-strength low-alloy (HSLA) steel	9
2.2.3 Welding of HSLA steel	9
2.3 Welding of dissimilar metals	10
2.3.1 An introduction	10
2.3.2 Bonding mechanisms in dissimilar weldments	12
2.3.3 Metallic bonding	12
2.3.4 Intermetallic bonding	13
2.4 Conventional welding techniques used for joining of aluminium and steel	15
2.4.1 Challenges related to dissimilar joining of aluminium and steel	15
2.4.2 Fusion welding	16
2.4.3 Solid-state welding	21
2.5 The Hybrid Metal Extrusion & Bonding (HYB) process	25
2.5.1 Principles behind the HYB technology	25
2.5.2 The HYB PinPoint extruder	26
2.6 Using the HYB process for dissimilar joining	28

2.6.1	Introduction to dissimilar joining	28
2.6.2	Working principle during aluminium-steel joining	28
2.6.3	Mechanical characterization of the first aluminium-steel HYB butt weld	29
2.7	Digital image correlation (DIC) analysis	32
3	Experimental	34
3.1	Materials	34
3.1.1	Base materials (BM)	34
3.1.2	Filler material (FM)	34
3.2	Welding conditions	35
3.3	Sample preparation and metallographic examination	36
3.3.1	Sample sectioning	36
3.3.2	Sample preparation	37
3.3.3	Optical microscopy	38
3.4	Scanning electron microscope (SEM)	38
3.5	Tensile testing	39
3.6	DIC analyses	40
4	Results	42
4.1	Microscopic examination	42
4.1.1	Base materials	42
4.1.2	The HYB joint macrostructure	42
4.1.3	The HYB joint microstructure	44
4.2	Examination of the Al-Fe interface	46
4.3	Tensile properties	48
4.3.1	Global properties of the dissimilar HYB joint	48
4.3.2	Local properties of the HAZ	49
4.4	DIC analysis of the tensile specimens	51
4.5	Fractography of tensile specimens	54
5	Numerical simulation	58
5.1	Introduction to the finite element method (FEM)	58
5.2	Set-up for finite element (FE) model of tensile testing	59
5.2.1	Part creation and material properties	59
5.2.2	Damage initiation and evolution	61
5.2.3	Boundary conditions, loads and constraints	64
5.2.4	Partitioning	65
5.2.5	Mesh	66
5.3	Discussion of simulation approach	68

6	Discussion	72
6.1	Introduction	72
6.2	Comparison of the mechanical properties of dissimilar Al-Fe friction stir (FS) and HYB weldments	72
6.3	Intermetallic layer thickness and Al-Fe interface configuration	73
6.3.1	Effect of IMP layer thickness	73
6.3.2	Effect of Al-Fe interface configuration	76
6.4	The significance of a root crack in the Al-Fe HYB joint	77
6.4.1	Validation of the FE model	77
6.4.2	Effect of the root crack size on the joint strength	78
6.4.3	Evaluating the root crack problem	80
6.4.4	Comparison of experimental and simulated crack propagation and strain concentration during tensile testing	82
6.5	Improvements and current status of the HYB process for joining aluminium and steel	85
7	Conclusion	87
7.1	Concluding Remarks	87
7.2	Recommendations for Further Work	88
	References	90
	Appendices	I
A	Material certificates	I
B	Results obtained from Matteo Manfrotto	II
C	Additional images of observed defects and steel fragments in the Al-Fe HYB joint	III
D	Tensile properties	IV
D.1	Global properties of the dissimilar Al-Fe HYB joint.	IV
D.2	Local properties of the HAZ	V
D.3	Interaction between the different weld zones.	VII
E	Additional BSE images of the Al-Fe bond line	VIII
F	Additional SEM fractographs	IX
G	Additional BSE fractographs	X
H	Study of crack positioning and crack domain in the FE analysis	XI
I	Simulated crack propagation and strain concentration of the Al-Fe HYB joint during tensile testing	XII
J	Risk assessment	XIV

List of Figures

2.1	The strength evolution during aging of Al-Mg-Si alloys. Copied from [10].	7
2.2	Participates forms a barrier to dislocation movement, the dislocations can pass through them by (a) bowing or (b) cutting. Copied from [22].	7
2.3	Honda Accord front subfram using friction stir lap welding (FSLW) of die cast aluminium and press formed steel. Copied from [6]. . . .	11
2.4	Depending on which joining technique that is used, different interfaces and bonding mechanisms can be observed. (a) illustrates the two interfaces that will form by the use of a filler material addition between BM1 and BM2, while (b) shows the one interface that appears by directly bonding the two metals.	12
2.5	Illustration of metallic bonding. Copied from [16].	13
2.6	A comparison of the atomic structure of aluminium (Al) and iron (Fe) [16]. The high degree of incompatibility between the atomic structures makes the sharing of valence electrons difficult.	14
2.7	Fe-Al binary equilibrium phase diagram. Copied from [30].	14
2.8	Comparison of thermal properties of steel and aluminum, and specific challenges involved in welding and fabrication of Al-Fe products (Ø.Grong, Personal Communication, 2019).	15
2.9	Schematic illustration of the Cold Metal Transfer (CMT) welding assembly for a dissimilar Al-Fe lap joint. Copied from [40].	18
2.10	Intermetallic phase (IMP) layers observed in Cold Metal Transfer(CMT) lap joint of (a) AA5754 and EN10143 (copied from [3]) and (b) AA6061 and galvanized boron steel (copied from [38])	19
2.11	Fracture initiation at the weld root due to faulty fusion in a Cold Metal Transfer (CMT) lap joint produced of AA6061-T6 and galvanized boron steel. Copied from [38].	20
2.12	Schematic illustration of the Friction Stir Welding (FSW) process for butt joining of aluminium and steel plates. Copied from [50]. . .	21
2.13	Intermetallic phase (IMP) layers observed in friction stir (FS) butt welds of (a) AA5052 and HSLA steel (copied from [47]) and (b) AA6061 and 304 stainless steel (copied form [52]).	23
2.14	Tunnel defects and pores observed in the stir zone (SZ) and along the Al-Fe interface of a friction stir (FS) weld produced of AA 5186 and mild steel. Copied from [54].	24
2.15	Schematic illustration of continuous extrusion. Copied from [36]. . .	26
2.16	Illustration of the main components in the HYB PinPoint extruder. Copied from [11].	27

2.17	A dissimilar Al-Fe butt joint produced with the HYB process. The separate die on the housing makes it possible to control the shape of the weld face. Copied from [56].	27
2.18	Schematic illustration of the pin and its location in the weld groove during production of the first HYB Al-Fe butt weld. Copied from [13].	28
2.19	Transverse hardness profile of the mid-section of the first produced HYB butt weld of aluminium and steel. Copied from [13].	30
2.20	Optical macrograph of the cross-section of the first produced Al-Fe HYB butt joint, showing the material flow of the aluminium base and filler material. Copied from [13].	31
2.21	Tensile strength measured for the four tensile specimens tested of the first dissimilar HYB butt weld of aluminium and steel. Data extracted from [57].	31
2.22	The fracture path in (a) the broken tensile specimen and (b) its location in the EZ in the first produced Al-fe HYB butt weld. Copied from [13].	32
2.23	The principle of digital image correlation (DIC). Copied from [59].	33
2.24	A Q4 element within a mesh using the "finite-element" based digital image correlation (DIC) approach. Copied from [60].	33
3.1	Schematic illustration of one of the base material plates used in the HYB joining trial, including both the plate dimensions and welding/rolling direction. Note that, the illustration is representative for both base material plates used in the joining trial.	35
3.2	Schematic illustration of the (a) surface preparation and groove configuration prior to the welding operation, and (b) pin-in-groove situation during welding.	36
3.3	Schematic illustration of the plate sectioning and numbering of the specimens. The specimens used for the microscopical examination are highlighted in pink.	37
3.4	Schematic illustration of specimen location and numbering of the tested tensile specimens.	39
3.5	Photographs of selected tensile specimens prior to testing (a) flush-machined and (b) as-welded.	39
3.6	Pictures of the experimental set-up used for DIC testing. Note that, specimen S4 is tested with the steel side on top [14].	40
3.7	Photograph of specimen S4 showing the applied mesh and the two virtual extensometers used to analyse the tensile test data.	41

3.8	(a) The HYB joint transverse hardness profile measured along the horizontal midsection of the joint [14]. (b) Photograph of specimen S8 showing the location of the virtual extensometers used to extract local tensile properties from the heat affected zone (HAZ).	41
4.1	Optical micrographs showing the microstructure of the base materials used in the welding trial taken transverse to the plate rolling direction. (a) The AA6082-T6 at low magnification (2.5x) and (b) the S355 at high magnification (2000x).	42
4.2	Optical macrograph showing an overview of the Al-Fe HYB joint macrostructure.	43
4.3	Optical micrographs showing the two different types of bond-lines that occur in the Al-Fe HYB joint. (a) Bonding between the aluminium base and filler material, and (b) dissimilar bonding between the aluminium filler material and the steel.	43
4.4	Optical micrograph showing an overview of the Al-Fe HYB joint transverse microstructure of specimen S6. Note that, only the microstructure of the aluminium is visible.	44
4.5	Optical micrograph showing the microstructure of the steel side of the Al-Fe HYB joint of specimen S11 at high magnification (2000x).	44
4.6	Optical micrographs showing an observed (a) tunnel defect and (b) steel fragments in the Al-Fe HYB weld.	45
4.7	Low magnification (50x) overview of the Al-Fe bond line of the HYB joint taken in the weld center.	46
4.8	BSE micrographs at high magnification (2000x) showing the (a) top, (b) bottom and (c) middle part of the Al-Fe bond line of the HYB joint.	47
4.9	BSE micrograph at high magnification (5000x) of the central part of the Al-Fe bond line of the HYB joint.	47
4.10	Measured stress-strain curves from the tensile testing using DIC and virtual extensometers.	48
4.11	Measured average tensile properties for the three Al-Fe HYB tensile specimens. The aluminum base material properties are obtained from Sandnes [50].	49
4.12	Example of measured stress-strain curves during tensile testing of specimen 2 with extensometers positioned in the HAZ.	50
4.13	Illustration of the positioning of the virtual extensometers in the aluminium BM, HAZ/EZ, and steel BM.	50
4.14	Example of measured stress-strain curves during tensile testing of specimen 8, for extensometers positioned in the aluminium BM, EZ/HAZ and steel BM.	51

4.15	Fracture propagation of specimen 2 at different stages during tensile testing; (a) before loading, (b) at the point of crack initiation and (c) final fracture.	52
4.16	Evolution of the strain localization during tensile testing of specimen 2.	52
4.17	Fracture propagation of specimen 4 at different stages during tensile testing; (a) before loading, (b) at the point of crack initiation and (c) final fracture.	53
4.18	Evolution of the strain localization during tensile testing of specimen 4.	53
4.19	Fracture propagation of specimen 8 at different stages during tensile testing; (a) before loading, (b) at the point of crack initiation and (c) final fracture.	54
4.20	Evolution of the strain localization during tensile testing of specimen 8.	54
4.21	Schematic illustration of the position where a significant layer of aluminium was detected on the steel fracture surface.	55
4.22	SEM overview micrographs at low magnification (25x) showing the steel fracture surfaces of specimen (a) 4 and (b) 8.	55
4.23	SEM micrographs showing close-ups at high magnification (5000x) of the (a) lower and (b) upper part of the steel fracture surface of specimen 4.	56
4.24	BSE micrographs at low magnification (100x) showing the (a) lower and (b) upper part of the steel fracture surface of specimen 2.	57
4.25	BSE micrographs at high magnification (2000x) showing the (a) lower and (b) upper part of the steel fracture surface of specimen 2.	57
5.1	Some element families commonly used in Abaqus. Copied from [15].	58
5.2	Illustration of the materials assigned to the different regions of the finite element (FE) model. Note that the width of the HAZ/EZ is set to 10.5 mm.	59
5.3	Stress-strain curves showing the true stress and true plastic strain for the different zones in the Al-Fe HYB joint, used as input for the material plasticity in the finite element (FE) model.	60
5.4	Illustration of the crack positioning and crack domain in the finite element (FE) model of the Al-Fe HYB joint.	62
5.5	Illustration of the linear damage evolution criterion based on fracture energy. Copied from [15].	64
5.6	To simulate the experimental set-up of the tensile testing (a) boundary conditions, (b) load and (c) a coupling constraint were applied to the finite element (FE) model.	65
5.7	Illustration of the partitioning of the finite element (FE) model.	65

5.8	Principal strains in the finite element (FE) model used for verification of mesh size (a) with and (b) without an initial crack.	67
5.9	Mesh sensitivity analysis of finite element (FE) model.	68
5.10	Mesh of the finite element (FE) model in a) the thickness and b) the length direction.	68
6.1	Comparison of the joint efficiency in different friction stir (FS) welds relative to the one obtained for the HYB process.	73
6.2	Graphical illustration of the intermetallic layer thickness formation relative to the heat input during joining (based on the tool rotation speed) and the corresponding tensile strength of the joint [47]. . . .	74
6.3	Low magnification micrographs showing the Al-Fe interface in different types of weldments. a) CMT [3], b) FSW [47] and c) HYB. . .	75
6.4	TEM micrograph showing the HYB joint intermetallic layer thickness. Copied from [70].	75
6.5	Illustration of the weld groove configuration and material flow in the dissimilar Al-Fe HYB joint.	76
6.6	SEM micrograph of the rough Al-Fe interface in the lower part of the HYB joint.	77
6.7	Comparison of simulated (dashed line) and measured (solid line) engineering stress strain curves for the Al-Fe HYB joint.	78
6.8	Master plot showing the force-displacement behavior of the simulated Al-Fe HYB joint. The black curve represents the behavior of the weld without any root crack, whereas the colored curves show the behavior of the joint when introducing a crack having an initial depth of 0.03 to 1.2 mm.	79
6.9	Comparison of simulated force-displacement curves (dashed lines) with the measured curve (solid line) from the DIC testing of the Al-Fe HYB joint.	81
6.10	(a) The force-displacement curve for specimen 2, indicating at which force and displacement the crack was first initiated during tensile testing. (b) Photograph of the first visible observation of the root crack developing during tensile testing of specimen 2.	82
6.11	Crack path of the simulated Al-Fe HYB joint containing a crack size equal to (a) 0.06 mm and (b) 0.4 mm	83
6.12	Evolution of strain localization and distribution during simulation of the Al-Fe HYB joint with a crack size equal to 0.4 mm. The scaling factor for deformation is set to 1 in the visualization.	84
6.13	Evolution of the strain localization during tensile testing of specimen 2.	84

6.14	Schematic illustration of the pin and its location in the different weld grooves for (a) the first and (b) the second produced Al-Fe HYB butt weld.	85
6.15	Schematic illustration of the pin and its location in the weld groove of the third produced Al-Fe HYB butt weld.	86
A.1	Material certificate for the AA6082-T6 aluminium used as base material.	I
A.2	Material certificate for the S355 structural steel used as base material.	I
A.3	Material certificate for the AA6082-T4 aluminium wire uses as filler material.	II
C.1	Additional EBS images of a (a) crack and (b) tunnel defect observed in the Al-Fe HYB weld.	III
C.2	Additional EBS images of observed steel fragments at (a) low (50x) and (b) higher (100x) magnification.	III
D.1	Stress-strain curves from the DIC tensile testing for all virtual extensometers. These curves are used to calculate the global E-module and 0.2% offset yield strength of the dissimilar HYB joint.	IV
D.2	Stress-strain curves for vectors positioned in HAZ obtained from Specimen 4.	V
D.3	Stress-strain curves for vectors positioned in HAZ obtained from Specimen 8.	V
D.4	Measured stress-strain curves during tensile testing of specimen 4, for extensometers positioned in the aluminium BM, EZ/HAZ and steel BM.	VII
E.1	Additional BSE micrographs at low magnification (500x), showing the (a) top, (b) bottom and (c) middle part of the Al-Fe bond line of the dissimilar HYB joint.	VIII
F.1	Additional SEM images of the lower, middle, and upper part of the steel fracture surface at different magnifications.	IX
G.1	Additional BSE images of the lower, middle, and upper part of the steel fracture surface at different magnifications.	X
H.1	Crack positioned at different distances from the Al-Fe bond line. 1) 0.1 mm, 2) 0.15 mm, 3) 0.2 mm and 4) 2 mm with increased crack domain.	XI
H.2	Crack positioned at different distances from the Al-Fe bond line. 1) 0.2 mm, 2) 0.3 mm, 3) 0.5 mm and 4) 0.6	XII
I.1	Evolution of strain localization and distribution during simulation of the Al-Fe HYB joint with a crack size equal to 0.03 mm.	XII
I.2	Evolution of strain localization and distribution during simulation of the Al-Fe HYB joint with a crack size equal to 0.1 mm.	XIII

I.3	Evolution of strain localization and distribution during simulation of the Al-Fe HYB joint with a crack size equal to 0.8 mm.XIII
I.4	Evolution of strain localization and distribution during simulation of the Al-Fe HYB joint without crack.XIII

List of Tables

1	Intermetallic phase (IMP) layer thickness, tensile strength, and joint efficiency for Cold Metal Transfer (CMT) weldments of aluminium and steel.	18
2	Intermetallic phase (IMP) layer thickness, tensile strength, and joint efficiency for for friction stir (FS) weldments of aluminium and steel.	23
3	Chemical composition (wt.%) of the AA6082-T6 aluminium used as base material.	34
4	Chemical composition (wt.%) of the S355 structural steel used as base material.	34
5	Chemical composition (wt.%) of the AA6082-T4 aluminium used as filler material.	35
6	Homogenization conditions for the AA6082-T4 DC cast billet.	35
7	Summery of the main welding parameters used in the HYB joining of AA6082-T6 and S355.	36
8	Engineering material data used for the aluminium and steel base materials in the finite element (FE) model.	60
9	The resulting maximum force, strength reduction, and displacement at failure for the simulated Al-Fe HYB joint when introducing a crack having an initial depth of 0.003 to 1.2 mm.	80
10	Tensile test results obtained from Matteo Manfrotto [14].	II
11	Calculated values for the E-module of the Al-Fe HYB joint.	IV
12	Measured tensile properties of the Al-Fe HYB joint.	IV
13	Measured tensile properties of the HAZ.	VI
14	Calculated values for the E-module of the HAZ.	VI

Abbreviations

Al	Aluminium
AS	Advancing Side
BCC	Body Centered Cubic
BSE	Backscatter Electrons
BM	Base Material or Metal
C	Carbon
CMT	Cold Metal Transfer
CTOD	Crack Tip Opening Displacement
DIC	Digital Image Correlation
EZ	Extrusion Zone
FCC	Face Centered Cubic
Fe	Iron
FEM	Finite Element Method
FM	Filler Material or Metal
FSD	Friction Stir Dovetailing
FSW	Friction Stir Welding
FZ	Fusion Zone
GMAW	Gas Metal Arc Welding
GTAW	Gas Tungsten Arc Welding
HAZ	Heat Affected Zone
HSLA	High Strength Low Alloy
HYB	Hybrid Metal Extrusion & Bonding
IMC	Intermetallic Compound
IMP	Intermetallic Phase
LEFM	Linear Elastic Fracture Mechanics
LOM	Light Optical Microscope
Mg	Magnesium
RS	Retreating Side
SEM	Scanning Electron Microscope
Si	Silicon
SZ	Stir Zone
T4	Naturally aged condition
T6	Peak-aged condition
TEM	Transmission Electron Microscope
TMAZ	Thermomechanically Affected Zone
UTS	Ultimate Tensile Strength
XFEM	Extended Finite Element Method

1 Introduction

1.1 Motivation

Today one of the world's biggest challenges is the climatic changes and pollution caused by industrial activity and the transportation sector. In particular, the humanly created CO_2 -gas emission, which mainly comes from the burning of fossil fuels, has to be reduced [1]. As a consequence, strict regulations have been imposed by the government for reducing the CO_2 -gas emission. For instance, within the automotive industry, reducing the exhaust emission and increase engine efficiency is a demand [2]. One way of achieving this is to increase the use of tailored multimaterial solutions by combining the use of different types of materials within a component or assembly. In this way, more optimal structures with lower weight and higher performance can be obtained, both in terms of cost and environmental impact [3].

Traditionally, steel has been the material of choice within the transportation sector due to its high strength and stiffness. However, there is a need to reduce the amount of steels in modern automotive applications due to its weight. Aluminium alloys, as the Al-Mg-Si alloys, exhibit favorable physical and mechanical properties, as high strength-to-density ratio and good formability, which makes them an ideal candidate for replacing steel in several applications [2, 4]. However, in complex structures, such as the car subframe, is it not beneficial (or even possible) to produce the entire part using only aluminium alloys [2]. As a result, the combined use of aluminium and steel may offer several advantages. In fact, combining these two metals have proven to successfully create more fuel-efficient vehicles by reducing the overall weight as well as the power consumption during manufacturing [5, 6]. However, welding and fabrication of aluminium-steel products are challenging because of their significant difference in physical and thermal properties (e.g., melting temperature, coefficient of thermal expansion, heat capacity and solidification shrinkage), which may give rise to a variety of weld defects [3, 7]. Therefore, joining of dissimilar materials has become a significant consideration during the last years due to the increased demand for complex industrial applications [5, 6].

One of the major challenges in aluminium-steel welding is the formation of brittle intermetallic phases (IMP), or intermetallic compounds (IMC), along the interface between the two materials. Even though these IMPs are necessary to achieve bonding, the high thermal input in conventional welding processes leads to an excessive formation of these phases resulting in brittleness of the bond [4, 8]. Thus, both the composition and thickness of the IMPs can strongly affect the mechanical integrity

of the joint [8, 9]. In addition, the thermal input associated with conventional welding techniques can change the width of the heat affected zone (HAZ) occurring on the aluminium side. This is critical for the load-bearing capacity of aluminium welds supposed that sufficient bonding is obtained [10]. At present, several welding processes have successfully been used for joining of aluminium and steels, including both Cold Metal Transfer (CMT) and Friction Stir Welding (FSW). But, as stated by Kovacevic et al. [7], none of the existing methods are able to produce reliable welds for industrial applications taking both quality and cost into account. Therefore, there is a need for an, even more, energy efficient welding process operating at even lower temperatures to produce high-quality welds between dissimilar materials.

The Hybrid Metal Extrusion & Bonding (HYB) process is a patented solid-state joining technique which by the use of filler material addition and plastic deformation can produce sound joints at even lower temperatures than conventional welding processes [11]. Initially, the process was developed for butt welding of aluminium alloys but has evolved into a multi-functional joining technique handling different joint configurations and material combinations [12]. Moreover, the process has shown great potential for joining challenging materials, as for instance, aluminium and steel [13]. In this case, the low operational temperature is seen to have a positive effect on both IMP formation at the Al-Fe interface and the width of the HAZ on the aluminium side, which both are critical factors for the resulting joint strength [13, 14]. At present, successful bonding has been obtained between 4 mm rolled plates of aluminium alloy 6082-T6 and structural steel 355. However, the process is not yet optimized, and there is a need for further characterization and examination of the joint to improve the process and bring it one step closer towards industrialization and commercial use.

1.2 Objectives

At present, there is little published information related to the mechanical integrity of dissimilar Al-Fe HYB joints. Despite that a general mechanical characterization of a 4 mm AA6082-T6 and S355 HYB butt joint can be found in the master thesis of Matteo Manfrotto [14], a detailed analysis of its mechanical properties and microstructure have not yet been carried out. Therefore, the aim of the present report is to give an in-depth analysis of the bond strength of the same joint, serving as an extension of the previous work, in order to provide a more consistent picture of the HYB process usefulness for dissimilar joining of aluminium and steel. Such an in-depth analysis has never been done before.

The objective is more specifically to combine the already existing results from Manfrotto [14] with the results obtained during this project to develop a finite element (FE) model that can simulate the behavior of the dissimilar HYB weld. To achieve this goal, the following steps must be followed:

- Detect critical areas of the dissimilar HYB weld and understand how the joining process affects the materials.
- Obtain global material properties for the different zones of the Al-Fe HYB weld.
- Determine the fracture model and behavior of the dissimilar HYB weld.
- Create an FE model that represents a tensile specimen of the Al-Fe HYB weld, which can simulate the behavior of the specimen during tensile testing.
- Verify the FE model by the use of experimental data.

1.3 Scope

Thus, a more extensive examination of the dissimilar Al-Fe HYB joint microstructure and bond line will be given, together with analysis of the tensile test results. The microscopic examination of the joint includes both the use of optical microscopy and scanning electron microscopy (SEM). The tensile tested specimens are analysed by the use of digital image correlation (DIC), while the fracture surfaces are investigated in the SEM. The DIC analyses are also used to determine the local material properties for the different weld zones. All experiments are conducted at room temperature. The finite element (FE) model is developed using ABAQUS/CAE (6.17) [15] and includes the implementation of different material properties for the base materials and weld zones, as well as properties for fracture initiation and propagation. The validation of the model is performed by comparing the simulated results with the results obtained from the DIC analyses.

2 Theory and literature review

2.1 Aluminium alloys

2.1.1 Overview

Aluminium (Al) and aluminium alloys are characterized by their low density, 2.7 g/cm^3 , high electrical and thermal conductivity, and good corrosion resistance [16]. When aluminium is exposed to air, the metal reacts with oxygen and an oxide layer forms on the metal surface. This layer is what gives the material its good corrosion resistance, and enables it to be used for exposed applications without additional protection [17]. Pure aluminium has low strength, due to the high dislocation mobility in the face-centered cubic (FCC) crystal structure, and is therefore commonly strengthened by the addition of alloying elements in order to be used for structural applications [17, 18, 19]. The FCC structure is also what gives the metal its good formability [17].

A variety of aluminium alloys have been developed where their mechanical properties have been tailored to a specific application area. For instance, the 6xxx series is a class of aluminium alloys that are frequently used in the automotive industry due to their high specific strength (strength-to-density ratio) and corrosion resistance [20]. The strength of these alloys mainly comes from the primary alloying elements, magnesium (Mg) and Silicon (Si) [18], and are therefore often referred to as the Al-Mg-Si alloys.

2.1.2 Al-Mg-Si alloys

The Al-Mg-Si alloys are wrought, heat-treatable alloys with good machinability and weldability. The mechanical properties of these alloys are often improved by precipitation hardening (age hardening) to obtain the highest strength in the T6 temper condition [18]. Precipitation hardening increases the strength of the material through the formation of small dispersed particles of a second phase within the original phase matrix. This is done by a phase transformation introduced by a controlled heat treatment process [16]. During aging, the properties change with respect to time and temperature, and both strength and hardness increase with time, as illustrated in Figure 2.1, until the peak-aged (T6) condition is obtained. After this point, the strength starts to decrease gradually. The solution heat-treated Al-Mg-Si alloys also have the ability to naturally age, which is the process where the strength is increased during storage at room temperature [10]. This is

referred to as the T4 condition as illustrated by the dotted line in the figure.

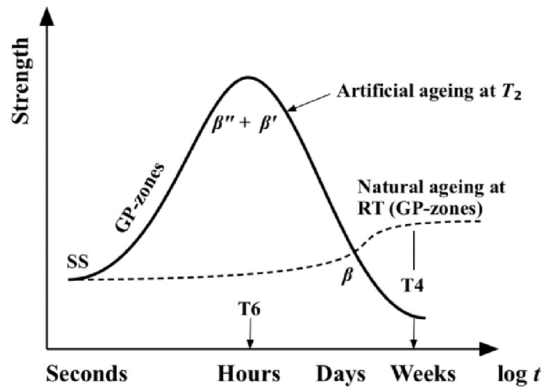


Figure 2.1: The strength evolution during aging of Al-Mg-Si alloys. Copied from [10].

The presence of the hard precipitates particles, together with the strain field in the matrix surrounding the precipitates, forms a barrier to dislocation movement [18]. The dislocations get trapped by the particles, and their only possibility is to either bow out between the particles, as shown in Figure 2.2a or cut through them, illustrated in Figure 2.2b. Thus, a higher stress level is required for slip to occur, and the strength of the material is increased [21, 22].

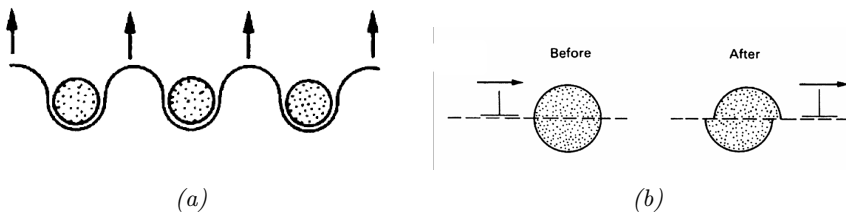


Figure 2.2: Particulates forms a barrier to dislocation movement, the dislocations can pass through them by (a) bowing or (b) cutting. Copied from [22].

Grain size refinement is also a method for strengthening of the Al-Mg-Si alloys. Adjacent grains in the material have different crystallographic orientations and share a common grain boundary. The smaller the grains, the more grain boundaries will exist in the material. Grain boundaries also act as a barrier to dislocation motion or slip. The yield strength, σ_y , is related to the average grain size, d ,

by the Hall-Petch equation, as shown in Equation 2.1. Here the K_y and σ_0 are constants for the specific metal [16].

$$\sigma_y = \sigma_0 + K_y d^{-\frac{1}{2}} \quad (2.1)$$

2.1.3 Welding of Al-Mg-Si alloys

The Al-Mg-Si alloys have both physical and mechanical properties which make them attractive for a wide range of structural applications and thus, welded assemblies. However, when the Al-Mg-Si alloys are used for welding, they can experience severe softening in the heat affected zone (HAZ) caused by the heat generation associated with the welding process [23]. The thermal stability of the hardening precipitates which form during artificial aging (T6) is low, leading them to coarsen and reverse (dissolve) when exposed to heat [17, 24]. The smallest precipitates will start to dissolve when the peak temperature is above 250 °C, while the largest ones will continue to grow [24]. This microstructural evolution during thermal processing of the Al-Mg-Si will not be considered further. Note that the severe softening is not the case for the naturally aged (T4) condition. This HAZ is a major concern in aluminium welding due to the mechanical degradation of the base material, and will often be the area that determines the load-bearing capacity of the overall joint. Other problems related to welding of Al-Mg-Si alloys include solidification cracking and hot cracking [23].

2.2 Steel

2.2.1 Overview

Steel are ferrous alloys containing mainly iron (Fe) and carbon (C), but may also contain concentrations of other alloying elements. Steel has a high density (7.9 g/cm^3) compared to aluminium, and a body-centered cubic (BCC) crystal structure which has lower dislocation mobility compared to FCC and hence higher strength. The main disadvantage with many ferrous alloys is their high susceptibility to corrosion. The classification of steels is often according to the carbon content, which strongly affects the materials mechanical properties. The widespread use of steel as an engineering construction material is due to the vast quantities of iron compounds within the Earth's crust, the relatively low production cost in addition to its versatility regarding mechanical and physical properties [16, 17].

Of all the different steels utilized, those produced in most considerable quantities are within the low-carbon classification. Their microstructure consists of ferrite and pearlite, which give them good ductility and toughness. In addition, have the low-carbon steels properties as good machinability and weldability, making them suitable for automotive applications. These alloys are not affected by heat treatment intended to form martensite and are commonly strengthened by strain hardening. Strain- or work hardening increases the strength of the material through plastic deformation. When the material is plastically deformed the dislocation density increase in the material together with the internal stress. An increase in the dislocation density makes it more difficult for the dislocations to move and therefore hinders slip [16].

2.2.2 High-strength low-alloy (HSLA) steel

A group of the low-carbon alloys is the high-strength low-alloy (HSLA) steels, such as S355. These alloys contain a small amount of alloy additions other than carbon, which gives them higher strength than plain low-carbon steels without any additional alloying elements. The impurity atoms impose lattice strains on the surrounding atoms, in addition to refinement of the ferrite grain size, which leads to restriction of dislocation movement and increased strength of the material. In addition to their high strength, typical minimum yield strength in the range 300-500 MPa, the HSLA steels are ductile, formable and easy to weld [16, 23]. HSLA steel was primarily developed for the automotive industry to replace other low-carbon steel and improve the strength to weight ratio. With higher strength, less material is needed to obtain the same strength properties, and vehicles with lower weight can be produced. [25].

2.2.3 Welding of HSLA steel

During welding, microstructural changes can occur in the HSLA steel depending on the amount of heat generated during the process. Nitrides and carbides can coarsen and dissolve, and grain growth can occur, leading to a strength reduction in the HAZ in a similar manner as for the Al-Mg-Si alloys. The microstructural changes lead to a reduction in the toughness of the weld and increase the risk of cold cracking/hydrogen cracking. Another critical problem related to welding of HSLA steels is to prevent brittle fractures due to increased strength in certain areas, caused by the structural transformation and impurities dissolved in the metal [23, 25]. However, a much larger local heating is required to form a HAZ and microstructural changes in steel compared to aluminium. Denys [26] noted that

HAZ softening typically occurred in the 650-1100 °C peak temperatures for high strength steels (TMCP/QT), which is significantly higher than the 250 °C for the Al-Mg-Si alloys.

2.3 Welding of dissimilar metals

2.3.1 An introduction

Mathers [17] describes welding as the joining of two components by coalescence of the material surfaces in contact with each other. Different methods can achieve this coalescence, either by melting the parts together, which is referred to as fusion welding or by bringing the two surfaces together under high pressure to create bonding. This is referred to as solid-state welding. The different methods can be used with or without a filler material between the two materials to be joined.

During the latter years, the importance of joining dissimilar materials has increased significantly, particularly within the automotive industry. The main reasons for this are the aim to reduce the CO₂-gas emissions and produce more energy efficient solutions [7, 27]. The use of iron- and aluminium-based alloys are most frequently applied to achieve these goals [7], and, therefore, joining these materials have become of great importance. In addition, has the emerging regulations from the government (related to emission, safety, and fuel efficiency) made car manufacturers thrive towards improving the engine efficiency, develop hybrid power-train systems and reduce the total weight of the vehicles to meet these strict requirements [2]. The European Aluminium Association [28] has stated that, with respect to the automotive market, is joining of aluminium and steel the most important task in the future, and the driving force for developing new and improved joining techniques.

In the automotive industry is the reduction of vehicle weight of particular importance, as the weight is expected to increase in the future due to increasing customer demand for more luxury, better performance, and higher safety. Even though thin, high strength steel sheets have been developed, the total effect on the vehicle weight is limited and, therefore, more innovative actions are needed. One solution is the use of mixed material structures composed of lightweight materials [4]. The favorable properties of aluminium alloys make them suitable for the replacement of heavier materials in several automotive components [2]. However, the use of aluminium alloys as a structural material, considering both the materials cost and properties, is limited to certain parts within the vehicle assembly such as the hood, trunk, doors, and roof. Thus, because aluminium alloys are used for specific ap-

lications, these parts often need to be joined to other steel parts and, therefore, there is a need for technologies capable of joining these two materials [4].

An industrial case where aluminium and steel are welded together to form the component is the Honda Motor Corporation. Here, the subframe is made of a die-cast aluminium alloy and press formed steel. Friction Stir Welding (FSW) is then used for welding the two materials together in a lap joint configuration, as indicated by the purple spots in Figure 2.3. This new subframe resulted in a total body weight reduction of 25%, and a 50% reduction in electrical consumption compared to the original steel subframe [5, 6]. Thus, the indications are that there is a vast potential for a reduction in weight and energy consumption by implementing multimaterial solutions made of aluminium and steel.

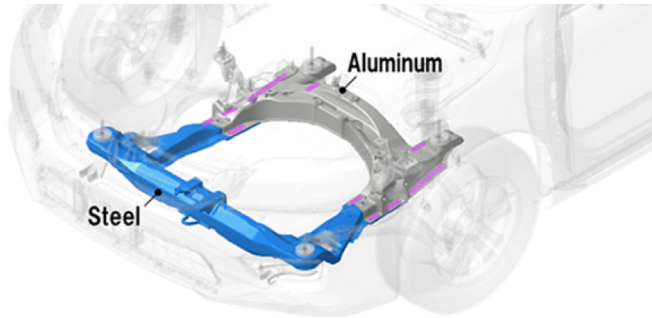


Figure 2.3: Honda Accord front subfram using friction stir lap welding (FSLW) of die cast aluminium and press formed steel. Copied from [6].

The aim towards lightweight, high performance, and optimal structures by the use of hybrid multimaterial structures of aluminium and steel does not only concern the automotive industry, but also other industries as aerospace, military, power generation, and marine sectors. However, when utilizing different materials to increase the product performance, the joining process is critical in order to obtain a sufficient product [6, 7]. A variety of joining techniques have been used for joining of aluminium and steel, such as mechanical joining, solid-state joining techniques (e.g., friction welding, ultrasonic welding, and explosion welding [7]) and adhesive bonding. However, most of these methods are restricted to certain simple geometries and suffers from a lack of reliability for industrial applications when it comes to either mechanical properties of the joint, cost or quality [7, 28].

2.3.2 Bonding mechanisms in dissimilar weldments

When joining dissimilar materials by welding, the joint can be produced either by the use of a filler material (FM), as commonly done in fusion welding, or without any additional material, as in Friction Stir Welding (FSW) [17]. Depending on which technique that is utilized, one or more interfaces will be created between the base materials (BM), and different bonding mechanisms may occur, as illustrated in Figure 2.4. In Figure 2.4a, a dissimilar joint formed by the use of filler material addition is shown. In this case, the filler material is an aluminium alloy. As can be seen from the figure, two bond lines occur. One at the interface between the FM and BM1 (yellow line), and one at the interface between the FM and BM2 (red line). Assuming that BM1 and the FM are similar materials, that means they contain only minor differences when it comes to their chemical composition, as for instance different types of aluminium alloys [29], metallic bonding occurs between them. By this means that bonding happens by the sharing of valence electrons [16].



Figure 2.4: Depending on which joining technique that is used, different interfaces and bonding mechanisms can be observed. (a) illustrates the two interfaces that will form by the use of a filler material addition between BM1 and BM2, while (b) shows the one interface that appears by directly bonding the two metals.

Now, assuming that BM2 is a different material than that of the FM and BM1, the bonding between BM2 and the FM is intermetallic, which means that the two metals are different from each other and the sharing of valence electrons are impossible. Instead, the formation of intermetallic phases occurs as a link between the two metals and creates bonding. This is also the case in Figure 2.4b, where BM1 and BM2 are welded together without filler material addition. A more in-depth explanation of these two bonding mechanisms will be given in the following.

2.3.3 Metallic bonding

To obtain sound joints in weldments of similar metals, metallic bonding is needed. Bonding between these metals is achieved when they are brought closely together (in an atomic scale) such that metallic bonding can occur through the sharing of valence electrons [16]. In metals, the electrons in the outer orbit are free to

move throughout the bulk of the material, and the atoms which become positively charged, are surrounded by a cloud of negatively charged electrons, as illustrated in Figure 2.5. The difference between the positively charged atoms and the negatively charged electrons creates a magnetic attraction, which binds the metals together when the two interfaces are brought close enough together [17]. Metallic bonding is the primary bonding type in metals and is both strong and non-directional. Both joining in liquid and solid state between similar materials involves the formation of this type of bonding mechanism. As a consequence of the free electrons, metals have high thermal and electrical conductivity. In addition, they have the ability to deform extensively before fracture, which causes them to often fail in a ductile manner [16, 17].

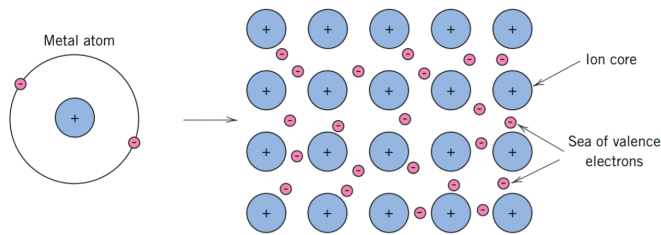


Figure 2.5: Illustration of metallic bonding. Copied from [16].

2.3.4 Intermetallic bonding

Joining of dissimilar metals, as Al and Fe, is quite different compared to the joining of similar metals (e.g., Al and Al), due to their distinct differences in atomic structure, as illustrated in Figure 2.6. The high degree of incompatibility makes the sharing of valence electrons difficult. Instead, when joining aluminium and steel, intermetallic phases (IMP) will form at the Al-Fe interface and create the bond between the two metals [7, 9, 13]. These phases form during joining in both liquid and solid state, either by diffusion at the interface or during solidification of the molten material [28]. By looking at the binary phase diagram for Fe and Al, shown in Figure 2.7, a wide range of IMPs may form during the joining process. The different IMPs are grouped as Fe-rich, FeAl and Fe_3Al , or Al-rich compounds, $FeAl_2$, Fe_2Al_5 and $FeAl_3$ [30]. Which of these different compounds that form the reaction layer depends both on the kinetics [31], the welding parameters (i.e., time, pressure and temperature), and the metals [7].

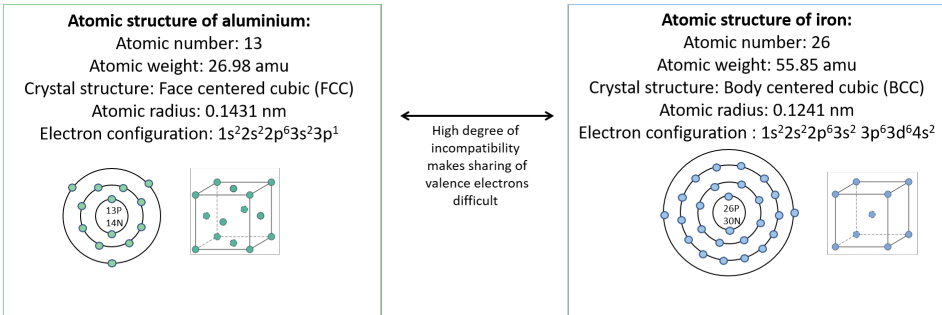


Figure 2.6: A comparison of the atomic structure of aluminium (Al) and iron (Fe) [16]. The high degree of incompatibility between the atomic structures makes the sharing of valence electrons difficult.

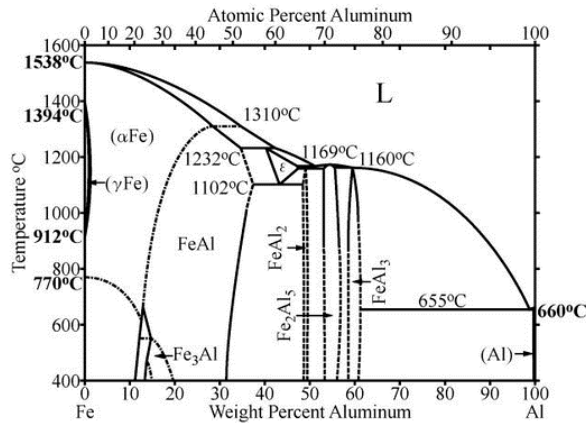


Figure 2.7: Fe-Al binary equilibrium phase diagram. Copied from [30].

It is worth noticing that the properties of the different IMPs are different from that of both the BMs and FM, which makes their composition important for the overall strength of the joint [32]. The most commonly reported IMPs formed during joining of aluminium and steel are the Al-rich Fe_2Al_5 and Fe_4Al_{13} [9]. They have a low symmetry crystal structure and are, therefore, more brittle than the Fe-rich phases. This is because the diffusivity of Al in Fe is much lower than the diffusivity of Fe in Al [8, 33]. The phases are characterized by their extreme hardness and, therefore, brittleness, and to manage their effect on the joint strength the diffusion process should be controlled, and the IMP layer thickness should be kept below a specific critical value (below $5\mu\text{m}$ or $10\mu\text{m}$) [9, 34]. If the layer is above this critical thickness, there will be a reduction in the joint toughness, which will inevitably

result in reduced overall strength of the joint [9, 32]. On the other hand, if the layer is too thin and discontinuous, there will not be sufficient bonding, which also results in a strength reduction of the joint [31].

2.4 Conventional welding techniques used for joining of aluminium and steel

2.4.1 Challenges related to dissimilar joining of aluminium and steel

Producing a reliable joint between aluminium and steel is difficult due to their poor metallurgical compatibility and significant differences in thermomechanical properties [7]. As already mentioned, have the materials a distinct difference in atomic structure and chemical composition. The key metallurgical challenge of welding of the two materials is, however, their considerable variations in thermal properties, which may give rise to a variety of welding defects [13]. This includes different melting temperature, coefficient of thermal expansion, thermal conductivity, and heat capacity. Due to these differences, a large amount of thermal stress builds up during the thermal joining process, which is making the joint susceptible to cracking and brittle failure during service [8]. Some thermal properties for steel and aluminium are compared in Figure 2.8, including some specific challenges.

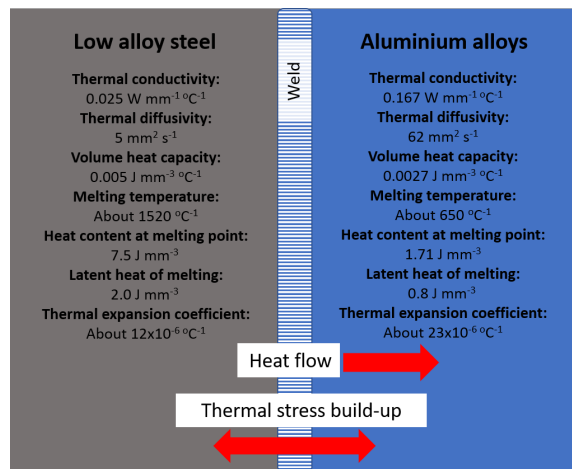


Figure 2.8: Comparison of thermal properties of steel and aluminum, and specific challenges involved in welding and fabrication of Al-Fe products (Ø.Grong, Personal Communication, 2019).

When heat is generated during the welding operation, thermal gradients build up between the aluminium and steel part of the joint. Aluminium has a significantly higher thermal conductivity than steel, as shown in Figure 2.8, resulting in that most of the heat flows through the aluminium. The fact that aluminium has a low melting temperature, 650°C compared to 1520°C for steel, results in that the aluminium experiences softening at a lower temperature relative to the steel [19]. This happens at a greater extent when most of the heat is transferred to the aluminium part of the joint and can lead to the formation of liquid nuggets [8]. If enough heat is generated such that melting occurs, this makes the weld susceptible to pore formation, hot cracking, and other bonding defects causing degradation of the joint [11]. The coefficient of thermal expansion is almost twice the value for aluminum compared to steel (see Figure 2.8), something that can cause buckling and distortion of the aluminium part of the joint during processing [17].

Wetting of solid steel by liquid aluminium is a requirement for solid-liquid reaction and joining of the two materials [8]. The stable passivating oxide layer of Al_2O_3 covering the aluminium surface has to be removed before joining of the metals, due to its negative effect on the wettability. The oxide layer can be broken up by heat or force or a combination of the two, but due to its high melting temperature of approximately 2060°C, high heat input is required [8, 17]. The high thermal input will again result in an excessive formation of IMPs and a thick reaction layer at the joint interface, which reduces the mechanical strength of the joint [13]. Oxide removal by the use of deformation and force is, therefore, preferred during welding of aluminium and steel.

When two different metals are in contact, the difference in their ionization tendency can cause corrosion to occur at the interface [4]. The thermal joining of aluminium and steel provides an electrically conductive connection, which may cause galvanic corrosion to take place. Corrosion is, therefore, a considerable issue in Al-Fe welding, but this will not be covered more in detail in this report. Note, that correct precautions to prevent corrosion when joining the two metals is necessary [19], and both the FM, the formation of IMCs and a galvanic zinc layer, are parameters that can influence the corrosion resistance of the joint [35].

2.4.2 Fusion welding

Fusion welding is a welding technology which uses a high-intensity external heat source (e.g., electrical arc, electron beam or laser) to localize melt the FM and BMs together. This melting process generates a lot of excess heat, which strongly affects the surrounding metal and its microstructure. Three distinct zones in a fusion

weld are evident and consist of the HAZ, the fusion zone (FZ) and unaffected BM. The different zones have different microstructures as a consequence of the non-uniform heating and solidification, where the FZ is similar to an as-cast structure, and the HAZ has altered structure relative to the BM [7, 29]. As mentioned, will the aluminium experience a degradation of strength in the HAZ. However, the steel does not exhibit the same softening from the microstructural changes when exposed to the same temperatures during the fusion welding process. As shown from the Al-Fe phase diagram, Figure 2.7, the formation of brittle IMPs is promoted by high temperatures. The thickness of the IMP layer is also increased with increased temperatures [3]. This gives the fusion welding processes major challenges regarding welding of aluminium and steel.

Fusion welding is the most used joining method for aluminium alloys due to its productivity, flexibility, robustness, and cost efficiency [10, 36]. Electric arc welding is the most common method for fusion welding, which includes both Gas Tungsten Arc Welding (GTAW) and Gas Metal Arc Welding (GMAW) [6]. Both of these processes have high heat input and little chance of slug to get entrapped in the weld metal since no flux is needed. The shielding gas utilized during the welding also protects the arc and causes little loss of alloying elements [7]. Electric arc welding can produce weldments of a variety of steel and aluminium alloys, but since the weld heat input should be kept at a low rate, other methods have shown greater potential including Cold Metal Transfer (CMT).

Cold Metal Transfer (CMT)

The CMT method is a relatively new process for joining of aluminium and steel [3, 37, 38]. The technique is an extension of GMAW, also known as MIG welding, where a consumable filler material is fed towards the BM by a wire feeder. In CMT is an additional motor installed to retract the wire after the droplet has reached the weld pool. This is done to get higher precision and control of the heat input [37, 39]. The CMT process is, therefore, more stable and generates lower heat compared to MIG, something that is beneficial regarding the formation of the IMP layer during joining of aluminium and steel [3, 38]. CMT is commonly used to produce dissimilar Al-Fe lap joints, as illustrated in Figure 2.9. The two metal sheets are joined together by continuously feeding an aluminium filler wire along the edges of the plates. The droplets of the aluminium FM merges with the molten aluminium BM and forms a fusion joint, whereas a brazed connection forms between the melted wire and the steel BM [3, 38].

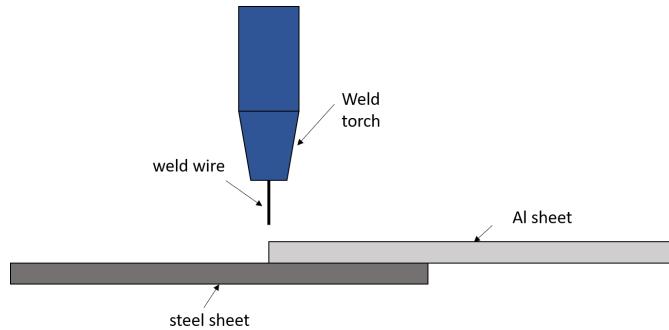


Figure 2.9: Schematic illustration of the Cold Metal Transfer (CMT) welding assembly for a dissimilar Al-Fe lap joint. Copied from [40].

Several successful joints between aluminium alloys and steel by the use of CMT have been reported in the literature. In the following, some examples from the literature will be given. Table 1 shows the resulting reaction layer thickness, ultimate tensile strength (UTS) and joint efficiencies for different dissimilar Al-Fe lap joints produced by CMT.

Table 1: Intermetallic phase (IMP) layer thickness, tensile strength, and joint efficiency for Cold Metal Transfer (CMT) weldments of aluminium and steel.

Al BM	Fe BM	FM	Sheet thickness	IMP thickness	UTS	Joint efficiency	Ref.
AA6061-T6	Galvanized boron steel	AA4043	1 mm	4-8 μm	193 MPa	68 %	[38, 41]
AA5754	EN10143	AA4043	2 mm	3 μm	125.8 MPa	53.1 %	[3, 42]
AA6082-T6	HCT600	AA4043	3/1.5 mm	3-4 μm	104 MPa	34.7%	[43, 44]

Çömez and Durmuş [3] investigated the properties of a CMT lap joint consisting of AA5754 and EN10143. They observed the formation of a brittle Fe_2Al_5 IMP layer, which resulted in fracture occurring along in the Al-Fe bond line and, hence, a low joint efficiency, as shown in Table 1. They did not detect any changes in the microstructure of the steel BM, while a significant coarsening of the aluminium grains was evident when the heat was increased. With increased heat where also an increase in the IMP layer thickness along the Al-Fe bond line noticed, from approximately 2.1 μm to 4.7 μm , respectively. The IMP layer can be seen in Figure 2.10a.

When studying the CMT produced lap joint of AA6061-T6 and galvanized boron steel, Cao et al. [38] found that the Al-Fe interface consisted mainly of Fe_3Al and $FeAl$, and that one of the samples failed in the HAZ while the other failed in the weld metal. They noted that the thickness of the IMP layer was not uniform along the Al-Fe bond line. The interface located at the center of the weld metal was in the range of 4-8 μm , which is larger than the 2-3 μm detected at the edges. Figure 2.10b shows the IMP layer at the transition interface obtained from Cao et al.'s research.

Tranø [43] studied the welding of AA6082-T6 and HCT600, and only experienced that fracture happened in the HAZ. Even though, where the joint efficiency only 34.7%, as shown in Table 1, which is significantly lower than what was observed by Çömez and Durmuş [3] and Cao et al. [38].

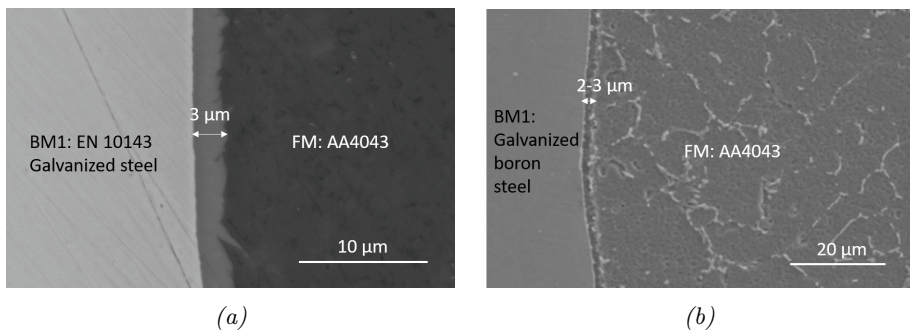


Figure 2.10: Intermetallic phase (IMP) layers observed in Cold Metal Transfer (CMT) lap joint of (a) AA5754 and EN10143 (copied from [3]) and (b) AA6061 and galvanized boron steel (copied from [38]).

Common defects related to Cold Metal Transfer (CMT) welding of aluminium and steel

Due to non-uniform heating and solidification in fusion welding, cracking, porosity and other imperfections often occur in relation to the in-homogeneous phase changes [7]. As in the research done by Cao et al. [38], the failure started at the root of the FZ, as shown in Figure 2.11, where faulty fusion had formed due to a relatively low temperature in this area, caused by poor wettability of the FM. Another defect, as already mentioned observed by Cao et al. [38], is heterogeneity in the thickness of the IMP layer formed during the welding process. This is also a result of the non-uniform thermal cycle near the weld area.

Furthermore, the Al-Mg-Si alloys have a relatively wide solidification range, which makes them sensitive to solidification cracking in the FZ. Solidification cracking is a result of the solidification shrinkage that occurs in the aluminium, in addition to the

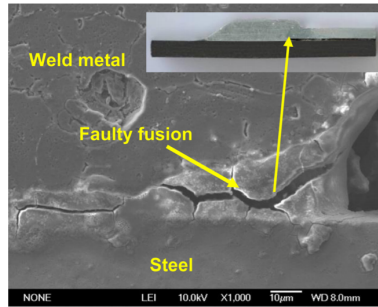


Figure 2.11: Fracture initiation at the weld root due to faulty fusion in a Cold Metal Transfer (CMT) lap joint produced of AA6061-T6 and galvanized boron steel. Copied from [38].

existing high thermal stresses that arise when the weld pool solidifies. Pores caused by hydrogen are also a common defect during fusion welding of aluminium alloys. Liquid aluminium has a much higher ability to absorb hydrogen than in the solid state. The hydrogen gets trapped and form pores during the solidification, which may lead to increased porosity of the final joint [28]. This was reported among others by Çömez and Durmuş [3] where the fracture surface showed numerous micro-scale pores in the weld seam.

Regarding the CMT joining method which consists of a lap joint configuration, additional defects arise compared to the butt joints associated with GTAW and GMAW. The bonding strength is dependent on the length of the bond line, which makes the zinc coating used on the steel during CMT welding important [40]. The zinc coating protects the steel BM from oxidation prior to the welding process. Because the oxide layer affects the welding process by disrupting the wetting and spreading of the aluminium FM on the steel BM, the use of a zinc layer results in a lower wetting angle and a longer bonded line length [40, 45]. The coating can also remove some heat from the process due to vaporization of the zinc [3]. Niu et al. [40] and Cao et al. [38] both observed zones of high concentration of zinc near the edges of the weld. These zinc-rich areas where the zinc coating had not vaporized entirely contains zinc vapor trapped inside the melt pool. This causes pores and lack of fusion as observed by Niu et al. [40]. These zinc rich areas have also shown to be acceleration sites for corrosion in aluminium and steel CMT weldments [40].

2.4.3 Solid-state welding

The solid-state welding techniques do not involve melting and solidification of the materials to be joined and, therefore, operate at temperatures below the melting temperature of the filler- and base materials [29]. Hence, these processes offer several advantages over the fusion welding processes regarding joining of aluminium and steel [13]. Bonding in these techniques is achieved by excessive plastic deformation and diffusion by the use of either mechanical, electrical, or thermal energy. Which of the many existing solid-state joining processes that are utilized depends on the final product and its applications [46]. One of the more recently developed joining techniques is Friction Stir Welding (FSW) [13]. This process has successfully been able to join aluminium and steel as reported by among others Ramachandran et al. [47] and Sajan et al. [48].

Friction Stir Welding (FSW)

Friction Stir Welding (FSW) is a technique where frictional heat is generated by the conversion of mechanical energy into thermal energy at the interface of the workpiece. A rotational pin interacts with the workpiece, and a weld is created by a combined action of frictional heat and plastic deformation caused by the rotating tool [29]. The principal features of the process are shown in Figure 2.12. The pin is pressed against the contacting surfaces between two overlapping or abutted aluminium and steel plates. Due to the frictional heat, a softening zone occurs around the pin, and the material is swept around the pin as the tool continues along the bond line. However, this softened material is constrained by the tool shoulder and can, therefore, not escape. Joining is here achieved without the use of an FM. Compared to other solid state joining methods, is FSW a technique which generates high strains and strain rates and is defined as an asymmetrical process [49].

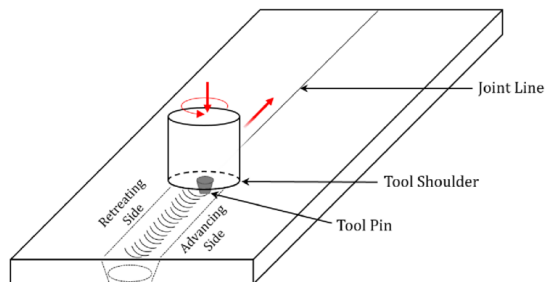


Figure 2.12: Schematic illustration of the Friction Stir Welding (FSW) process for butt joining of aluminium and steel plates. Copied from [50].

As illustrated in Figure 2.12 the advancing side (AS) is the side where the rotational tool is moving in the same direction as the welding direction, while the retreating side (RS) is the side where the rotation motion opposes the travel direction. As shown in the research done by Sajan et al. [48], which side that is the advancing and retreating in joining of aluminium and steel can be of great importance. Having aluminium in the RS in an FS weld of AA6082 and mild steel resulted in a maximum tensile strength of 35 MPa, while having aluminium on the AS the tensile strength increased to 160 MPa. However, Watanabe et al. [51] successfully joined AA5083 and SS400 mild steel plates by FSW and reported that no joining was achieved when the aluminium alloy was placed on the AS. This indicates that different operational parameters and welding tools, in addition to the positioning of the pin in the weld groove contribute to deciding which side should be the advancing and retreating.

Joining of aluminium and steel by FSW can result in a full-strength weld, without any sacrifice of integrity or strength of the weld. Heat is localized at the weld center and is quickly removed during the joining operation, leading to only minor effects on the BMs. The HAZ adjacent to the weld only consists of a narrow band which, therefore, does not affect the temperature of the neighboring area [7]. However, softening of the HAZ is still a significant problem also during this welding technique. The as-cast microstructure in the FZ obtained during fusion welding is eliminated, and replaced with a thermomechanically affected zone (TMAZ) with superior mechanical properties regarding ductility and toughness [10]. A weld nugget is found in the center of the weld where the material is swept around by the rotating tool at a relatively high temperature. Due to the deformations in the stir zone (SZ), the material often experiences grain refinement and strengthening in this area [49].

In FSW, the rotation of the pin generates heat, and a higher rotational speed leads to increased heat input. As stated by Ramachandran et al. [47], both tool rotational speed and tool tilt angle has to be optimized to produce a sound joint with limited IMP layer thickness. Figure 2.13 shows the IMP layers observed by Ramachandran et al. [47] and Ghosh et al. [52] during their examination of different aluminium and steel welds produced by FSW. Both found a reaction layer thickness of approximately $1 \mu m$, which is significantly lower than the thickness observed for CMT. Furthermore, also in these joints [47, 52], the thickness of the IMP layer where not uniform over the entire Al-Fe interface. This was also observed by Watanabe et al. [51], where only IMPs were found on the upper region of the Al-Fe interface, where the temperature during the process reaches its maximum.

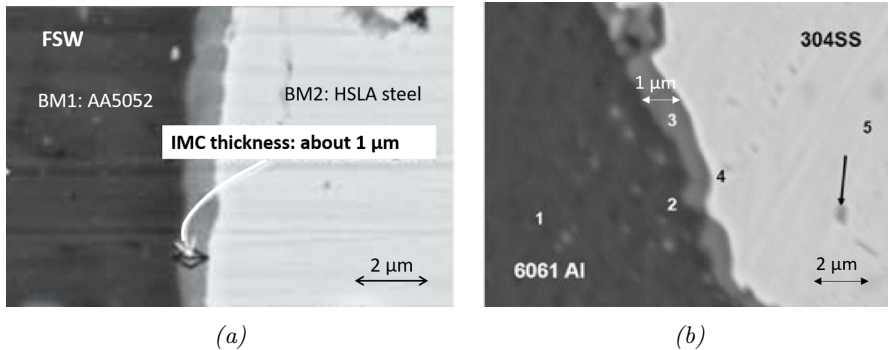


Figure 2.13: Intermetallic phase (IMP) layers observed in friction stir (FS) butt welds of (a) AA5052 and HSLA steel (copied from [47]) and (b) AA6061 and 304 stainless steel (copied from [52]).

Table 2 shows the resulting reaction layer thickness, ultimate tensile strength (UTS), and joint efficiencies for different dissimilar Al-Fe butt joints produced by FSW obtained from the literature. Ramachandran et al. [47] studied an FS weld produced by AA5052 H32 and HSLA steel. They did not observe any distinct TMAZ or HAZ on the steel side of the joint. In the SZ the grains showed signs of refinement due to the dynamic recrystallization effect, and a finite TMAZ with minor deformations were detected next to the weld nugget. No clear HAZ on the aluminium side of the joint was observed, but a significant drop in hardness can often be evident in this area [49]. The fracture of the joint was a combination of a brittle and ductile fracture mode, where the top part of the weldment was almost entirely caused by the brittle fracture mechanism, while the rest of the joint showed signs of a ductile fracture mechanism. This resulted in a high joint efficiency of 94%, as shown in the table.

Table 2: Intermetallic phase (IMP) layer thickness, tensile strength, and joint efficiency for for friction stir (FS) weldments of aluminium and steel.

Al BM	Fe BM	Sheet thickness	IMP thickness	UTS	Joint efficiency	Ref.
AA6068	Mild steel	6 mm	-	160 MPa	53%	[44, 48]
AA5052 H32	HSLA steel	3 mm	1 μm	196 MPa	94%	[47]
AA6061	304 SS	3 mm	1 μm	254 MPa	63%	[52, 53]

Common defects related to Friction Stir Eelding (FSW) of aluminium and steel

In comparison to fusion welding, solid-state welding avoids many of the major problems related to the aluminium, including solidification cracking and porosity. The absence of fusion also removes defects associated with solidification and cooling, which leads to a significant reduction in distortion. However, the solid-state joining techniques are not without flaws, and the most common defects related to FSW of aluminium and steel are caused by non-optimal process parameters or lack of process control [49, 54].

Pores and tunnel defects are commonly observed in FS weldments of aluminium and steel. As shown in Figure 2.14, Dehghani et al. [54] noticed these types of defects when investigating an FS joint of AA5186 and mild steel. They observed that the number of defects increased with higher welding speed. Increased welding speed leads to a shorter time to plasticize and move the material and a decrease in maximum temperature. This results in insufficient plastic deformation of the material and the formation of tunnels and pores. Inadequate removal of the oxide layer along the bond line is also something that can lead to the formation of defects and inadequate bonding along the Al-Fe interface, where increased speed reduces the disruption of the oxide layer. The size and geometry of the tool shoulder have also shown to play an essential role in the formation of defects along the joint bond line [49].

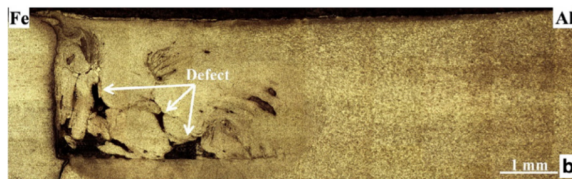


Figure 2.14: Tunnel defects and pores observed in the stir zone (SZ) and along the Al-Fe interface of a friction stir (FS) weld produced of AA 5186 and mild steel. Copied from [54].

The correct penetration depth of the pin is essential during FSW for mixing of the material to occur over the full plate thickness. If the pin is positioned incorrectly or is too short, a root flaw can occur. A root flaw is indicated by an area with a complete lack of bonding. If the area has some bonding, but it is weak, this is known as a "kissing"-bond. "Kissing"-bonds are often difficult to detect but can lead to a significant reduction in strength, and act as initiation points for fracture [49]. Since FSW doesn't utilize an FM, there is an increased chance for insufficient material feeding leading to undercuts and other internal defects [11, 46]. Aluminium and steel have significant differences in flow properties, resulting in

that the material movement in the SZ is more inhomogeneous compared to welds of similar materials, which may be a source for defect formation. Defects related to FSW are often eliminated by increasing the heat input, which is not an optimal solution when joining steel and aluminium [54].

The main difficulty in FSW is the optimization of the process and the process parameters [48, 54]. The different FSW parameters and its combinations are all critical in producing a defect-free joint [47]. As stated by Ramachandran et al. [47], the range of tool rotational speeds and tool tilt angles that are able to create a sound joint is relatively narrow. Besides, these parameters also influence the material flow and the number of steel fragments in the SZ, which are factors that can contribute to reducing the integrity of the joint [13, 51].

2.5 The Hybrid Metal Extrusion & Bonding (HYB) process

2.5.1 Principles behind the HYB technology

The Hybrid Metal Extrusion & Bonding (HYB) process is a new solid-state joining technology that originally was developed for butt joining of aluminium alloys. The idea behind the technology is a method that combines continuous extrusion and solid-state joining. The process uses a filler material addition and plastic deformation to produce sound joints, as reported by among others Grong [10] and Sandnes et al. [11]. The addition of the FM makes to process less vulnerable to undercuts and other weld defects associated with solid-state welding methods. Also, is the process more flexible and able to operate at even lower temperatures compared to existing conventional welding techniques, which contributes to reducing the HAZ strength loss and the amount of residual stress in the weld zone [10, 11].

The principles of continuous extrusion, also known as conform extrusion, is used in the HYB technology to extrude the FM between the two plates to be joined [36]. Extrusion is a process where the cross-section of a metal billet is reduced by forcing it through a die under high pressure, such that the material plastically deforms and flows through. Extrusion requires large forces, and to reduce the deformation resistance the process is often done under hot conditions. The method is usually divided into two basic types, direct and indirect extrusion. The difference between the two is that there is no relative movement between the container and the billet in indirect extrusion, which results in less friction force compared to direct extrusion. Indirect extrusion also requires less power than direct extrusion [55].

Continuous extrusion share some common features with indirect extrusion. In indirect extrusion, the container with the billet is moving towards a stationary die which is embedded in the ram. In continuous extrusion, as illustrated in Figure 2.15, the container is substituted with a rotating extrusion wheel. This wheel contains a slot where the metal is feed in addition to a stationary shoe which consists of an abutment and a die [36]. When the filler wire is fed into the slot, the material is forced to flow against the stationary abutment. A pressure is built up in front of the die, and the material is continuously extruded through the die opening and plastically deformed [10].

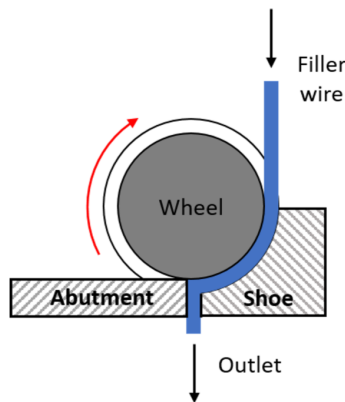


Figure 2.15: Schematic illustration of continuous extrusion. Copied from [36].

2.5.2 The HYB PinPoint extruder

During the latter years, several different tool designs have been tested to find the optimal design for the HYB extruder [36]. The current version is the HYB PinPoint extruder, and a schematic illustration of its main components is shown in Figure 2.16. The extruder is built up around a 10 mm diameter rotating drive pin attached to a drive spindle. The pin is provided with an extrusion head which contains a set of moving dies at the lower conical end. The filler material flows through the dies, due to an imposed friction grip. This friction grip causes the extrusion chamber, with its three moving walls, to drag the filler wire into and through the extruder when the pin is rotating [11, 12, 13, 56].

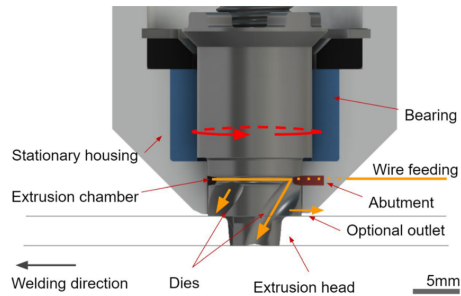


Figure 2.16: Illustration of the main components in the HYB PinPoint extruder. Copied from [11].

A stationary house is covering the pin and extrusion chamber, which causes the filler wire to be kept in place inside the chamber due to a fourth wall. In a similar manner as described during continuous extrusion is the material forced to flow towards an abutment block and finally, due to the pressure built up, extruded through the dies located on the extruder head. The dies have a helicoid-shape, which causes them to act as small "Archimedes screws" when the pin rotates. Thus, preventing a pressure drop on further extrusion of the FM in the direction along the axis of the pin and down into the groove [11, 12, 13, 56].

The permanent housing can if wanted be equipped with an additional die at the rear. This makes it possible to produce a weld face by controlling the aluminium flow in the radial direction, as illustrated in Figure 2.17. Both the width and height of the weld reinforcement can then be controlled and varied. This is, however, dependent on the geometry of the die, where a range from flat to fully reinforced weld face is possible. This is what gives the HYB process the flexibility to produce joints for several different applications, including bead-on-plate deposition, fillet joining, plate surfacing, additive manufacturing, and multi-material joining [11, 12, 56].



Figure 2.17: A dissimilar Al-Fe butt joint produced with the HYB process. The separate die on the housing makes it possible to control the shape of the weld face. Copied from [56].

2.6 Using the HYB process for dissimilar joining

2.6.1 Introduction to dissimilar joining

The HYB technology was initially used to produce simple joints of aluminium alloys. However, as the technology has evolved the method is becoming a multi-functional joining process able to create different joint configurations in addition to hybrid joints consisting of different base materials [12, 13]. At present, as shown by Grong et al. [12] up to four different materials have been joined by the use of the HYB PinPoint extruder and AA6082 as filler wire. The addition of the filler material has proven to be advantageous when it comes to joining the different combinations of base materials.

The first attempt of joining steel and aluminium showed promising results regarding the potential of the process for joining of these challenging materials. Therefore, a new generation of the HYB butt weld consisting of AA6082-T6 and S355, with AA6082-T4 as filler wire, were produced. These two generations were produced with the same pin and steel housing as the ones used during Al-Al butt welding. Filippo Abbatinali [57] characterized the first attempt, and Matteo Manfrotto [14] did basic mechanical characterization of the new improved version of the joint. His work is the basis for this thesis.

2.6.2 Working principle during aluminium-steel joining

When joining aluminium and steel with the HYB process, the extruder head is clamped against the two plates to be joined. The plates are placed at a certain distance from each other such that a groove is formed between them. A schematic illustration of the location of the pin in the weld groove for the first produced Al-Fe HYB butt weld is shown in Figure 2.18. From the figure, it can be seen that the steel BM is machined to form a slope that is parallel to the pin. This is done to avoid contact between the pin and the steel plate during the welding operation [13].

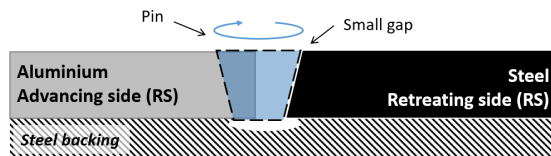


Figure 2.18: Schematic illustration of the pin and its location in the weld groove during production of the first HYB Al-Fe butt weld. Copied from [13].

The aluminium BM is placed such that the pin is slightly larger than the groove. This causes direct contact between the pin and the sidewall of the aluminium and thus proper removal of the oxide layer. During welding, the HYB PinPoint extruder moves along the welding interface at a constant speed. The extruder feeds the aluminium FM into the weld groove and mixes it with some of the aluminium BM, due to the rotating motion of the pin. Most of the aluminium flows from the top of the weld downwards along the steel side and consolidates when it meets the steel backing [13]. Similar as for FSW is also the HYB process defined as asymmetrical. The force from the extruder head will be different on the AS compared to the RS [11]. A combination of oxide dispersion, surface expansion, shear deformation, in addition to pressure, creates metallic bonding on the aluminium side of the joint. On the steel side, however, is it reasonable to believe that the formation of IMCs along the bond line is the primary bonding mechanism similar to other welding techniques used for joining of the two materials [13].

During HYB welding, a large number of processing parameters have to determine. These parameters play a vital role in determining the final properties of the joint. An in-depth analysis of these parameters can be found in the PhD thesis of Ulf Roar Aakenes [36]. For butt joining of 4 mm steel and aluminium plates, the rotational speed of the pin is approximately 400 RPM and the welding speed 6 mm/s. The temperature does not exceed 400° (Ø. Grong, Personal Communication, 2019), which is below the operating temperature that is reported for FSW [11].

2.6.3 Mechancial characterization of the first aluminium-steel HYB butt weld

The first attempt of the dissimilar HYB weld of aluminium alloy 6082-T6 and structural steel 355 was produced as explained above and fully characterized by Abbatinali [57]. Two plates with dimensions 4 mm × 240 mm × 55 mm were joined with a Ø 1.2 mm wire consisting of AA6082-T4. The chemical composition of the BMs and FM are the same as explained in the experimental part of this thesis (see Section 3). Further information about the joining conditions and configuration can be found in [57].

Four samples were cut from the welded plate and machined into specimens used for tensile testing. Other samples were utilized for hardness measurements and microscopical analysis. These samples were prepared according to standard sample procedures. Dimensions and an in-depth description of the preparation procedure can be found in [57]. In the following, the main results from the hardness measurements, tensile testing, and microscopical investigation will be given.

Microstructure and hardness measurements

The hardness data for the mid-section of the joint is presented in Figure 2.19. The figure shows the hardness profile on both sides of the joint in the transverse direction. Two reference values were obtained from the BMs, 111.5 HV and 157.2 HV for the aluminium and steel, respectively. The dotted horizontal line represents these values in the figure. Remark that the results showed is the mean value between two different test series along the same path.

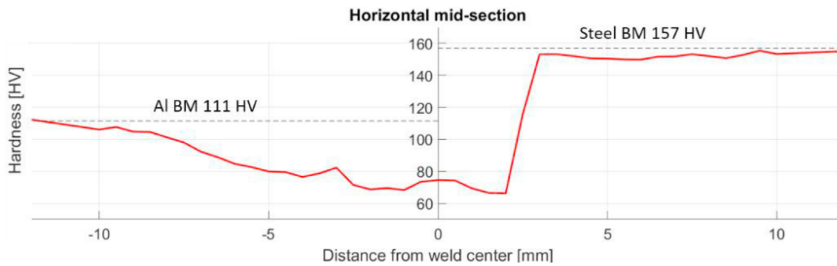


Figure 2.19: Transverse hardness profile of the mid-section of the first produced HYB butt weld of aluminium and steel. Copied from [13].

As shown in Figure 2.19, the steel reaches the value of the steel BM almost immediately, shown by the clearly step between the steel and EZ. Thus, indicating that the steel is unaffected by the joining operation. In the transition between the aluminium BM and FM, the minimum hardness of the joint is found. This point is located approximately 2 mm from the weld center and has a value of roughly 66 HV, which is 57% of the value of the aluminium BM. Full recovery of the hardness of the BM on the aluminium side is reached after approximately 12 mm.

In addition to the hardness in the horizontal direction, vertical measurements were taken along the weld mid-section. Figure 2.20 shows an optical macrograph of the cross-section of the HYB joint in addition to the hardness paths. The different weld zones and the material flow pattern of the aluminium BM and FM are clearly shown in the figure. The steel, however, does not show signs of deformation. The lower part of the weld groove contains mostly aluminium BM while the FM dominates the upper region. Regarding the hardness in the vertical direction, the hardness reaches its lowest value in the area mainly containing the aluminium BM and increases towards the top of the weld. No defects, including pores and tunnels, were detected in the joint [13, 57].

Tensile properties and crack path

The ultimate tensile strength (UTS) of the four transverse tensile specimens is presented in the bar charts in Figure 2.21. The different specimens were sampled

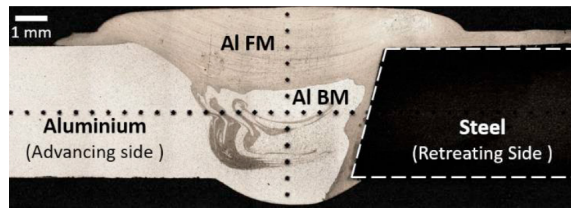


Figure 2.20: Optical macrograph of the cross-section of the first produced Al-Fe HYB butt joint, showing the material flow of the aluminium base and filler material. Copied from [13].

from different positions of the welded plate, which is indicated by numbers in the figure. A low number means that the sample is taken at the beginning of the plate while a higher refers to a position closer to the end. The results show that the specimens at the center of the plate had a lower tensile strength compared to the specimens located closer to the end. The highest tensile strength obtained corresponds to a joint efficiency of 45%.

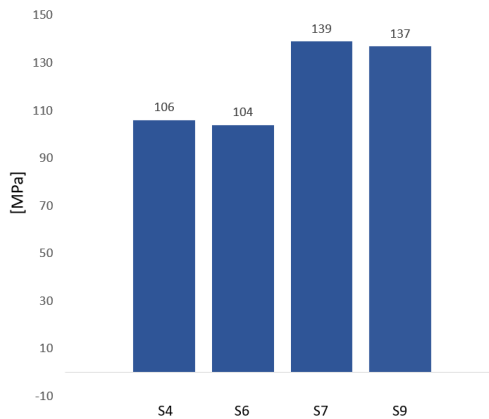


Figure 2.21: Tensile strength measured for the four tensile specimens tested of the first dissimilar HYB butt weld of aluminium and steel. Data extracted from [57].

All the specimens were observed to fracture in a similar manner. The fracture started in the bonding between the aluminium and steel and then continued along the aluminium FM, as shown in Figure 2.22. The fracture mechanism was, therefore, a combination of brittle and ductile failure, where the ductile failure mechanism is dominating. This is the same fracture path as the one observed by Ramachandran et al. [47] in their research on an FS weld consisting of AA5052 and HSLA steel. As stated by Berto et al. [13], this indicates that the first produced

HYB weld of aluminium and steel has good bonding along most of the aluminium and steel bond line. The fracture path also corresponds to the hardness measurements, where the weakest part of the joint is inside the EZ.

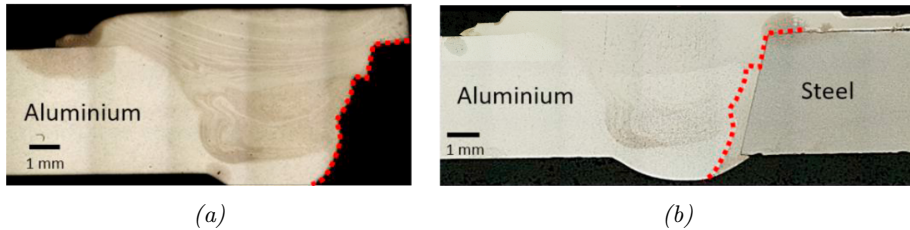


Figure 2.22: The fracture path in (a) the broken tensile specimen and (b) its location in the EZ in the first produced Al-fe HYB butt weld. Copied from [13].

Intermetallic compounds formation

A sample in the middle of the welded plate was used to look at the possible IMCs formation. Both scanning electron microscope (SEM) at high magnification and energy dispersive x-ray spectroscopy (EDS) were utilized. However, even at the highest magnification in the SEM, there were no signs of IMCs along the bond line. This indicates that the IMP layer has to be extremely thin compared to what has been observed for other conventional welding techniques.

2.7 Digital image correlation (DIC) analysis

DIC is an optical method that can store images of the surface of an object. Image analysis is performed to obtain full-field shape, deformation and/or motion measurements [58]. Different types of patterns can be used, including lines, dots, and grids. A high-resolution digital camera is utilized during tensile testing to evaluate the changes that occur. The DIC algorithm involves comparing a deformed image of the specimen to a reference image, which is taken when no load is present. All the deformed images will show a different random dot pattern relative to the reference image, as shown in Figure 2.23, these differences between the patterns are calculated by correlating the pixels of the reference image and the deformed image [59]. From this, field maps of principal strain can be obtained to evaluate how the strain localizes and changes during the tensile test.

There exist different DIC approaches, the subset-based which uses the Newton-Raphson optimization and the "finite-element" based approach [60]. The eCorr software developed by Egil Fagerholt [60] utilizes the "finite element" approach,

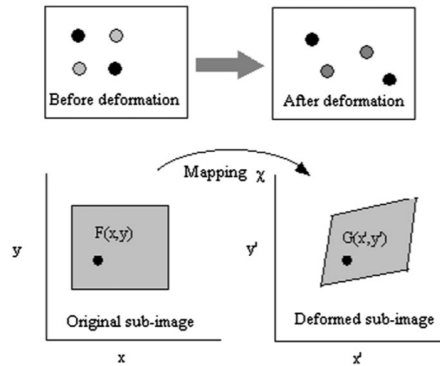


Figure 2.23: The principle of digital image correlation (DIC). Copied from [59].

where the correlation problem is formulated as a finite-element decomposition on a mesh consisting of Q_4 elements. The mesh as illustrated in Figure 2.24, has four nodes (1-4) with two degrees of freedom (u_n, v_n). For each element, eight parameters (4 nodes \times 2 degrees of freedom) need to be optimized in the correlation function. This approach has relatively high computational cost but ensures a continuity of the displacement across the element boundaries [60]. In addition to obtaining the strain history of selected elements or nodes can virtual extensometers be used to get local and global material parameters. This is done by the use of vectors and comparing the elongation of the vectors in the reference and current (deformed) image.

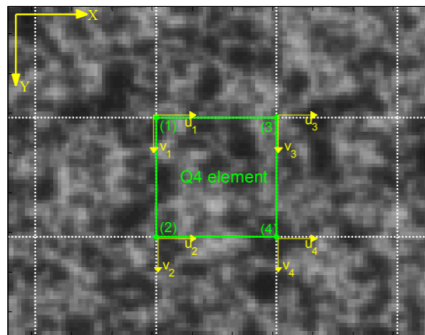


Figure 2.24: A Q_4 element within a mesh using the "finite-element" based digital image correlation (DIC) approach. Copied from [60].

3 Experimental

3.1 Materials

3.1.1 Base materials (BM)

The base materials (BM) used for the welding trial were 4 mm rolled plates of aluminium alloy 6082-T6 and 4 mm rolled plates of structural steel 355. Their chemical composition are given in Table 3 and Table 4, while the corresponding material certificates can be found in Table A.1 and Table A.2 in Appendix A. Note that, both plates were received from an external supplier and therefore no further information about the heat treatment and homogenization schedules are available.

Table 3: Chemical composition (wt.%) of the AA6082-T6 aluminium used as base material.

Alloying element (wt.%)									
Si	Fe	Cu	Mn	Mg	Cr	Zn	Ti	Other	Al
0.90	0.45	0.06	0.42	0.80	0.02	0.05	0.02	0.03	Balance

Table 4: Chemical composition (wt.%) of the S355 structural steel used as base material.

Alloying element (wt.%)															
C	Si	Mn	P	S	Al	Nb	V	Ti	Cu	Cr	Ni	Mo	N	B	Ceq
0.067	0.02	0.69	0.01	0.005	0.040	0.014	0.008	0.001	0.028	0.05	0.05	0.009	0.005	0.0001	0.2

3.1.2 Filler material (FM)

The filler material (FM) used for joining was a $\text{\O}1.2$ mm wire of aluminium alloy 6082-T4, with chemical composition, as shown in Table 5. The corresponding material certificate is given in Figure A.3 in Appendix A. The wire was produced by HyBond AS and was made from a DC cast billet provided by Norsk Hydro ASA. The DC billet was homogenized, hot extruded, cold drawn, and shaved down to the final wire dimension. The applied homogenization conditions are described in Table 6.

Table 5: Chemical composition (wt.%) of the AA6082-T4 aluminium used as filler material.

Alloying element (wt.%)										
Si	Fe	Cu	Mn	Mg	Cr	Zr	Ti	B	Other	Al
1.11	0.20	0.002	0.51	0.61	0.14	0.13	0.043	0.0.6	0.029	Balance

Table 6: Homogenization conditions for the AA6082-T4 DC cast billet.

Heat rate [°C/h]	Holding temp. [°C]	Holding time [h]	Cooling rate [°C/h]
200	540	2..25	300

3.2 Welding conditions

The plate dimensions used for the HYB joining trial were 4 mm × 240 mm × 120 mm, respectively. A schematic illustration of one plate with the corresponding dimensions is shown in Figure 3.1. The drawing also includes the rolling direction, which is the same as the welding direction during the joining trial.

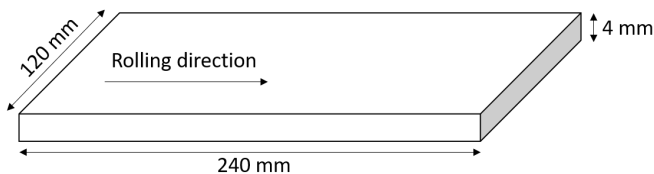


Figure 3.1: Schematic illustration of one of the base material plates used in the HYB joining trial, including both the plate dimensions and welding/rolling direction. Note that, the illustration is representative for both base material plates used in the joining trial.

Single pass butt joining of the two base plates was conducted by HyBond AS, using a weld groove with a root opening of 2 mm. Prior to the welding operation, the steel side was machined to form a Y-groove to ensure that the pin is not in contact with the steel BM. The aluminium side, on the other hand, was left without any surface preparation. This is illustrated in Figure 3.2a. Both surfaces were cleaned in acetone prior to joining. Figure 3.2b shows the pin location in the weld groove, as well as the welding direction during the joining operation. As can be seen from

the figure, the aluminium is located on the advancing side (AS) of the joint while the steel is then located on the retreating side (RS).

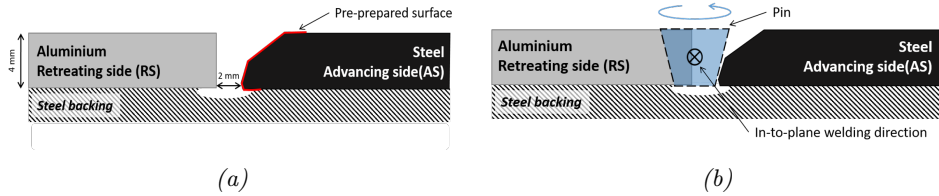


Figure 3.2: Schematic illustration of the (a) surface preparation and groove configuration prior to the welding operation, and (b) pin-in-groove situation during welding.

During welding, CO_2 -gas was used for cooling, using a gas flow rate of 160 g/min. The total power consumption during the process is approximately 2973 W, and the temperature in the outer skirt of the extruder is about 400 °C. The main parameters used during the welding trial are listed in Table 7.

Table 7: Summary of the main welding parameters used in the HYB joining of AA6082-T6 and S355.

Welding parameters			
Pin rotation [RPM]	Welding speed [mm/s]	Feed rate [mm/s]	Gross heat input [kJ/mm]
400	6	146	0.33

3.3 Sample preparation and metallographic examination

3.3.1 Sample sectioning

Transverse samples were cut from the weld plate and numbered, as illustrated in Figure 3.3. The samples used for the metallographic investigation are highlighted in pink in the same figure.

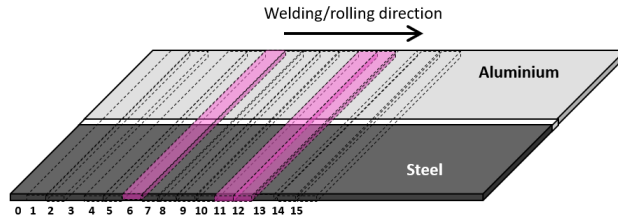


Figure 3.3: Schematic illustration of the plate sectioning and numbering of the specimens. The specimens used for the microscopical examination are highlighted in pink.

3.3.2 Sample preparation

Samples used for the microscopical examination were cut into smaller parts, having a length of about 36 mm, including both the steel and aluminium side of the joint. Then, the samples were cold mounted in ClaroCit acryl resin between two pieces of steel to avoid "a round edge effect" that may easily occur when two materials having a large difference in hardness are ground and polished. This, in turn, may influence the quality of the macro- and micrographs taken of the prepared surfaces and need to be avoided. The surface preparation of the specimens was carried out in the following steps.

First, the mounted samples were ground by the use of SiC grinding papers with an increasingly finer abrasive size (P80, P120, P220, P500, P1000, P4000). During the grinding process water was used as a lubricant, and the samples were cleaned in ethanol after each step. After grinding, the specimens were polished using a polishing disk and diamond paste suspension of 3 and 1 μm . In this operation, a DP Lubricant Blue was used as lubricant. Between each step, the samples were cleaned in an ultrasonic bath and ethanol.

The samples used for analysis in the scanning electron microscope (SEM) were ground as previously explained. Then they were polished using a colloidal silica suspension (OP-S Suspension) for 40 min to minimize the height difference between the two materials. Finally, the samples were thoroughly rinsed in water.

In order to reveal the macrostructure of the dissimilar HYB joint, the sample was immersed in an alkaline sodium hydroxide solution, containing 1 g NaOH and 100 ml H_2O , for about 3 min. Note that this process only reveals the macrostructure of the aluminium, whereas the steel is unaffected.

To reveal the microstructure of the two base materials (Al BM and Fe BM) and the dissimilar HYB joint, different etching methods were utilized. Anodization by the use of Bakers solution, containing 5% HBF_4 and 95% H_2O , was used to reveal the microstructure of the Al BM and Al part of the HYB joint. The steel side of the joint was coated with nail polish to prevent it from dissolving during the anodization process. This was applied by hand, using the including brush, and allowed to completely dry before exposure to the electrolytic solution. The samples were immersed in the solution for 90 s, using a current of 1.0 A and a voltage of 20 V. Then, the samples were rinsed in water and cleaned with ethanol. Finally, the coating on the steel was removed using acetone.

In order to reveal the microstructure of the steel, the specimen was chemically etched in 5% Nital for about 15 to 20 s, followed by cleaning in both water and ethanol.

3.3.3 Optical microscopy

The microstructure of the two base materials and the HYB joint were examined in different types of light optical microscopes (LOM). The microstructure of all the samples was investigated perpendicular to the rolling direction. Leica MEF4M optical microscope was used to examine the microstructure of the aluminium. This by using lens magnification of 2.5x, together with polarized light and a subparallel lambda plate. Alicona infinite focus confocal microscope was used to look at the entire weld macrostructure, in addition to the steel microstructure.

3.4 Scanning electron microscope (SEM)

The bond line of the HYB joint along the Al-Fe interface, as well as the fracture surface of selected broken tensile specimens, were examined in a scanning electron microscope (SEM), of the Quanta FEG 650 type. The acceleration voltage was set to 20 kV, and the working distance was approximately 10 mm. In addition to standard SEM analysis, backscatter electron (BSE) analysis was conducted in the same machine, using a BSE detector containing a phosphor screen.

In the standard SEM analysis, the topography contrast in the specimens is clearly visible, while the BSE makes it possible to see the contrast of the different elements in the sample. During BSE, heavier atoms backscatter more electrons than lighter atoms. Therefore, materials with high density (such as steel) will reject more electrons compared to a material with lower density (such as aluminium) and appear

lighter in the BSE images. This also makes it possible to see the microstructure of the steel containing ferrite and pearlite, with different carbon content and density, respectively.

3.5 Tensile testing

The transverse samples used for the tensile testing were taken from different locations in the welded plate, as illustrated in Figure 3.4. As there are no standard methods available for tensile testing of dissimilar materials, subsize specimens were prepared in accordance to ASTM standard E8/E8M-16a [61]. Two types of tensile specimens were prepared, one set having the as-welded shape and one set where the weld is flush-machined, as shown in Figure 3.5a and Figure 3.5b. This was done in order to reveal the effect of the reinforcement on the joint strength.

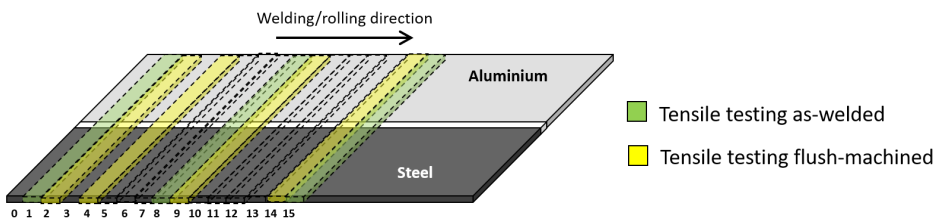


Figure 3.4: Schematic illustration of specimen location and numbering of the tested tensile specimens.



Figure 3.5: Photographs of selected tensile specimens prior to testing (a) flush-machined and (b) as-welded.

Only three of the tensile specimens were tested using the DIC measurements system, that is specimen number 2, 4, and 8. The other specimens were tested using conventional measuring equipment and were conducted by Matteo Manfrotto [14]. These results can be found in Table 10 in Appendix B. In the following, only the specimens tested using the DIC equipment will be covered. Tensile testing of these specimens was carried out in room temperature, using an Instron 5985 hydraulic test machine with a load cell of 250 kN. The test speed was set to $v = 1.5$ mm/min which corresponds to a strain rate of $\dot{\epsilon}_{nom} = 10^{-3} s^{-1}$. The experimental set-up

for DIC testing is shown in Figure 3.6. As can be seen from the figure, one of the specimens (S2) was tested with an extensometer placed on the aluminium side, having a gauge length of 10 mm.

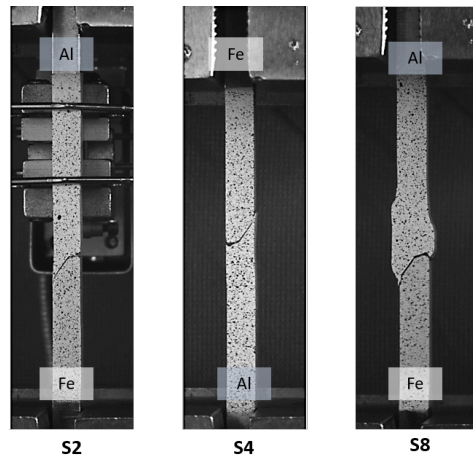


Figure 3.6: Pictures of the experimental set-up used for DIC testing. Note that, specimen S_4 is tested with the steel side on top [14].

3.6 DIC analyses

Post-processing of the DIC results was conducted by the use of the finite element based software eCorr created by Egil Fagerholt [60]. First, a quadratic mesh having an element size of approximately 20×20 pixels were added to a reference picture before any deformation had occurred in the specimen. This is shown by the photograph in Figure 3.7. Then, in specimen 2, the elements that cover the extensometer were deactivated and thus, excluded from the analysis. From this, field maps of the principal strain can be extracted from the software.

For all DIC specimens tested, two virtual extensometers (vectors) were applied in the software using a gauge length of 30 mm, as shown in Figure 3.7. This gauge length was chosen based on the transverse hardness measurements made by Matteo Manfrotto [14] (see Figure 3.8a). In order to capture the entire weld zone and obtain the global stress-strain values of these specimens.

The hardness measurements in Figure 3.8a were also used to determine the extension of the different weld zones in the HYB joint. As can be seen from the graph, the lowest hardness value is found in the HAZ approximately 5.5 mm from the

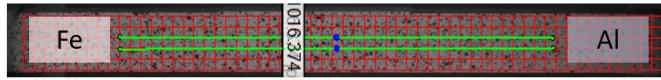


Figure 3.7: Photograph of specimen *S4* showing the applied mesh and the two virtual extensometers used to analyse the tensile test data.

weld center. In order to get local values of the HAZ material properties, two virtual extensometers with a gauge length of 6 mm were placed across the weak zone (see Figure 3.8b). From this, the local tensile properties were extracted. Similarly, the local properties for both the Al BM and Fe BM were obtained.

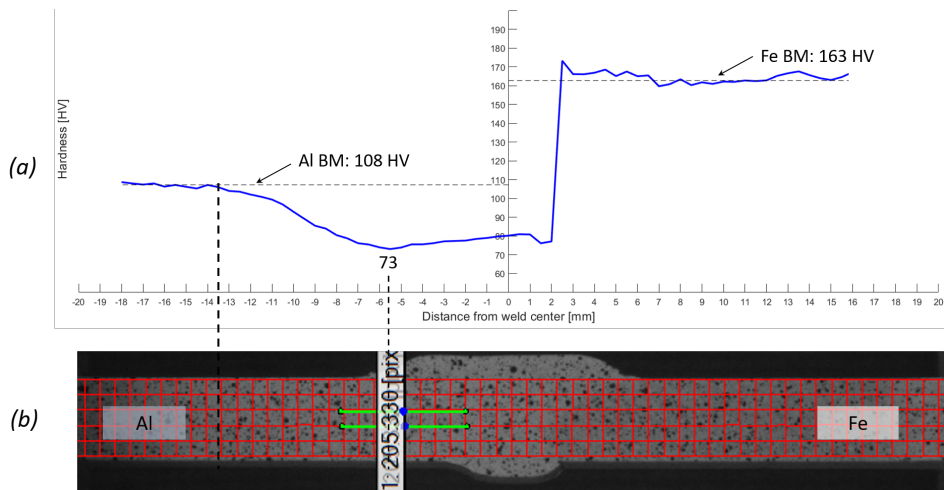


Figure 3.8: (a) The HYB joint transverse hardness profile measured along the horizontal midsection of the joint [14]. (b) Photograph of specimen *S8* showing the location of the virtual extensometers used to extract local tensile properties from the heat affected zone (HAZ).

4 Results

4.1 Microscopic examination

4.1.1 Base materials

Figure 4.1 shows overview pictures of the aluminium and steel microstructure taken transverse to the plate rolling direction. As can be seen from Figure 4.1a, the AA6082-T6 base material shows a clear rolling structure, having small equiaxed grains in the center which gradually increase in size towards the top and bottom of the plate. The grain size was measured to be between 50 and 200 μm .

Figure 4.1b shows the microstructure of the S355 base material. It shows a fine equiaxed (polygonal) grained microstructure that consists of both ferrite (light phases) and pearlite (darker phases). Due to the high magnification, no differences in grain size was observed due to the rolling operation. The grain size was measured to be between 5 and 15 μm .

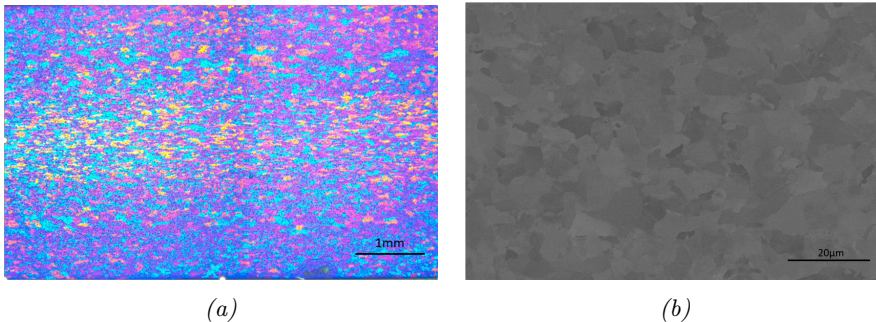


Figure 4.1: Optical micrographs showing the microstructure of the base materials used in the welding trial taken transverse to the plate rolling direction. (a) The AA6082-T6 at low magnification (2.5x) and (b) the S355 at high magnification (2000x).

4.1.2 The HYB joint macrostructure

An overview of the dissimilar Al-Fe HYB butt weld macrostructure is shown in Figure 4.2. From the figure, it can be seen that both the aluminium base and filler material (Al BM and FM) are heavily deformed and the Al FM flow pattern is clearly visible. On the other hand, the steel is not affected by the joining operation

when it comes to plastic deformation. Moreover, it is evident from the flow pattern that most of the Al FM flows downward along the steel side of the weld groove and forms the Al-Fe interface.

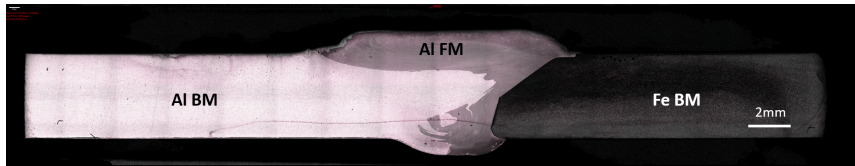


Figure 4.2: Optical macrograph showing an overview of the Al-Fe HYB joint macrostructure.

In the dissimilar Al-Fe HYB joint, two different types of bonding occur. That is metallic bonding between the aluminium base and filler materials, and intermetallic bonding between the aluminium and the steel, as shown in Figure 4.3a and 4.3b, respectively. From Figure 4.3a, it can be seen that there is a smooth transition between the aluminium base and filler material along most of the interface, which indicates good bonding. However, in the weld root (red arrow), there is a region along the bond line of about $308\ \mu\text{m}$ that appears more distinct, indicating insufficient bonding. Moving on to Figure 4.3b, a close-up of the Al-Fe interface is shown. As can be seen from the figure, some small irregularities can be observed on the steel side. This may either be a result of the pre-machining of the steel surface, or it may indicate that there is some deformation of the steel due to contact with the pin during joining. However, further research is required to determine the origin of these observations.

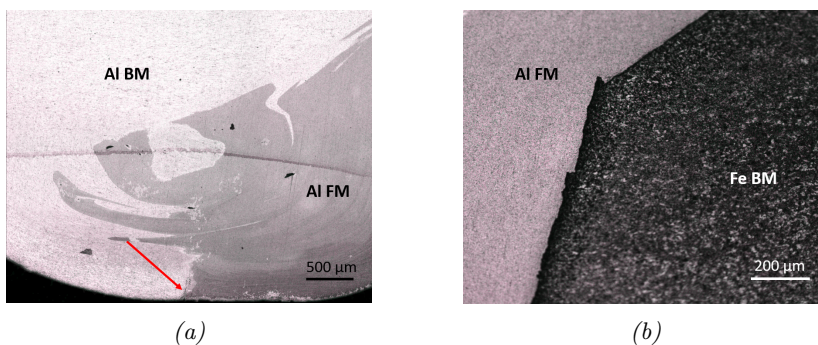


Figure 4.3: Optical micrographs showing the two different types of bond-lines that occur in the Al-Fe HYB joint. (a) Bonding between the aluminium base and filler material, and (b) dissimilar bonding between the aluminium filler material and the steel.

4.1.3 The HYB joint microstructure

Figure 4.4 shows an overview of the Al-Fe HYB joint microstructure taken transverse to the welding direction. Obviously, the microstructure changes across the joint, and it is observed that the extrusion zone (EZ) contains finer grains compared to that of the base material. This may reflect the differences in chemical composition between the FM and aluminium BM, as well as the amount of deformation the materials undergo in these zones. Moreover, elongated and finer grains are observed in the transition between the BM and the EZ as a result of substantial deformation. In Figure 4.5, the microstructure of the steel part of the Al-Fe HYB joint is shown close to the bonding line. From the micrograph, no apparent signs of microstructural changes could be observed on the steel side of the weld.

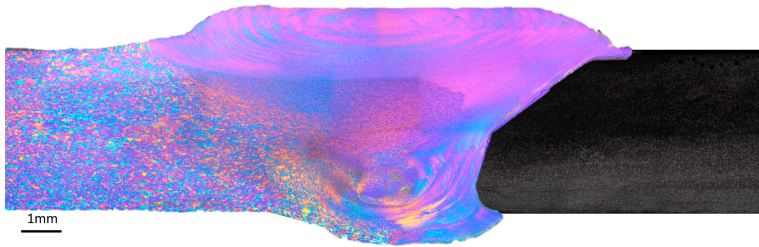


Figure 4.4: Optical micrograph showing an overview of the Al-Fe HYB joint transverse microstructure of specimen S6. Note that, only the microstructure of the aluminium is visible.

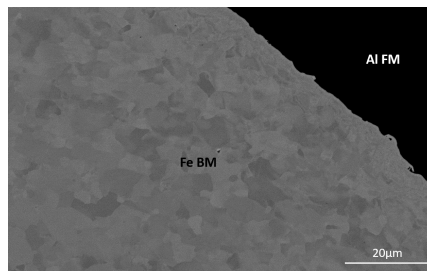


Figure 4.5: Optical micrograph showing the microstructure of the steel side of the Al-Fe HYB joint of specimen S11 at high magnification (2000x).

The grain refinement observed in the EZ and transition area between the HAZ and EZ indicates increased strength in these areas, in accordance with the Hall-Petch relation. In addition to strengthening achieved by strain hardening caused by the severe plastic deformation. However, the measured hardness profile along

the horizontal mid-section, given in Figure 3.8 in Section 3.6, shows that regardless of the microstructural changes the minimum hardness is found in the transition between the HAZ and EZ. The decreased strength in this area is mainly believed to be caused by heat localization, and growth or dissolution of precipitates in the aluminium. From the hardness measurements, the steel reaches the value for the BM hardness almost immediately, which corresponds to the microstructural results.

Tunnel defects and cracks were observed during the microstructural examination. Insufficient material flow of the FM, gas pores, or a lack of heat can be reasons why these defects form at different positions in the EZ. Tunnel defects are as mentioned commonly seen during solid-state joining. Figure 4.6a shows such a defect with a length of approximately $190\ \mu\text{m}$. Moreover, there were also steel fragments observed inside the EZ, as shown in Figure 4.6b. If the pin comes in contact with the steel surface, the forces acting on the surface can be large enough to remove particles that then get stirred into the weld zone. Most of the fragments were measured to be positioned at a distance of between 1.3-2.4 mm away from the Al-Fe interface. Which is in good correspondence with the width of the extrusion head and EZ. However, it has to be considered that the preparation process also can explain these fragments. Additional images of the observed defects and the steel fragments can be seen in Figure C.1 and Figure C.2 in Appendix C.

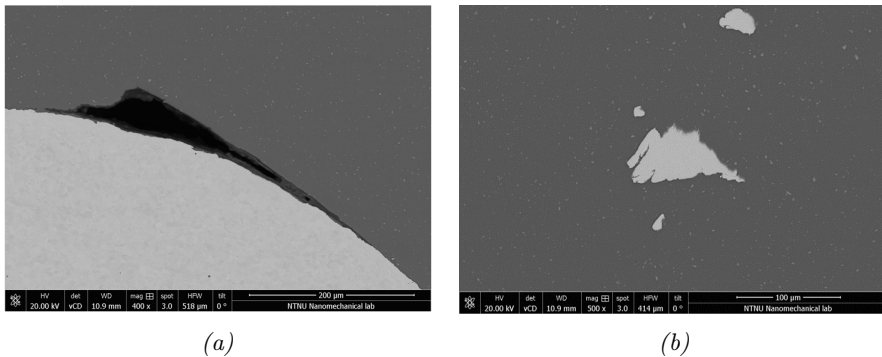


Figure 4.6: Optical micrographs showing an observed (a) tunnel defect and (b) steel fragments in the Al-Fe HYB weld.

4.2 Examination of the Al-Fe interface

To reveal any remarkable formation of intermetallic phases along the Al-Fe interface of the HYB joint, a more thorough analysis using BSE was carried out. Figure 4.7 shows an overview of the bond line at low magnification (50x) taken in the center of the specimen. At low magnification, there is no sign of any IMPs along the bond line. However, it is observed that the bond line changes its appearance from straight (top) to wavy (bottom), which gives rise to a longer nominal interface in the lower part of the weld.

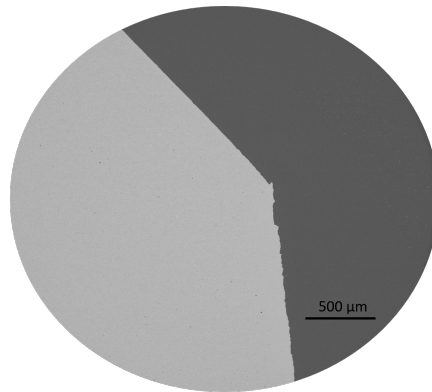


Figure 4.7: Low magnification (50x) overview of the Al-Fe bond line of the HYB joint taken in the weld center.

Figure 4.8 shows BSE micrographs at higher magnification (2000x) of selected regions of the Al-Fe bond line. As can be seen from Figure 4.8a and Figure 4.8b, there are some areas at the top and the root region, respectively, where insufficient bonding occurs. However, in the central part of the joint, there seems to be sufficient bonding between the two materials, see Figure 4.8c. Additional micrographs at low magnification can be found in Figure E.1 in Appendix E.

The bond line in the central part of the weld was examined at an even higher magnification. Figure 4.9 shows that at a magnification of 5000x, there is no sign of any IMCs along the Al-Fe interface. Similar observations were made by Abbatinali [57] in his work examining the first produced dissimilar Al-Fe HYB joint.

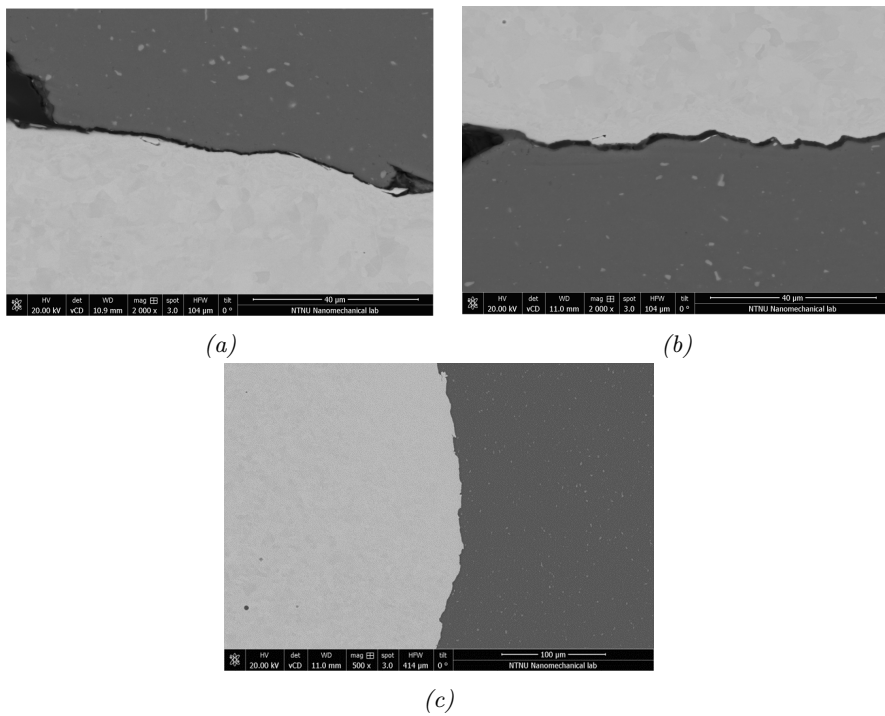


Figure 4.8: BSE micrographs at high magnification (2000x) showing the (a) top, (b) bottom and (c) middle part of the Al-Fe bond line of the HYB joint.

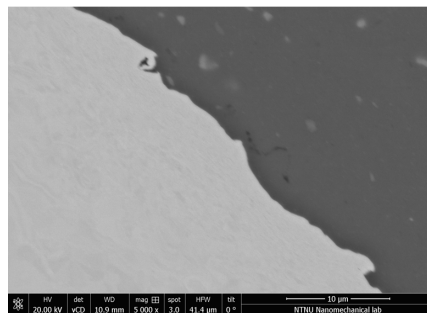


Figure 4.9: BSE micrograph at high magnification (5000x) of the central part of the Al-Fe bond line of the HYB joint.

4.3 Tensile properties

4.3.1 Global properties of the dissimilar HYB joint

As previously explained in Section 3.5, two virtual extensometers were applied to the mesh with a gauge length of 30 mm to measure the global strength of the joint. In the following, only one of these is presented, whereas a graphical representation of both can be found in Figure D.1 in Appendix D. The measured stress-strain curves for the specimens are shown in Figure 4.10. Note that, the stress-strain curve for specimen 8 starts at approximately 60 MPa, indicating that the pre-load after clamping was not properly removed prior to testing. For all specimens tested, the final fracture occurred along the Al-Fe interface.

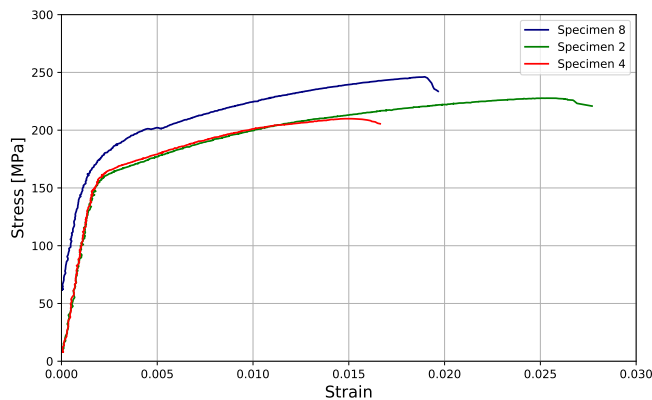


Figure 4.10: Measured stress-strain curves from the tensile testing using DIC and virtual extensometers.

From the stress-strain curves, the 0.2% offset yield strength and modulus of elasticity (E-module) were calculated. Due to large scatter in the elastic region of the stress-strain curves, linear regression was used to calculate the E-module. The average value for the E-module was found to be 90.44 GPa, which is in between the generally accepted values of 70 GPa and 210 GPa for aluminium and steel, respectively. This corresponds with the superposition principle used for calculating the stiffness of composite materials, indicating a strength contribution from both of the base materials on the resulting joint stiffness. The calculated E-modules for all the specimens tested using virtual extensometers can be found in Table 11 in Appendix D.

The resulting average tensile properties for the three DIC specimens, together with the aluminium base material properties obtained from Sandnes [50], can be found in the bar charts in Figure 4.11. Additional tensile properties for all the test samples, using the virtual extensometers, can be found in Table 12 in Appendix D. As seen from the figure, all the welded samples reach lower values compared to that of the aluminium base material. The specimen with reinforcement (i.e., specimen 8) reaches a yield and tensile strength of about 201 MPa and 246 MPa, respectively, whereas both the flush-machined specimens show lower values. For specimen S8 this equals a joint efficiency of 80 %, which is significantly higher than that obtained for the first produced Al-Fe HYB weld (45%). However, the average tensile strength for the three tested specimens equals 227.96 MPa and corresponds to a joint efficiency of approximately 75%.

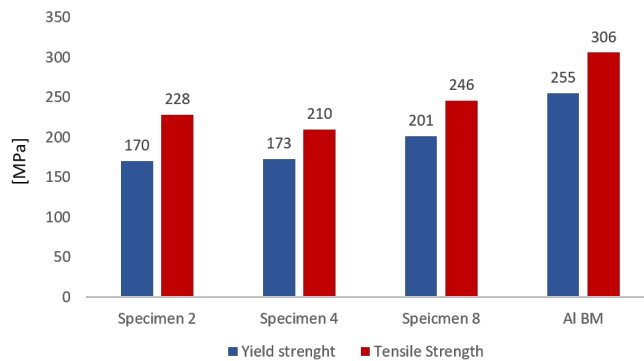


Figure 4.11: Measured average tensile properties for the three Al-Fe HYB tensile specimens. The aluminum base material properties are obtained from Sandnes [50].

4.3.2 Local properties of the HAZ

The local tensile properties of the HAZ were calculated by the use of two virtual extensometers (6 mm) on each specimen. The average value for the 0.2% offset yield strength and the E-module were found to be 172 MPa and 43.5 GPa, respectively. Linear regression was used to obtain values for the E-module. The measured stress-strain curves for the two virtual extensometers in the HAZ obtained from specimen 2 are shown in Figure 4.12. As seen from the figure, the two curves are almost identical. This indicates that the different positions of the extensometers in the thickness direction does not influence the resulting stress-strain curves. Additional stress-strain curves for all the other specimens can be found in Figure D.2 and Figure D.3 in Appendix D.

The local yield strength in the HAZ is remarkably similar to the global yield strength of the weld. This indicates that the HAZ is the area of the weld that dominates the global yield properties of the weld. Additional values for the E-module and yield strength in the HAZ for all tested specimens using virtual extensometers can be found in Table 14 and Table 13 in Appendix D.

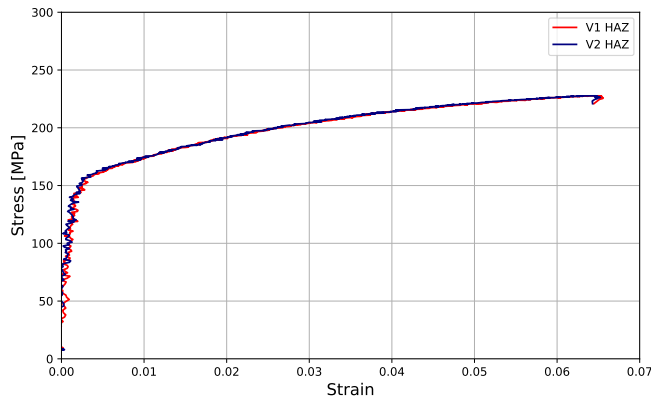


Figure 4.12: Example of measured stress-strain curves during tensile testing of specimen 2 with extensometers positioned in the HAZ.

Virtual extensometers were positioned in the aluminium BM, HAZ/EZ, and steel BM of the weld, as illustrated in Figure 4.13, in order to extract local material properties. These give an indication about how the materials in the different weld zones interact and deform during tensile testing. Due to the positioning of the physical extensometers used during testing of specimen 2, which covered significant parts of the aluminium BM, this specimen is not considered further.

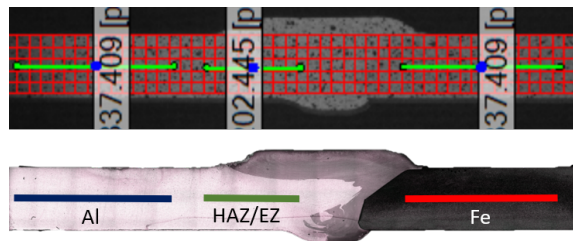


Figure 4.13: Illustration of the positioning of the virtual extensometers in the aluminium BM, HAZ/EZ, and steel BM.

Figure 4.14 shows the local stress-strain curves for the aluminium BM (blue curve), EZ/HAZ (green curve), and steel BM (red curve) for specimen 8. As can be seen from the figure, the steel is in the elastic region during the test, whereas small

deformations of the Al BM can be observed. Still, most of the deformations occur in the EZ/HAZ, indicating that this is the weakest part of the joint. Corresponding curves for specimen 4, can be found in Figure D.4 in Appendix D.

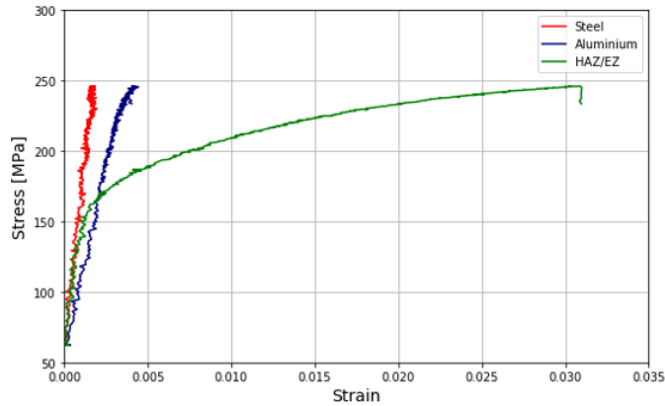


Figure 4.14: Example of measured stress-strain curves during tensile testing of specimen 8, for extensometers positioned in the aluminium BM, EZ/HAZ and steel BM.

4.4 DIC analysis of the tensile specimens

The fracture propagation and behavior of the weld during tensile testing were studied by the use of DIC analysis. The images obtained from the DIC were used to identify the crack and its propagation path, which is not possible to detect by visual inspection. In addition, the DIC analysis was used to analyse the evolution of the strain concentration in the specimen during testing. In the following, the main findings from the analysis of specimen 2, 4, and 8 will be presented.

Specimen 2

Figure 4.15 shows three pictures of specimen 2 at different stages during tensile testing; a) before testing (no load applied), b) at the point of crack initiation and c) at the point of final fracture. As can be seen from Figure 4.15b, the crack initiates in the root region at the Al-Fe interface. The crack then continues to propagate as the load increases and results in ultimate failure close to the Al-Fe interface, as shown in Figure 4.15c.

From the eCorr analysis, the plastic strain distribution can be extracted at different steps during tensile testing, as shown in Figure 4.16. Obviously, the strain localization changes during the test as the load is increasing. At an early stage

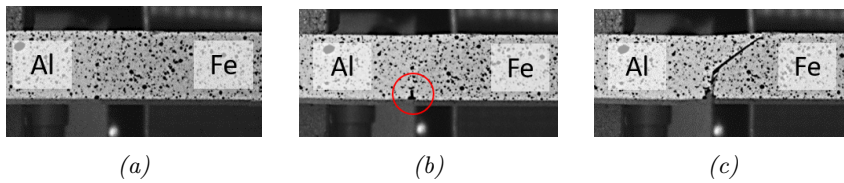


Figure 4.15: Fracture propagation of specimen 2 at different stages during tensile testing; (a) before loading, (b) at the point of crack initiation and (c) final fracture.

during testing, it was observed that the strains start to localize in the HAZ and in the root at the Al-Fe interface, as seen in Figure 4.16a. When the load increased, there is seen to be a "competition" between the HAZ and the root crack, before most of the strain accumulates at the root crack and leads to the final fracture along the Al-Fe interface, as shown in Figure 4.16b and Figure 4.16c, respectively.

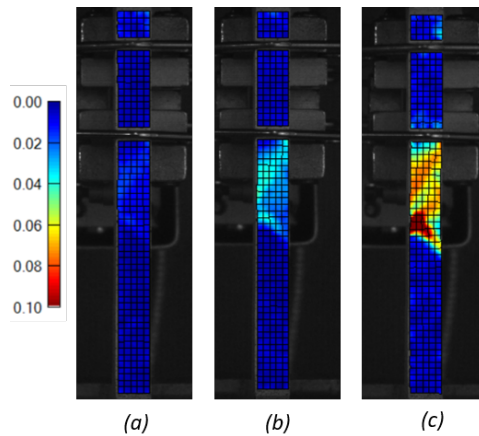


Figure 4.16: Evolution of the strain localization during tensile testing of specimen 2.

Specimen 4

For specimen 4, similar observations as for specimen 2 were made, as shown in Figure 4.17. A root crack starts to develop along the Al-Fe interface, which leads to the final fracture. Figure 4.18 shows the plastic strain evolution during tensile testing extracted from the eCorr analysis. In contrast to specimen 2, it can be seen that the strains start to concentrate in the root between the Al and Fe at an earlier stage, and only small portions of the strains are localized in the HAZ on the aluminium side. Also, in this case, the final fracture occurs along the Al-Fe interface. However, it was noted that this specimen was tested with the steel side

up (and not the aluminium as for the other specimens) which may have impacted the results.

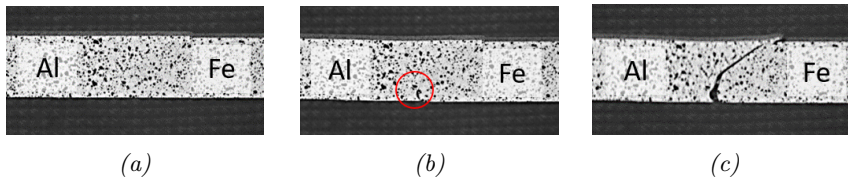


Figure 4.17: Fracture propagation of specimen 4 at different stages during tensile testing; (a) before loading, (b) at the point of crack initiation and (c) final fracture.

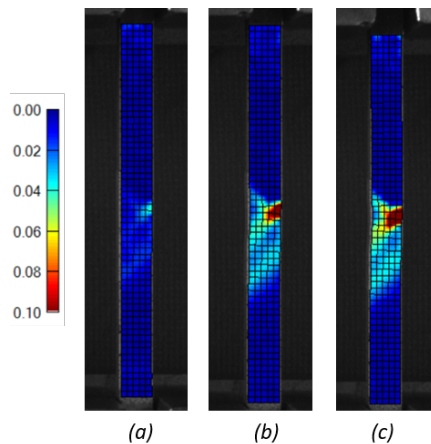


Figure 4.18: Evolution of the strain localization during tensile testing of specimen 4.

Specimen 8

Figure 4.19 shows pictures of tensile specimen 8, having the original shape, at different stages during testing; a) initial unloaded stage, b) at crack initiation and c) the stage of final fracture. In contrast to specimen 2 and 4, it was observed that crack initiation starts at two positions, at the crown and root, respectively, as shown in Figure 4.19b. Both cracks are located close to the Al-Fe interface.

Figure 4.20 shows the strain localization in specimen 8 at different loading stages. As can be seen from Figure 4.20a, at an early stage during testing, the strains start to concentrate both in the HAZ on the aluminium side and the root region between the Al and Fe. The strains continue to develop, and relatively large strains are observed in both the HAZ and root region right before failure, as seen in Figure 4.20c. This highlights the "competition" between the two weakest parts of the

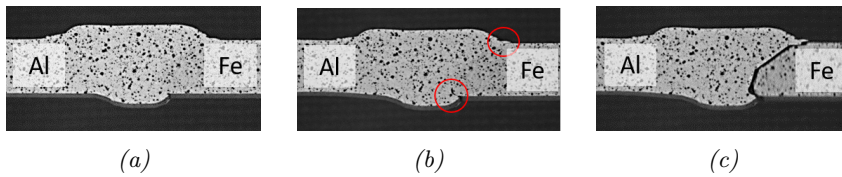


Figure 4.19: Fracture propagation of specimen 8 at different stages during tensile testing; (a) before loading, (b) at the point of crack initiation and (c) final fracture.

weld. Still, the final fracture occurs along the Al-Fe interface, as previously shown in Figure 4.19c. From these pictures, it can be seen that the crack observed in the crown region has little impact on the overall strain concentration, compared to that of the root crack. The indications are that without the root problem, fracture will occur in the HAZ on the aluminium side.

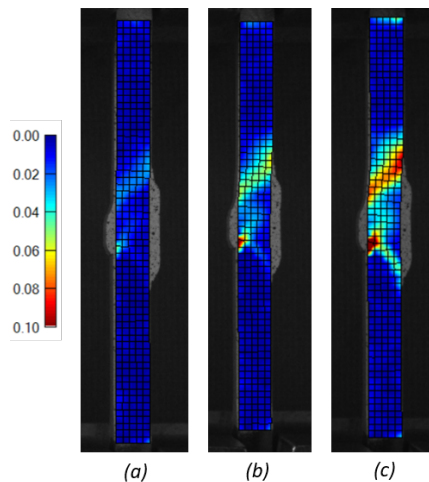


Figure 4.20: Evolution of the strain localization during tensile testing of specimen 8.

4.5 Fractography of tensile specimens

In the following, the main results from the fractographic examination of selected tensile specimens will be presented. All the fractured tensile specimens showed the same characteristic features at the fracture surface, having clearly visible parts of aluminium stuck on the lower part of the steel side, close to the weld root, as

highlighted in Figure 4.21. Below, a more detailed examination of the steel side will be given by the use of SEM and BSE.

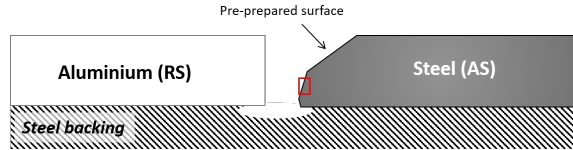


Figure 4.21: Schematic illustration of the position where a significant layer of aluminium was detected on the steel fracture surface.

Figure 4.22 shows SEM micrographs of the steel fracture surface of specimen 4 and specimen 8 at low magnification (25x). In these overview micrographs, it is observed a clear distinction between the upper and lower part of the fracture surface. In the lower part, it is evident that aluminium is stuck on the steel surface, having a fairly rough fracture surface. In addition, a pattern caused by the rotating motion of the extrusion pin can be seen. At the upper part, a cleaner fracture surface is observed with no signs of aluminium at this magnification.

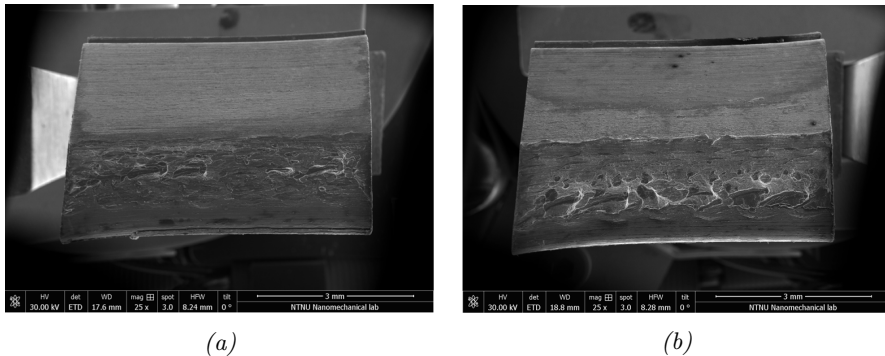


Figure 4.22: SEM overview micrographs at low magnification (25x) showing the steel fracture surfaces of specimen (a) 4 and (b) 8.

Close-ups at higher magnification (5000x) of the fracture surface at different locations of specimen 4 are shown in Figure 4.23. In Figure 4.23a, large dimples with smaller, more shallow, dimples in between, being characteristic for a ductile type of fracture, are observed. Moving on to Figure 4.23b, small shallow dimples are observed, having regions with relatively smooth fracture surfaces in between. The latter regions may indicate regions where the steel surface is visible, and hence, that insufficient bonding between the two materials has occurred. Additional SEM micrographs can be found in Figure F.1 in Appendix F.

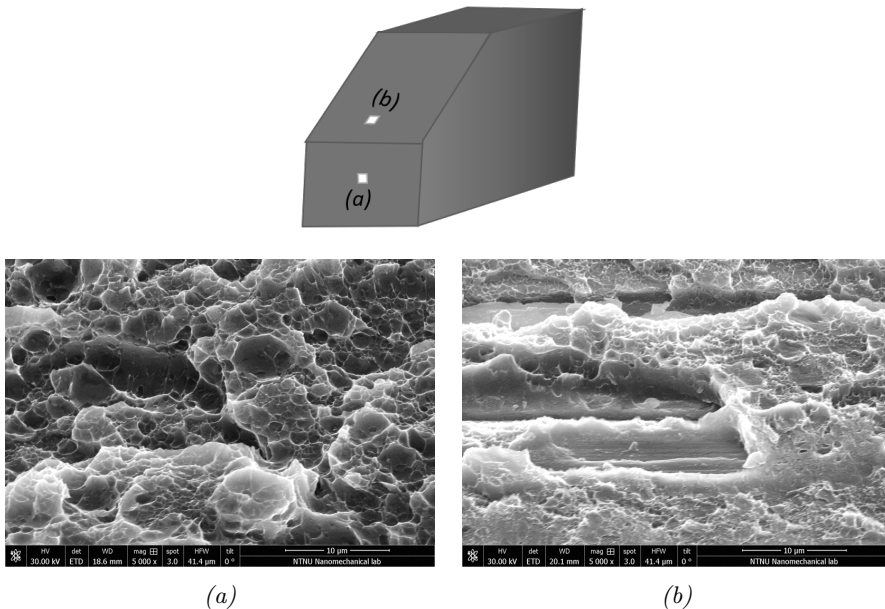


Figure 4.23: SEM micrographs showing close-ups at high magnification (5000x) of the (a) lower and (b) upper part of the steel fracture surface of specimen 4.

Figure 4.24a shows a low magnification micrograph (100x) of the central region in the lower part of specimen 2, where larger portions of aluminium (dark parts) are stuck to the steel (bright parts). As can be seen from the figure, there is almost no sign of aluminium close to the root region, whereas about 0.5 mm higher up from the root, large amount of aluminium can be seen with only small areas of steel visible in between. This is consistent with the observations of a root crack forming in the lower region of the joint close to the Al-Fe interface.

Moving on to Figure 4.24b, showing the transition in the machined slope on the steel side of the weld groove, it is observed that fractions of aluminium are attached to the steel. The amount, however, is significantly smaller compared to Figure 4.24a. This is a remarkable observation that has not been detected before and indicates that the amount of bonding in this area is larger than first assumed. Hence, something that may have a significant impact on the joint strength.

Figure 4.25 shows high magnification micrographs (2000x) of the same regions as previously shown in Figure 4.24. From Figure 4.25a, it can be seen that small chunk's of steel are trapped inside the aluminium. These steel fragments may indicate that the pin has been in contact with the steel during welding and is corresponding well with the previous observations of steel fragments in the EZ, see

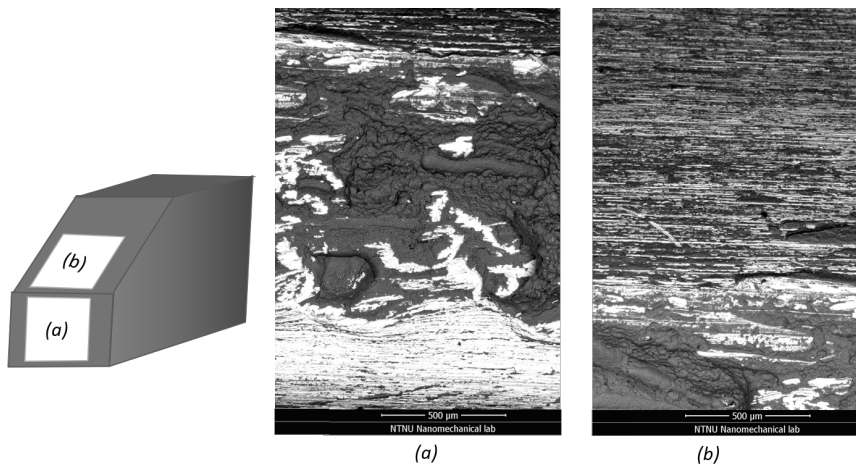


Figure 4.24: BSE micrographs at low magnification (100x) showing the (a) lower and (b) upper part of the steel fracture surface of specimen 2.

Figure 4.6b, from the microscopic examination. Figure 4.25b shows a close-up of the upper half of the steel side groove. From this picture, it is evident that there are aluminium attached to the steel, and that the steel has a wavy surface. However, the amount of aluminium is significantly smaller compared to the lower part of the joint. Additional EDS images can be found in Figure G.1 in Appendix G.

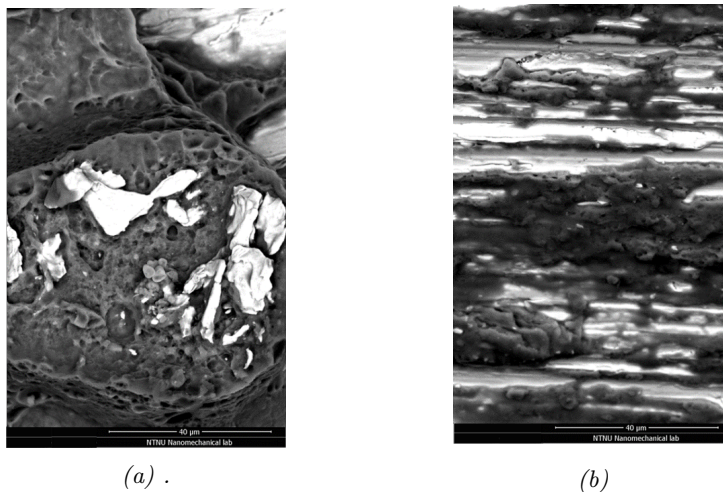


Figure 4.25: BSE micrographs at high magnification (2000x) showing the (a) lower and (b) upper part of the steel fracture surface of specimen 2.

5 Numerical simulation

5.1 Introduction to the finite element method (FEM)

The finite element method (FEM) is a numerical method that is used to predict and solve problems related to engineering and mathematics, as for instance, to simulate the behavior of complex engineering systems. The basics behind the FE analysis is that the system is decomposed into a finite number of sub-domains or elements, known as discretization. This reduces the problem into a finite number of unknowns, where solutions can be obtained for each of these smaller domains. The solutions can then be combined to represent the global solution of the entire system. The elements in the FE model are built up by nodal points, or nodes, which defines the element geometry, and through their degree of freedom, the coupling to the neighboring elements. The elements then form the mesh of the structure, and the smaller the mesh or the element size, the more accurate is the analysis. However, finer mesh also contributes to higher computational time [15, 62].

Several different element types exists, and some of the most commonly used during stress analyses are shown in Figure 5.1. The degrees of freedom, like displacement and rotation, are calculated at the nodes of the elements, while at other positions the displacements are obtained by interpolation from the nodal displacement to the specific location. The elements may have different number of nodes, which determines the interpolation order [15, 62, 63].

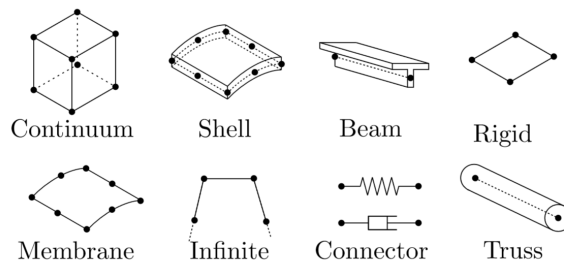


Figure 5.1: Some element families commonly used in Abaqus. Copied from [15].

In this report, the FE software used for analysis is the Abaqus finite element system ABAQUS/CAE (6.17). This software includes both a general-purpose FE program and an explicit dynamic FE program. In Abaqus, the behavior of the material is described by integrating different numerical models. The material response is then evaluated at each integration point in all the elements, either using full or reduced integration for the continuum elements [15].

5.2 Set-up for finite element (FE) model of tensile testing

5.2.1 Part creation and material properties

The first step in an FE analysis is to create a part, as shown in Figure 5.2. Previously it has been observed that the properties of the dissimilar Al-Fe HYB joint changes across the joint. Thus, in order to obtain a realistic model, the extension of the different weld zones is needed, together with their corresponding material properties.

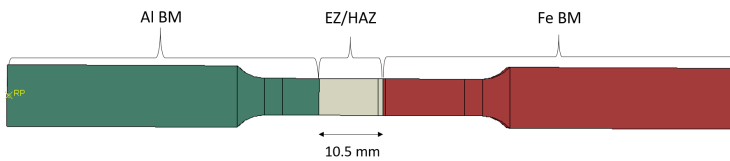


Figure 5.2: Illustration of the materials assigned to the different regions of the finite element (FE) model. Note that the width of the HAZ/EZ is set to 10.5 mm.

From the hardness measurements in Figure 3.8a in Section 3.6, four distinct zones are observed. That is the unaffected aluminium base material, the HAZ, the EZ, and the unaffected steel base material. However, it is noted that the lowest hardness in the HAZ and that of the EZ is relatively similar and these zones will, therefore, be treated as one material in the following. In addition, since the hardness of the HAZ gradually increases from the lowest point until the Al BM hardness is reached, the total width of the reduced strength zone in the joint is set to 10.5 mm. This value is based on calculations of the reduced cross-section area of the joint, which is a model for calculating the joint design stress [64], and obtained from Lise Sandnes (Personal Communication, 2019).

The second step in the FE analysis is the implementation of relevant material data. Figure 5.2 also shows the materials assigned to the different regions of the FE model. Material data used for AA6082-T6 base material was extracted from the master thesis of Lise Sandnes [50]. She has done material testing on the exact same Al BM as used in the present report. Relevant material data are summarized in Table 8. For the Poisson ratio and E-module, the generally accepted values of 0.33 and 70 GPa was used. For the S355 steel, material data was extracted from the literature (see Table 8).

In Abaqus, true stress-strain data is needed. For the aluminium base material, the data could be directly converted because raw data from the tensile testing was available. However, for the steel base material, the original data was not available,

Table 8: Engineering material data used for the aluminium and steel base materials in the finite element (FE) model.

Material	σ_{YS} [MPa]	σ_{UTS} [MPa]	ν	E [GPa]	Ref.
AA6082-T6	255	306	0.33	70	[50]
S355	355	490	0.3	210	[65]

and the data had to be rendered by the use of Hollomon's equation [66], shown in Equation 5.1. Here σ_T is the total true stress, ϵ_T is the total true strain, n is the strain-hardening exponent and K is the strength coefficient. K and n were calculated to be 900 MPa and 0.15, respectively.

$$\sigma_T = K\epsilon_T^n \quad (5.1)$$

The properties of the HAZ/EZ were obtained from the DIC analysis of the tensile specimens, by the use of virtual extensometers sampling the HAZ properties. The true stress-strain curves were obtained directly from the DIC analysis. Because the FE model is made without a weld reinforcement, material data from specimen 2 was selected for further use. The values for the E-module, yield strength and UTS can be found in Table 13 and Table 14 in Appendix D. Figure 5.3 shows a comparison of the true stress-true plastic strain curves for all the materials used in the FE model (i.e., Al BM, Fe BM, and HAZ/EZ). This data was used to account for the post-yield behavior of the materials.

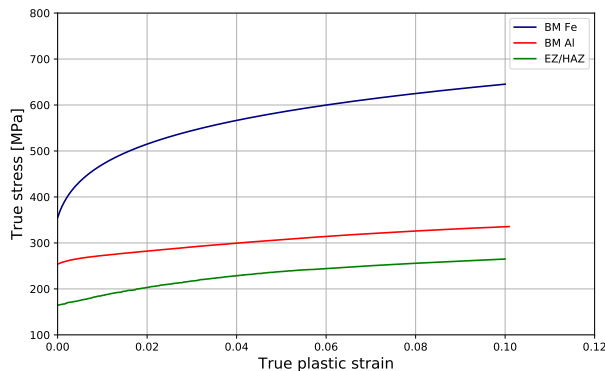


Figure 5.3: Stress-strain curves showing the true stress and true plastic strain for the different zones in the Al-Fe HYB joint, used as input for the material plasticity in the finite element (FE) model.

5.2.2 Damage initiation and evolution

In numerical simulations, like FE, the materials are assumed to be homogeneous without any defects or weak parts. However, weak parts of a structure are often the origin of crack initiation and final fracture. Abaqus offers several different models to account for these defects by making it possible to define the point where failure initiates and the following damage evolution. As observed from the DIC analysis and the microscopic investigation, a root crack developed close to the Al-Fe bond line, which led to the final fracture during tensile testing. To simulate the effect a root crack has on the mechanical integrity of the dissimilar HYB joint, the extended finite element method (XFEM) was utilized.

XFEM is a method to implement the onset and propagation of cracks in quasi-static problems. This method is an extension of the conventional FE method, which is based on the concept of partition of unity. This concept allows the presence of a discontinuity in an element by adding displacement functions to the degrees of freedom, which then accounts for jumps in displacements across the discontinuity. The XFEM method overcomes some of the main drawbacks with the conventional FE method, including the need for complex meshing of the fracture surface, because the fracture surface is independent of the mesh configuration. This makes it possible to implement the crack propagation along an arbitrary path without the need to remesh the model. XFEM allows you to either define the initial location and size of the crack or let Abaqus determine the location of the crack during the analysis based on pre-defined values for the damage initiation [15].

To investigate the effect of a root crack on the dissimilar Al-Fe HYB joint this discontinuity was included in the FE simulation. The crack was modeled separately as a 3D deformable shell and assembled with the model of the tensile specimen. This method is preferred as it takes advantage of the mesh-independent representation of the crack, which is preferred in XFEM. The initial length of the crack was varied between 0.03 and 1.2 mm. As observed in the SEM and EBS images, relatively large amounts of aluminium were present on the steel fracture surface. This implies that the fracture did not go entirely through the Al-Fe bond line, as first indicated from the DIC analysis, but rather in the FM close to the Al-Fe interface. An advantage with XFEM compared to the conventional FE method is that the fracture does not need to be aligned with the edge of an element. It is preferred that the crack is inside an element, which makes it possible to position the crack close to the interface. The crack was positioned 0.6 mm away from the Al-Fe bond line, as shown in Figure 5.4. This was the smallest distance found which prohibited the crack from propagating into the steel during the simulation. A description of the crack positioning study can be found in Appendix H.

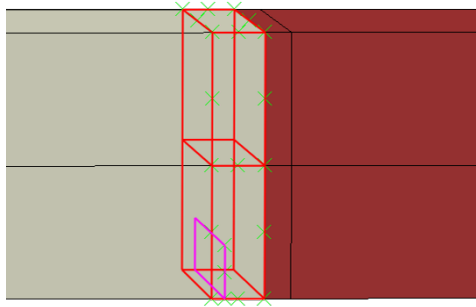


Figure 5.4: Illustration of the crack positioning and crack domain in the finite element (FE) model of the Al-Fe HYB joint.

In addition to the positioning of the initial crack, the crack domain needs to be specified. The crack domain defines the enrichment region in the model where the existing crack is allowed to propagate or the area in which a crack might be initiated. In Figure 5.4, the red part indicates the crack domain and was set to be 0.8 mm starting from the Al-Fe interface. The crack domain should be limited because the addition of extra internal nodes will strongly affect the computational time of the analysis. The width of the crack domain was also investigated during the crack positioning study and can be found in Appendix H.

In Abaqus, two different approaches can be used for studying the crack initiation and propagation using XFEM. The cohesive zone model (XFEM based cohesive behavior) and the virtual crack closure technique (XFEM based LFM approach). In this study, the cohesive segment approach was utilized, which is based on traction-separation cohesive behavior [15]. The damage properties are in this model specified as a part of the material properties, and both a damage initiation and evolution criteria are included.

The damage initiation criterion specifies when the crack will start to propagate, and when the degradation of the cohesive response will begin. The degradation begins when the stresses or strains satisfy a given criterion. The maximum principal stress criterion was chosen for this study ('Maxps Damage' in Abaqus) and can be represented by Equation 5.2. Here σ_{max}^0 is the maximum principal stress allowed, and the $\langle \rangle$ represents the Macaulay brackets. Macaulay brackets are a notation that indicates that $\langle \sigma_{max} \rangle = 0$ if $\sigma_{max} < 0$ and $\langle \sigma_{max} \rangle = \sigma_{max}$ if $\sigma_{max} \geq 0$. The crack length of the existing crack is extended when the fracture criterion reaches the critical value ($f = 1$) [15].

$$f = \left\{ \frac{\langle \sigma_{max} \rangle}{\sigma_{max}^0} \right\} \quad (5.2)$$

The true ultimate tensile strength (233 MPa) for the HAZ/EZ was used as the limiting maximum principal stress. When the criterion is satisfied, the crack will propagate orthogonal to the maximum principal stress direction, and degradation of the cohesive stiffness will occur. The damage evolution criterion defines how the degradation of the stiffness will happen. Two components describe the evolution of the damage. The first is the fracture energy or the energy dissipated due to failure, which equals the area under the traction-separation curve, see Figure 5.5 [15]. This fracture energy was estimated using the relationship between J and CTOD (crack tip opening displacement), $J = \sigma_{YS} \delta$ [67]. The value was calculated to be 103.3 N/mm (L. Sandnes, Personal communication, 2019).

The second component is to specify the nature of the evolution of the damage variable, D . D represents the average damage at the intersection between the surfaces of the crack and the edges of the cracking element. This variable has an initial value of 0 (no damage) and continues to increase towards 1 (complete failure) as the load is increased during the simulation. Equation 5.3 shows how the normal and shear stress components are affected by the damage. In the equation T_n , T_s and T_t are the contact stress components predicted by the elastic traction-separation behaviour for the current separations without any damage [15].

$$t_n = \begin{cases} (1 - D)T_n, & \text{if } T_n \geq 0. \\ T_n, & \text{otherwise.} \end{cases} \quad (5.3a)$$

$$t_s = (1 - D)T_s \quad (5.3b)$$

$$t_t = (1 - D)T_t \quad (5.3c)$$

D can either be defined by a linear or exponential softening behavior. The linear damage evolution was chosen and is shown in Figure 5.5. Due to both the softening and stiffness degradation, there can often be problems with the convergence in Abaqus. To overcome some of these difficulties, viscous regularization was used. The viscosity coefficient was set to 0.0001. Such a small value will help convergence while having minimal effect on the final results.

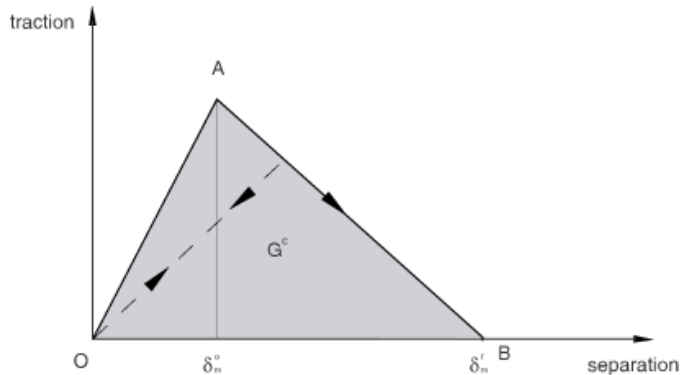


Figure 5.5: Illustration of the linear damage evolution criterion based on fracture energy. Copied from [15].

5.2.3 Boundary conditions, loads and constraints

During all the simulations, the same boundary conditions, constraints, and loads were used. The effect of the clamping of the tensile specimens during tensile testing was applied to the model in the form of boundary conditions. At the lower part of the model (steel side), a mechanical Encastre boundary condition was chosen. This prohibits translation in all directions and rotation about all axes ($U1 = U2 = U3 = UR1 = UR2 = R3 = 0$), see Figure 5.6a. To the top part of the model (aluminium side), the load is moving the specimens in the y-direction, but the clamping constrains the specimen from rotating or translate in all other directions. A mechanical displacement/rotation boundary condition was therefore utilized, which only allow movement along the loading direction ($U1 = U3 = UR1 = UR2 = UR3 = 0$), as shown in Figure 5.6b.

To apply the right load, a coupling constraint was added to the aluminium side of the joint. A reference point was made at the middle of the top surface, and set as the coupling master control point. The two surfaces that were clamped during the experimental testing were set as slave surfaces, as illustrated in 5.6c. This was done to evenly distribute the load over the surfaces and make the simulation as similar to the experimental test set-up as possible. The load was applied to the reference point as a 2 mm displacement in the y-direction.

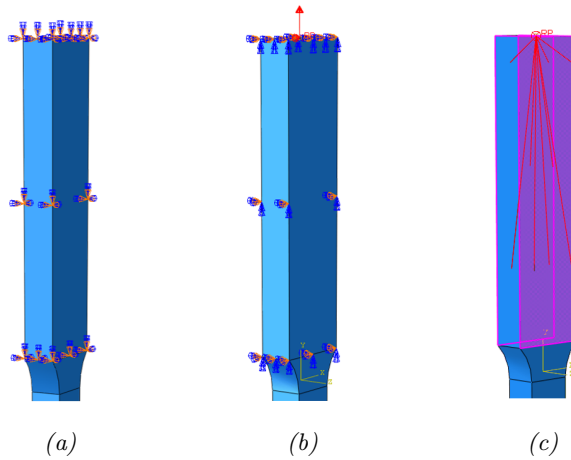


Figure 5.6: To simulate the experimental set-up of the tensile testing (a) boundary conditions, (b) load and (c) a coupling constraint were applied to the finite element (FE) model.

5.2.4 Partitioning

Partitioning of the model into smaller parts is essential for many reasons; correct application of the mesh, be able to assign the crack domain, define different material properties and positioning of the extensometer. The faces of the three-dimensional model were first partitioned by using the sketch method. Secondly, the face partitions were used to partition the cell by utilizing the extrude/sweep edge method. An area of 10.5 mm was partitioned to represent the HAZ/EZ. Another partitioning of 30 mm along the thickness of the model, as shown in Figure 5.7, represents the extensometer. This partitioning made it possible to obtain values for the displacement from the right position after the simulation. The extensometer was positioned similarly as the virtual extensometers applied to the DIC analysis, see Figure 3.7 in Section 3.6. Additional partitions made to obtain a consistent mesh can be seen in the figure below.

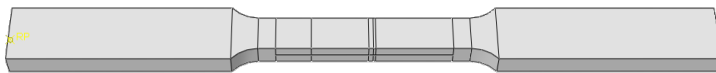


Figure 5.7: Illustration of the partitioning of the finite element (FE) model.

From Figure 5.7, it can be seen that a partitioning was made 0.8 mm from the Al-Fe interface. This partition line, in addition to the Al-Fe interface, were chosen to

represent the crack domain. In order to position the initial crack, a temporary face partition was made, and the nodes from the partition line were used to translate the crack to its respective position. This temporary line was not a part of the final simulation. After much trial and error, it was also needed to partition a line from the bottom of the model with the same length as the chosen initial crack. This is because the crack always propagates through one element at the time to avoid the need to model the stress singularity. If the mesh then is bigger than the crack length, the crack length will automatically be altered to the same length as the mesh.

5.2.5 Mesh

Two different 3D elements can be used for XFEM simulations. These are the tetrahedral and hexahedral elements. The hexahedral elements are only available as linear order approximations, while the tetrahedral elements also are available as quadratic. Linear structural hexahedral elements were chosen for the simulations and are denoted C3D8R. Different sections of the model were meshed with varying element size. As observed from the results showing the different stress-strain curves of the weld (Figure 4.14 in Section 4.3.2) and the DIC analysis, only the aluminium deforms plastically, and the significant deformations are found within the HAZ/EZ. It was, therefore, assumed that only the part of the model representing the HAZ/EZ would experience large strains and deformations during the simulation.

This assumption was verified by studying the local strains in the model when the model was set-up for simulation. The verification was also used to see if the constraints and boundary conditions behaved as intended. The load was changed to 3 mm as a safety factor during the verification, and a mesh size of 1 mm was applied. One simulation was done with an initial crack of the same length as the mesh size, and another simulation was executed without any pre-existing crack. Figure 5.8 shows the two verification studies of the model.

As shown in Figure 5.8a, when no crack is present, the deformations and strains concentrate in the HAZ/EZ, where necking occurs. No changes can be seen elsewhere in the model. The same is observed from the results from the simulation with an initial crack, Figure 5.8b. Most of the strain concentrates around the crack tip, but also in the HAZ/EZ. From both studies, it is evident that no strains or displacements of importance were noticed in either the aluminium or steel BM. A finer mesh was therefore only applied to the regions close to the crack domain and the HAZ/EZ, to reduce computational time. The function "local seeds" was used to assign more elements in these areas.

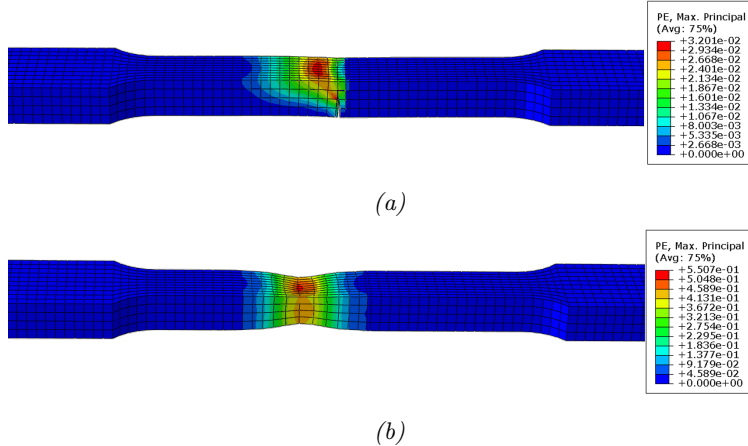


Figure 5.8: Principal strains in the finite element (FE) model used for verification of mesh size (a) with and (b) without an initial crack.

When the mesh is refined in a FEM simulation, the results will converge towards more accurate results. Therefore, a mesh sensitivity analysis was performed to find the optimal number of elements in the thickness direction. This was done regarding the plasticity in the model because when the crack is introduced, the model gets more complex and problems regarding convergence appear. Therefore, a separate analysis was needed regarding the positioning of the crack and the mesh size in the crack domain. Figure 5.9 shows the maximum force in the simulation as a function of the number of elements in the thickness direction. It can be seen from the figure that the maximum force starts to converge when the number of elements equals 8. A further refinement of the mesh would then not have a significant effect on the resulting output data regarding plasticity. However, 10 elements were chosen as this was found to be the smallest element size where the crack propagation converged, as explained in the discussion below, and is within the limit for convergence regarding plasticity.

It is wanted during an XFEM simulation to have quadratic mesh in the crack domain. Therefore, were also a mesh size of 0.4 mm chosen for the rest of the model close to the crack and in the area representing the EZ/HAZ. The remaining parts of the model were selected to have a mesh size of 1 mm, to reduce the computational time of the simulation. The final model then consisted of a solid mesh of 24 288 linear brick elements and is shown in Figure 5.10.

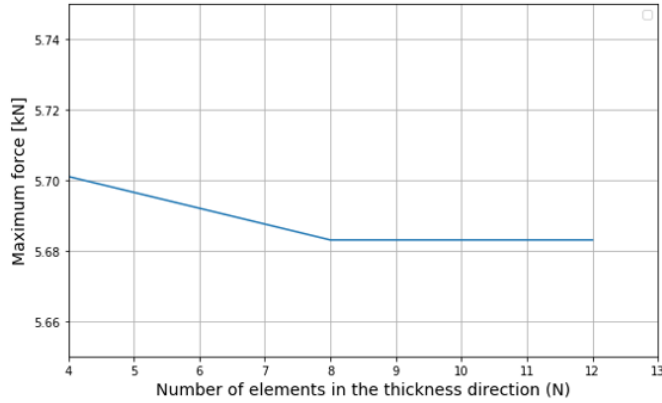
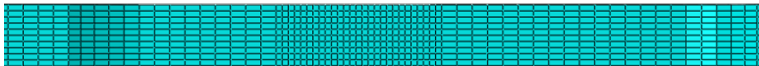
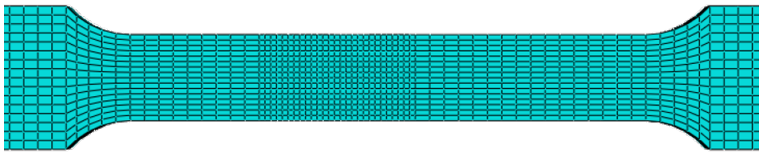


Figure 5.9: Mesh sensitivity analysis of finite element (FE) model.



(a)



(b)

Figure 5.10: Mesh of the finite element (FE) model in a) the thickness and b) the length direction.

5.3 Discussion of simulation approach

Several factors made the simulation of the dissimilar Al-Fe HYB joint challenging. Mainly because the model consists of three different elastic-plastic bulk materials and the fact that mechanical problems like fracture are very complex. In elastic-plastic cases, there are two types of non-linearity that occur. The geometric non-linearity caused by large deformations, and the non-linearity in the material due to the plasticity. Fracture also makes the structure respond non-linear and non-smooth, something that strongly affects the convergence of the solution. As the

fracture is considered as ductile in the analysis, the non-linear theory of fracture mechanics need to be considered. As stated by Kumar et al. [68], most of the use of XFEM focuses mainly on the linear elastic behavior of the material and involves only small deformations. Little information was, therefore, possible to obtain about elastic-plastic simulations with XFEM.

It was desired to simulate the competition between failure occurring due to necking in the weakest part of the weld, EZ/HAZ, and failure due to an initial crack close to the Al-Fe bond line. Due to the high elasticity of the aluminium EZ/HAZ, a ductile damage criterion should be used to predict the onset of necking and final fracture in this area. This criterion with element deletion can only be simulated in a dynamic explicit analysis. However, XFEM, which is a quasi-static analysis, can only be simulated as dynamic implicit or static general. This makes it impossible to simulate the two different fracture criteria in the same simulation. To overcome this limitation, a co-simulation was performed. The model was split into two parts, where one was simulated explicit and one implicit. This resulted in large deformations at the interface between the two models, and no valid results. It was, therefore, decided to only focus on fracture caused by an initial crack. A fine and quadratic mesh is wanted close to the propagating crack. In addition, as mentioned, is a limitation with the XFEM approach that the crack always propagates one element length at the time. To simulate small cracks, the element size needs to be similarly small, which resulted in a study on mesh size in the crack domain. The increased number of elements led to long computational time and not adequate computer capacity. A new strategy was tested, which involved splitting the model into three parts and mesh them separately, followed by connecting them by the use of tie constraints. The results showed inconsistent strain across the element boundaries between the tied regions, and no convergence of the simulation.

Many different element sizes were investigated, but a common problem with small elements was that the crack would not propagate across element boundaries in the length direction and convergence was not achieved. Different positions of the crack were also tried for the different element sizes. The smallest element size in the length direction, which gave consistent results was 0.4 mm. Two alternatives could then be considered to simulate cracks smaller than 0.4 mm. Either have different mesh sizes in the thickness and length direction, which would result in a very un-quadratic mesh configuration, or partition a line from the bottom of the model with the same length as the crack. The last alternative was chosen as already explained, resulting in only the bottom mesh of the model consisting of a not quadratic mesh.

Therefore, the final simulation set-up is a result of the testing of several different approaches. This is because a similar simulation has not been reported earlier.

Due to the complexity of the model, further work should be done based on the now existing model to make it even more representative for the dissimilar Al-Fe HYB weld. An in-depth validation should also be executed.

6 Discussion

6.1 Introduction

In the following, attempts will be made to rationalize the main findings from the experimental work. The discussion is divided into four main parts. First, a comparison of the mechanical properties of different FS and HYB weldments will be given. Secondly, attempts will be made to explain the relatively high strength obtained in the HYB joint by means of the intermetallic layer and the Al-Fe interface configuration. Then, the effect of the root crack problem will be analysed by the use of the finite element (FE) model. Finally, some concluding remarks regarding the evolution and current status of the HYB process for joining aluminium and steel will be presented.

6.2 Comparison of the mechanical properties of dissimilar Al-Fe friction stir (FS) and HYB weldments

In the following, the joint efficiency (i.e., tensile strength to base material ratio) being achieved for different friction stir (FS) butt welds, using different base material combinations, will be compared to that obtained in the HYB joint. Note that, all data for the FS welds are extracted from the literature. Due to the difference in base material combinations used in these joints, the materials microstructure and crystallographic texture are not further considered.

Figure 6.1 shows a comparison of the joint efficiency of different types of dissimilar Al-Fe weldments produced using FSW and the HYB process. As can be seen from the bar graph, the HYB joint reaches a relatively high joint efficiency of 75%, despite the presence of the root crack. In fact, this value is higher than what can be seen for the two FS welds produced using the 6xxx-series aluminium alloys. Still, in this comparison, the highest joint efficiency reported is found for the FS weld produced using aluminium alloy 5052 and HSLA steel as base materials, and reaches a joint efficiency of 95%. To the author's knowledge, this is the best practice within dissimilar aluminium-steel welding and the result of years of research and optimization of the process. Taking this into consideration, the HYB technology shows promising results for further use of dissimilar welding when the process has been further optimized.

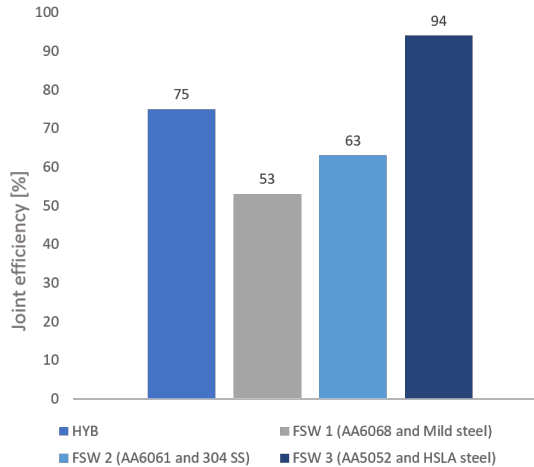


Figure 6.1: Comparison of the joint efficiency in different friction stir (FS) welds relative to the one obtained for the HYB process.

6.3 Intermetallic layer thickness and Al-Fe interface configuration

6.3.1 Effect of IMP layer thickness

In dissimilar weldments of aluminium and steel, the governing bonding mechanism is the formation of intermetallic phases (IMP) along the Al-Fe interface. Both the composition and thickness of these phases will strongly affect the overall joint strength under otherwise sufficient conditions [9, 32]. In Al-Fe welding, the IMPs that form along the interface between the two materials are characterized by their high hardness and brittle properties. Therefore, it is essential to keep the IMP layer thickness below a critical value to avoid cracks from forming within the layer. Previously, it has been proposed that there exists an ideal thickness of the intermetallic layer of about 1 μm for dissimilar Al-Fe FS welds [47, 69]. This is illustrated in Figure 6.2. As can be seen from the figure, the heat input during processing (here represented by the tool rotation speed) will strongly affect the formation of the intermetallic layer thickness and, thus affect the joint strength. Moreover, it can be seen that when the intermetallic layer is too small (less than 1 μm), there will be a reduction in the joint strength.

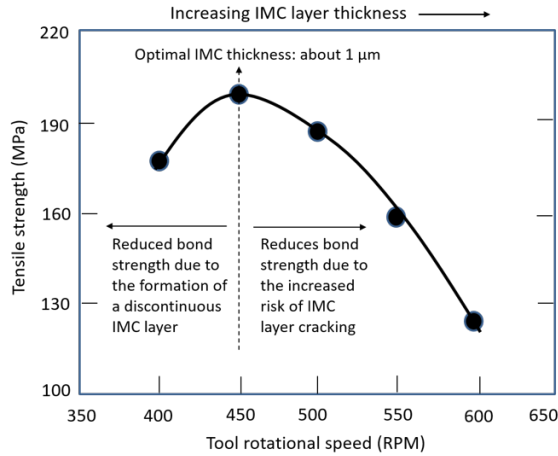


Figure 6.2: Graphical illustration of the intermetallic layer thickness formation relative to the heat input during joining (based on the tool rotation speed) and the corresponding tensile strength of the joint [47].

Figure 6.3 shows a comparison of the intermetallic layer thickness in three different Al-Fe joints produced by CMT, FSW, and HYB, respectively. As can be seen from Figure 6.3a, the thickest intermetallic layer is found for the CMT specimen having a thickness of about $3\ \mu\text{m}$. This joint is welded in a lap configuration and reaches a joint efficiency of approximately 53%. The FS weld in Figure 6.3b have an IMP layer thickness of about $1\ \mu\text{m}$ and a corresponding joint efficiency of about 95%. However, for the HYB joint shown in Figure 6.3c, the IMP layer cannot be seen even at a magnification of 10 000x. Thus, the layer must be less than $0.1\ \mu\text{m}$, which is typically the lower limit for what can be seen in standard SEM analysis. In fact, work done by the PhD candidate Tina Bergh [70], using a high-resolution transmission electron microscope (TEM), has proven that the intermetallic layer in the HYB joint is between 20 and 30 nm, as shown in Figure 6.4. The HYB joint reaches a joint efficiency of 75%, which is surprisingly based on the observation of an extremely thin intermetallic layer being present on the Al-Fe interface. These findings strongly challenge the proposed existents of an optimal IMP layer thickness in dissimilar Al-Fe weldments. The reason for this can not yet be explained but may indicate that the composition of the Al-Fe IMCs plays a significant role when it comes to the joint strength. Further research is therefore needed to thoroughly understand the effect of the intermetallic layer on the overall bond strength in dissimilar Al-Fe welds.

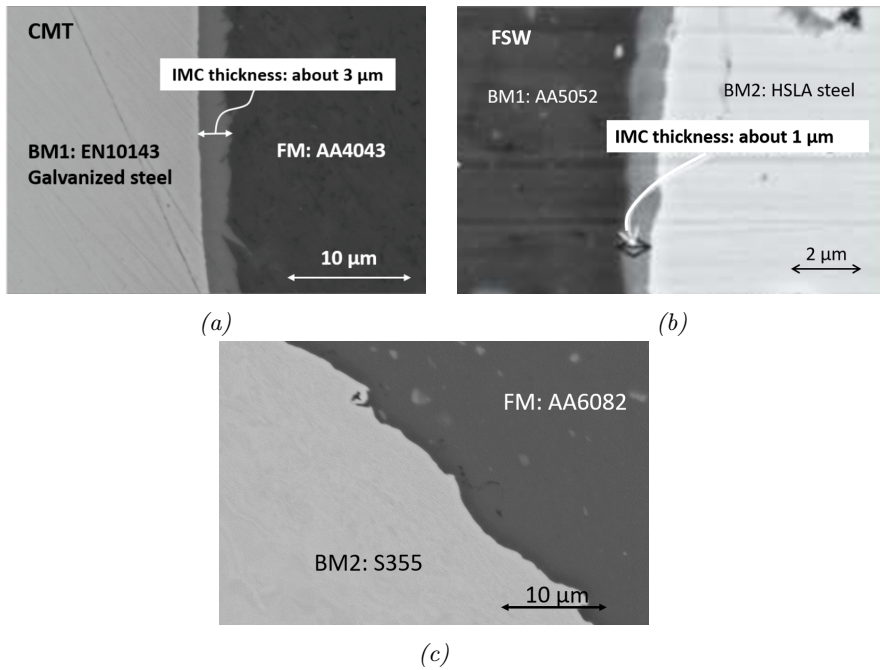


Figure 6.3: Low magnification micrographs showing the Al-Fe interface in different types of weldments. a) CMT [3], b) FSW [47] and c) HYB.

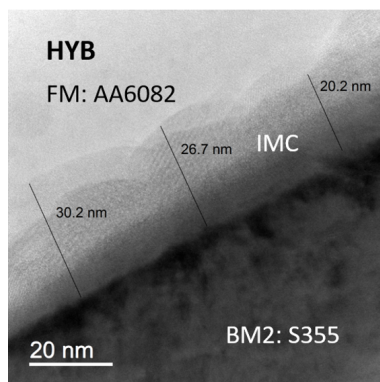


Figure 6.4: TEM micrograph showing the HYB joint intermetallic layer thickness. Copied from [70].

6.3.2 Effect of Al-Fe interface configuration

In the HYB welding trial, the steel side was machined to form a Y-groove, as shown in Figure 6.5. Due to this configuration of the weld groove on the steel side, together with the pin being formed as a conical “Archimedes”-screw, the velocity of the material flow, and thus the pressure, in the upper part (close to the weld crown) would be lower compared to the bottom part of the weld groove. This may in turn result in more ideal conditions for IMP formation and result in better bonding closer to the root, as previously observed from the fractographic examination.

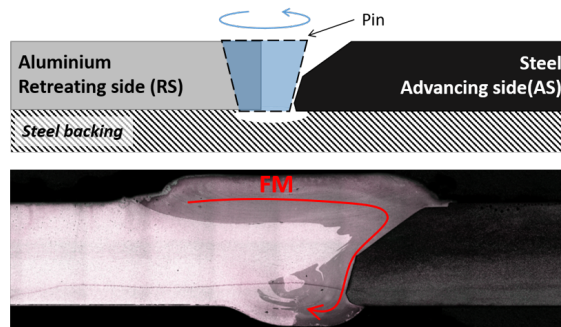


Figure 6.5: Illustration of the weld groove configuration and material flow in the dissimilar Al-Fe HYB joint.

During the microscopic analysis of the HYB joint Al-Fe interface, it was observed that the steel side appears rougher in the lower region (close to the weld root) where good bonding did occur. This compared to the upper region, closer to the weld crown, where the bonding was less apparent. This is mainly believed to be a result of the pre-machining process, or that the pin is slightly touching the lower part of the steel side during the joining operation. This wavy surface in the lower part will inevitably increase the surface area and give a larger effective bonding area. In addition, the surface roughness may give rise to small scale mechanical interlocking, as shown in Figure 6.6. In fact, the effect of mechanical interlocking, together with intermetallic bonding, has proven to have a positive effect on the strength of aluminium-steel welds made by Friction Stir Dovetailing (FSD) [71]. In FSD, mechanical interlocking is formed at the aluminium and steel interface in addition to strengthening by the intermetallic bonding. During the experimental trial, testing was performed both with and without dovetail. This was to compare the effect of mechanical interlocking with that of the metallurgical bonding on the overall bond strength. They concluded that the combination of both dovetail interlocking and metallurgical bonding by IMP formation resulted in a significant increase in strength and elongation compared to when only one of the bonding

mechanism was present. However, the interlocking mechanism used in this research was relatively large scale compared to the observations made in the present report, and the effect of small scale interlocking in the HYB case is yet to be determined.

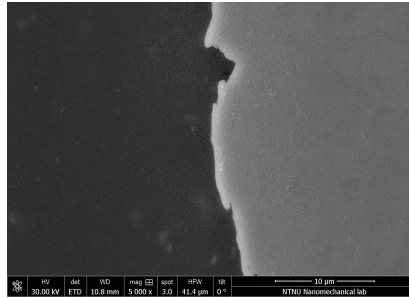


Figure 6.6: SEM micrograph of the rough Al-Fe interface in the lower part of the HYB joint.

Despite the fact that better bonding was observed in the lower region of the HYB joint, traces of aluminium stuck on the steel was also seen in the upper half of the joint, as shown by the BSE fractographs in Figure 4.25 and Figure 4.24 in Section 4.5. As larger areas of steel are visible in this region compared to the bottom part of the weld, it is believed that the bonding here is more discontinuous. This may be caused by the weld groove configuration, which reduces the velocity of the material flow in this region, causing insufficient bonding conditions. Still, this partly bonded area is believed to have a positive contribution to the overall joint strength.

6.4 The significance of a root crack in the Al-Fe HYB joint

6.4.1 Validation of the FE model

Figure 6.7 shows the engineering stress-strain curve obtained from the DIC analysis (black curve) and that from the simulation (dashed line). The DIC curve is obtained from specimen 2, while the simulation curve from a model without implementation of any damage criteria or initial crack. As can be seen from the figure, the FE model gives a fairly good representation of the experimental results, with only small deviations. Therefore, the model is believed to provide an adequate representation of the tensile response of the Al-Fe HYB butt weld. The results also imply that the set-up and input data applied in the simulation are reasonable. This justifies further use of the FE model for investigating the integrity of the dissimilar Al-Fe HYB joint.

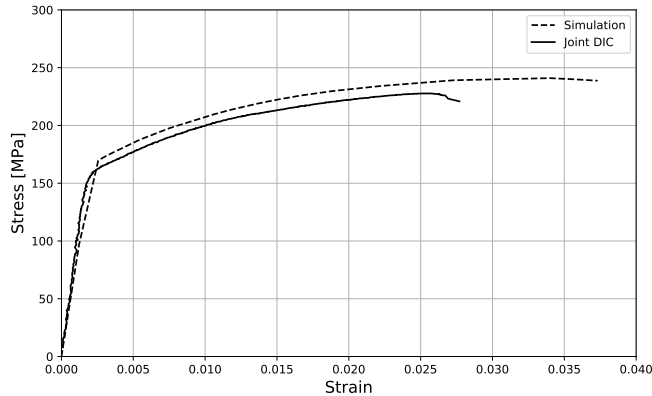


Figure 6.7: Comparison of simulated (dashed line) and measured (solid line) engineering stress strain curves for the Al-Fe HYB joint.

One simplification in the FE model, which may have an impact on the results, is the configuration of the steel side of the weld groove. In the simulation, the steel surface is modeled as a straight surface. Thus, when a crack is present close to the Al-Fe interface, it will experience Mode I loading if no incline is present relative to the loading direction. In reality, due to the slope on the steel side after the machining, the fracture will be a combination of Mode I and Mode II, and therefore mixed mode loading. The effect of this assumption on the results is uncertain. Nevertheless, Tvergaard [72] looked at the effect pure mode I and mode mixity loading had on the crack growth in a homogeneous ductile metal modeled with elastic-plastic behavior, which is comparable to the situation in the HYB case. He noted that when adding a mode II loading to the Mode I case, this contributed to increasing the fracture toughness relative to that for the pure Mode I loading. This can indicate that the results obtained from the FE simulations of the Al-Fe HYB joint are conservative compared to the actual case, further research and development of the FE model is needed to confirm this.

6.4.2 Effect of the root crack size on the joint strength

From the DIC analysis, it was evident that a root crack formed along the Al-Fe interface of the HYB joint. In the following, the FE model will be used to evaluate the mechanical strength of the joint when introducing a crack to the model. The crack length is varied between 0.03 mm and 1.2 mm in order to see the effect of the crack size on the overall properties of the joint.

Note that, the model is simplified by assuming perfect bonding between steel and aluminium and that a root flaw with no bonding is present in the root region. A detailed description of the FE model and materials used was given in Section 5. Figure 6.8 shows a master plot of the force-displacement curves for different simulated crack lengths. The black curve represents the behavior of the joint when no crack is present, whereas the colored curves show the joint behavior when different crack lengths are introduced in the model.

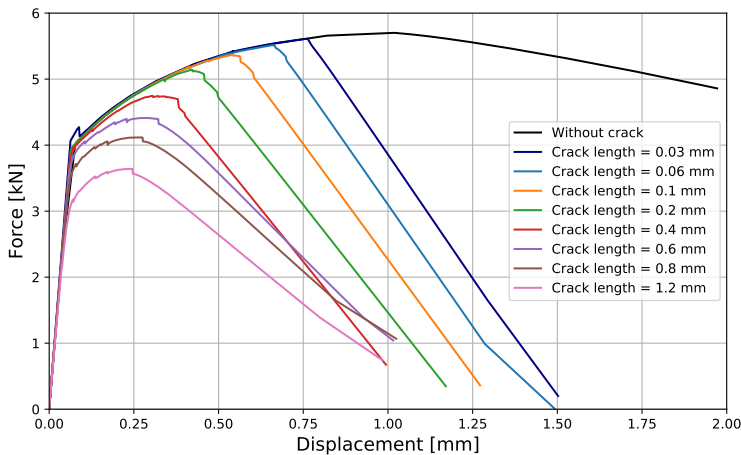


Figure 6.8: Master plot showing the force-displacement behavior of the simulated Al-Fe HYB joint. The black curve represents the behavior of the weld without any root crack, whereas the colored curves show the behavior of the joint when introducing a crack having an initial depth of 0.03 to 1.2 mm.

From this plot, it can be seen that when a crack is introduced to the system, the force-displacement curves are shifted to the left reaching a lower maximum force compared to the model without any crack. Moreover, it can be seen that the mechanical response to the tensile test is gradually decreased with an increase in crack length. In addition, when the pre-crack is larger than 0.4 mm it also compromises the yield strength of the joint which becomes smaller, as well as its elasticity. Thus, if the pre-crack is kept below this limit, only the tensile strength and ductility are compromised, and the force-displacement curve will otherwise follow the behavior of the joint without a pre-crack.

The maximum force, strength reduction, and displacement at failure for the different simulations are summarized in Table 9. When it comes to the mechanical strength of the weld the highest possible load is 5.7 kN, which is equal to a ten-

sile strength of approximately 238 MPa. This is slightly higher than the tensile strength for the flush-machined specimens (i.e., specimen 2 and specimen 4), measured in the experimental trial. Moreover, as can be seen from the table, a small crack length of 0.03 mm reduces the maximum force with 1.6%, while a larger crack of 1.2 mm can reduce the strength as much as 38%. If the initial crack length is kept below 0.1 mm, the strength reduction will be about 6%. From Table 9 it can also be seen that the displacement at failure reduces significantly with an increase in the initial crack length. However, as there does not exist any experimental data for a defect free weld, the amount of reduction is unknown.

Table 9: The resulting maximum force, strength reduction, and displacement at failure for the simulated Al-Fe HYB joint when introducing a crack having an initial depth of 0.003 to 1.2 mm.

Crack length [mm]	Maximum force [kN]	Strength reduction [%]	Displacement at failure [mm]
Without crack	-	5.7	-
0.03	5.61	1.6	0.76
0.06	5.51	3.33	0.66
0.1	5.36	5.96	0.55
0.2	5.14	9.82	0.42
0.4	4.74	16.84	0.33
0.6	4.41	22.63	0.29
0.8	4.06	28.77	0.17
1.2	3.53	38.1	0.14

6.4.3 Evaluating the root crack problem

Actions should be taken to reduce the formation of root flaws and lack of bonding in the dissimilar HYB weld, which have shown to be the factors that determine the strength of the overall weld. Producing welds without any existing flaws or defects are, however, considered an impossibility. It is therefore highly relevant to investigate how the presence of a root crack will affect the structural integrity of the dissimilar Al-Fe HYB weld, and examine how small the crack can be without significantly affecting the tensile properties. Hence, assuring that the weld will fail in the observed weakest point, the HAZ, due to necking. This will provide insight and understanding of the fracture mechanism and the maximum achievable strength of the hybrid weld, and make it possible to build safe constructions with the joining technology in the future.

Due to the configuration of the weld groove and the present of two highly different materials, detection of the total length of the poorly bonded area in the root region was not possible in the microscopic examination. In the following, the FE model will be used to predict the initial length of this region. Figure 6.9 shows the measured force-displacement curves from the DIC analysis (solid line) together with that from the simulation of selected crack lengths (dashed lines). As can be seen from the figure, the dark blue curve (i.e., a crack length of 0.03 mm) corresponds relatively good with that of the experimental data, whereas an increase in crack length shows larger deviations. Thus, this indicates that the same failure mechanism and strength reduction caused by the observed lack of bonding corresponds to an initial crack close to the Al-Fe bond line with a length of about 0.03 mm. Now, assuming that the simulated and experimental case fails, after the exact same amount of deformation, the indications are that the strength reduction caused by the root crack of 0.03 mm corresponds to the poorly bonded area in the root region of the Al-Fe HYB joint.

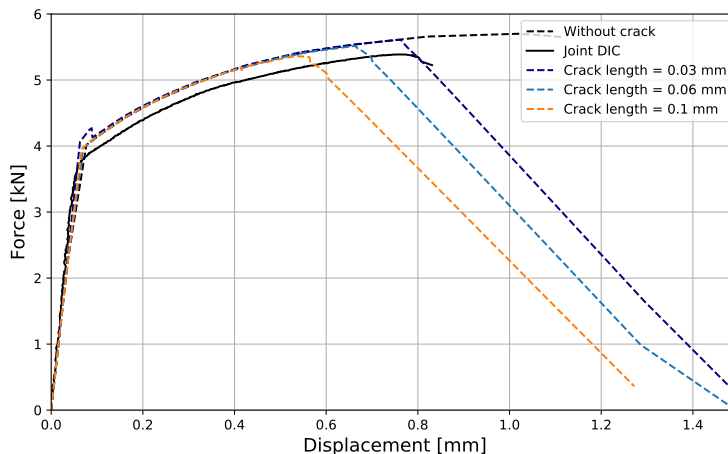


Figure 6.9: Comparison of simulated force-displacement curves (dashed lines) with the measured curve (solid line) from the DIC testing of the Al-Fe HYB joint.

From this, it is reasonable to assume that if perfect bonding is obtained along the entire Al-Fe interface in the HYB joint. The maximum force obtained during tensile testing could be higher, and then the HAZ would be the limiting area of the joint strength. However, in accordance with the simulations, the increase in tensile strength would not be significantly high, but the effect on the overall joint ductility would be beneficial.

Another interesting observation made from the tensile testing of the HYB joint is the point where crack initiation was observed in the DIC pictures. As highlighted in Figure 6.10a, the crack in specimen 2 (shown in Figure 6.10b) was first visible when the force reached a value of 4.96 kN. This is relatively far from the yielding point of the joint and may indicate that there is some kind of partly bonding in the lower region, but that full intermetallic bonding is not obtained. Similar observations were also made for specimen 4, reaching a force of 4.6 kN before the crack could be detected in the DIC pictures.

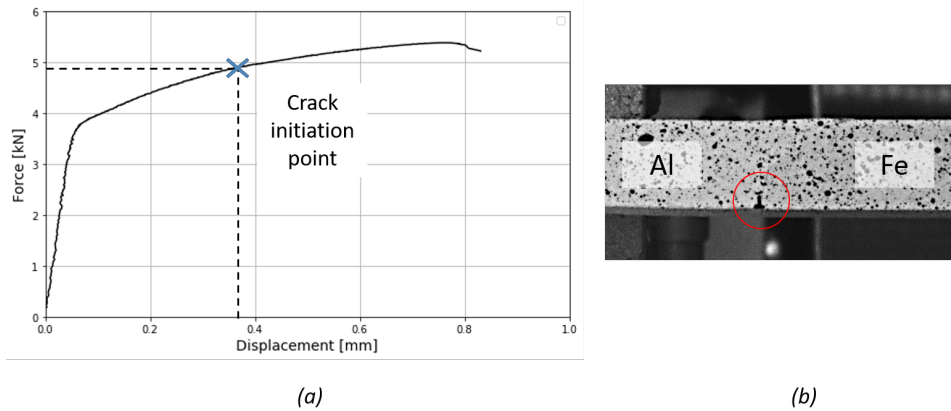


Figure 6.10: (a) The force-displacement curve for specimen 2, indicating at which force and displacement the crack was first initiated during tensile testing. (b) Photograph of the first visible observation of the root crack developing during tensile testing of specimen 2.

6.4.4 Comparison of experimental and simulated crack propagation and strain concentration during tensile testing

For all the different crack sizes used in the simulation, the cracks propagated in a relatively similar manner. The fracture path, however, experienced some minor changes for the different crack sizes. For the small cracks (i.e., 0.03 and 0.06 mm), the propagation direction rapidly shifts from straight upwards towards the steel side of the model. This is shown in Figure 6.11a for a crack size equal to 0.06 mm. For larger crack lengths, the crack goes from propagating upwards to changing more towards the aluminium side of the weld. This is shown in Figure 6.11b for a crack size equal to 0.4 mm. For the largest crack sizes of 0.8 mm and 1.2 mm, the simulations had difficulties converging due to the cracks desire to propagate across the element boundaries in the length direction at the top of the model.

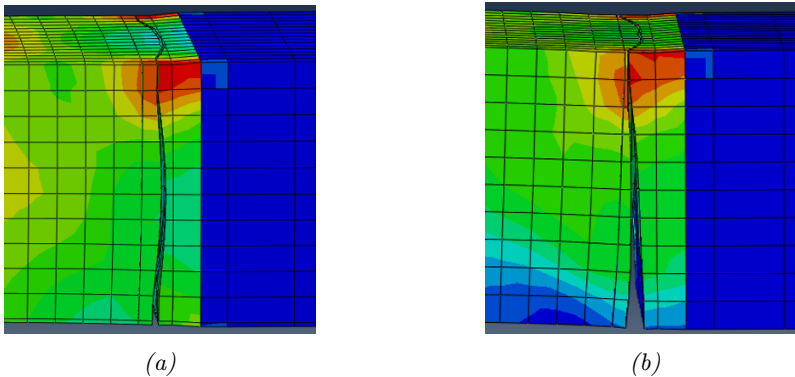


Figure 6.11: Crack path of the simulated Al-Fe HYB joint containing a crack size equal to (a) 0.06 mm and (b) 0.4 mm .

When comparing the different simulated fracture paths, with the observations from the DIC analysis and BSE images, the crack propagation of the smallest crack sizes is most similar to the experimental one. From the BSE images (see Figure 4.24 in Section 4.5) it can be seen that even though the fracture is close to the Al-Fe bond line, it first goes through the aluminium FM, followed by shifting closer to the steel side of the weld. However, the differences in configuration between the simulated and experimental steel surface should be taken into consideration, as the simulation does not have the same machined slope as the actual joint. This can contribute to alter the fracture path and respectively affect the propagation of the crack. Nevertheless, it is seen that using a small crack in the simulation corresponds well with the experimental model, and that the model is also able to capture the crack propagation in a reasonable manner.

Now, a closer look will be given to the principal tensile strain concentration and development, obtained from the simulation and the DIC analysis. This is shown in Figure 6.12 and Figure 6.13, respectively. As can be seen from these figures, in both cases, the strain starts to concentrate in both the HAZ and ahead of the root crack. The competition between the weak areas continues to evolve before most of the strain accumulates close to the crack. Moreover, when the crack propagates (Figure 6.12c) the highly strained area is relatively similar to what was observed in specimen 2 from the DIC analysis, right before failure (Figure 6.13c). From this, it is seen that the FE model is able to capture most of the strain concentrations ahead of the crack tip, but that of the HAZ is not thoroughly rendered. This is mainly believed to be a result of the simplifications made in the FE model, by assuming that the transition between the different zones is straight. In reality, the transition between the Al BM and the HAZ has a slope, as more heat is generated

at the top compared to the bottom during joining. Additional images of the strain concentration and evolution for other crack sizes can be found in Figure I.1 to Figure I.3 in Appendix I. The strain concentration without any presence of a crack is also shown in the same appendix in Figure I.4.

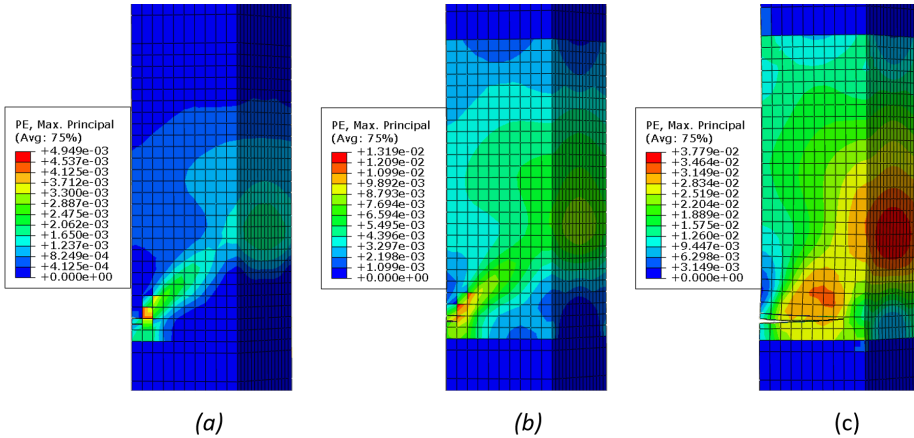


Figure 6.12: Evolution of strain localization and distribution during simulation of the Al-Fe HYB joint with a crack size equal to 0.4 mm. The scaling factor for deformation is set to 1 in the visualization.

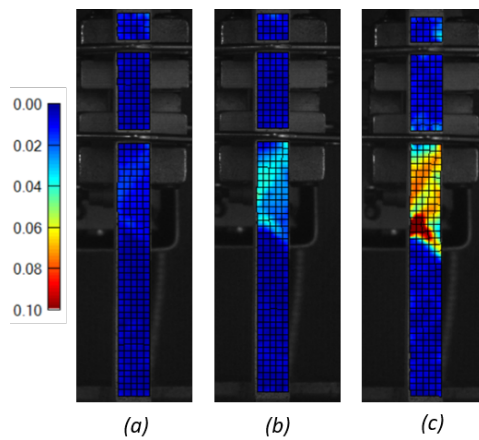


Figure 6.13: Evolution of the strain localization during tensile testing of specimen 2.

6.5 Improvements and current status of the HYB process for joining aluminium and steel

As already mentioned, an average joint efficiency of 75% for the tensile strength was reached for the second generation Al-Fe HYB butt weld. This is significantly higher than the efficiency of 45% obtained for the first produced generation, which shows promising results regarding the changes done in the newer generation with respect to the mechanical properties. The major differences between the two generations are the configuration of the steel side of the weld groove and which side that is the AS and RS of the joint. These differences are schematically illustrated in Figure 6.14. A cooling action during the welding process consisting of CO_2 -gas from the rear, are also added in the newer attempt.

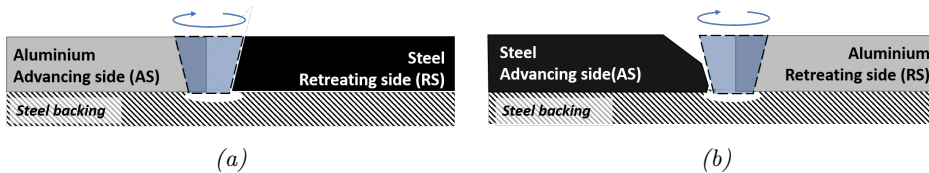


Figure 6.14: Schematic illustration of the pin and its location in the different weld grooves for (a) the first and (b) the second produced Al-Fe HYB butt weld.

Both the hardness measurements and the microscopical investigation of the two welds gave similar results. It could have been expected that the AS would experience a slightly higher peak temperature compared to the RS, and following a lower strength in the HAZ in the first generation. However, from the hardness measurements, there does not seem to be any changes regarding which side that is the advancing and retreating. Moreover, this change may have contributed to more ideal conditions for IMC formation and consequently, higher bonding strength in the newer attempt.

Another reason for the increased strength in the second generation could be the changes in the steel side of the weld groove. The newer configuration resulted in good bonding in the lower part of the Al-Fe interface, while a more discontinuous bonding is believed to be present at the upper part of the interface. Both small scale mechanical interlocking at the lower region and shear forces acting on the upper region can be factors that have contributed positively to the bond strength, since the second generation showed promising results regardless of the existing root flaw.

Recent improvements on the Al-Fe HYB butt weld has been made, and a third generation has been produced. In this generation, the steel side of the weld is not

pre-machined, and does, therefore, consist of a vertical surface, as shown in Figure 6.15. Which side that is the advancing and retreating is similar as for the second generation, but the pin is altered and specially designed for welding of aluminium and steel. The results from the flushed machined tensile specimens showed an average joint efficiency of 90%, which is a significant improvement from the second generation. All the tested specimens fractured in the HAZ on the aluminium side of the weld, which is extremely promising results for the HYB technology.

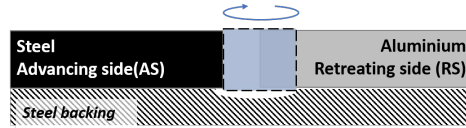


Figure 6.15: Schematic illustration of the pin and its location in the weld groove of the third produced Al-Fe HYB butt weld.

7 Conclusion

7.1 Concluding Remarks

This report gives for the first time an in dept analysis of the structural integrity and microstructure of a dissimilar aluminium (Al) and steel (Fe) butt weld produced by the Hybrid Metal Extrusion & Bonding (HYB) technology. The main conclusions that can be drawn from this investigation can be summarized as follows:

- The HYB PinPoint extruder shows promising results for single pass butt welding of the challenging base material combination of AA6082-T6 and S355. The full-penetration weld is found to be essentially free from internal defects in the weld zone, and displays a very nice surface finish on both sides. However, the microscopic examination of the Al-Fe interface revealed some discontinuities in the weld root region and on the top crown.
- Digital image correlation (DIC) measurements were used to analyse the tensile tested specimens and revealed that most of the strains start to concentrate in the heat affected zone (HAZ) on the aluminium side of the joint. However, due to the formation of a root crack after a certain point during testing, a competition between these two weak zones occurred before the final fracture developed along the Al-Fe interface.
- The dissimilar Al-Fe HYB joint reaches a high joint efficiency of 75%. In comparison, the joint efficiency of friction stir (FS) welds produced using 6xxx alloys and low alloy steels is reported to be about 63%. But, still the HYB joint does not reach as good results as that of an FS weld produced using 5xxx aluminium alloy and high-strength low-alloy (HSLA) steel which achieves a joint efficiency of about 95%.
- The Al-Fe interface was examined by the use of a scanning electron microscope (SEM) and backscatter electrons (BSE) in order to reveal any significant formation of intermetallic phases (IMP) along the interface. Even at the highest possible magnification (10 000x), no sign of any IMP layer was detected, which means that this layer thickness must be below 0.1 μm , which is normally the lower limit that can be detected in standard SEM analysis. This has been confirmed by the work done by Tina Bergh, which has been able to detect an IMP layer thickness of 20 to 40 nm by the use of a high resolution transmission electron microscope (TEM).
- A finite element (FE) model of the HYB joint tensile specimen is developed, using three different elastic-plastic materials (i.e., the aluminium and steel

base materials, and the extrusion zone/heat affected zone) with local properties extracted from the DIC analysis. The model was used to simulate different initial crack lengths close to the Al-Fe interface. It was found that the overall strength and ductility of the joint decreased with increased crack length. If the initial crack exceeded 0.4 mm it would also affect the yield strength properties of the joint.

- Data from the FE simulation of different crack lengths were compared to the experimental data from the DIC analysis. It was observed that the experimental data closely resembled the simulation when introducing an initial crack of length 0.03 mm. This, in turn, caused a strength reduction of 1.6% compared to the simulations of a joint without any initial crack present. Thus, indicating that the observed defects in the Al-Fe HYB joint are not devastating for the resulting tensile properties of the weld.
- Based on the findings in this report, the indications are that the HYB Pin-Point extruder is well suited for joining of dissimilar metals, as aluminium and steel. However, there is a need for further optimization of the process to reach the forefront of aluminium-steel welding. This work is now in progress.

7.2 Recommendations for Further Work

The modeling of the dissimilar Al-Fe HYB weld contains many assumptions in this report. It is therefore suggested that further examination of the newest produced generation of the weld is done to validate the different damage criteria used. A study on how the configuration and size of the mesh in the crack domain effects the crack propagation and initiation, should also be considered to strengthen the credibility of the obtained results. As mentioned, is it not taken into account in the model that the experimental specimens experience mixed mode loading. However, since the newest generation of the Al-Fe HYB butt weld consists of a vertical steel surface, this is no longer needed. The steel base material used in the HYB process should be experimentally tested, to obtain exact material data which can be used as input for the simulation.

Suggestions for making the FE model more complex and representative is to simulate the IMP layer, instead of assuming perfect bonding between the aluminium and steel. This requires that the composition of the IMCs is obtained in addition to its mechanical properties. Due to the extremely thin thickness of the layer, this could be done in collaboration with Tina Berg and the physics department. An additional attempt of the co-simulation can also be considered in the future. This

method can with the right conditions and properties be able to simulate the competition between fracture occurring due to necking or due to a lack of bonding in the Al-Fe interface. A step even further can be to also include the material flow and heterogeneity of the materials in the simulation.

Optimization of HYB process for welding of aluminium and steel is already in progress. Where the newest generation has shown great results. A natural continuation of this work is, therefore, to characterize this weld regarding microstructure and mechanical properties, and compare them to results obtained from the FE simulation. A thorough benchmarking against weldments consisting of the same base materials produced by FSW is also recommended.

References

- [1] United Nations Association of Norway, “Klimaendringer,” <https://www.fn.no/Tema/Klima-og-miljoe/Klimaendringer>, 2018, (Accessed on 05/09/2019).
- [2] W. Miller, L. Zhuang, J. Bottema, A. Wittebrood, P. De Smet, A. Haszler, and A. Vieregge, “Recent development in aluminium alloys for the automotive industry,” *Materials Science & Engineering A*, vol. 280, no. 1, pp. 37–49, 2000.
- [3] N. Çömez and H. Durmuş, “Consideration of cold metal transfer welding of AA5754 to galvanized steel from mechanical and microstructural aspects.” *Revista de Metalurgia*, vol. 54, no. 1, p. 115, 2018.
- [4] T. Sakiyama, Y. Naito, Y. Miyazaki, T. Nose, G. Murayama, K. Saita, and H. Oikawa, “Dissimilar Metal Joining Technologies for Steel Sheet and Aluminum Alloy Sheet in Auto Body,” *Nippon Steel Technical Report*, vol. 103, pp. 91–97, 2013.
- [5] N. Kumar, R. S. Mishra, and W. Yuan, *Friction stir welding of dissimilar alloys and materials*. Oxford: Butterworth-Heinemann, 2015.
- [6] K. Martinsen, S. J. Hu, and B. E. Carlson, “Joining of dissimilar materials,” *CIRP Annals - Manufacturing Technology*, vol. 64, no. 2, pp. 679–699, 2015.
- [7] R. Kovacevic, M. M. Atabaki, P. Chenier, M. Harooni, J. Ma, and M. Nikodinovski, “Welding of Aluminum Alloys to Steels: An Overview,” *Journal for Manufacturing Science and Production*, vol. 14, no. 2, 2014.
- [8] M. Pouranvari, “Critical assessment 27: dissimilar resistance spot welding of aluminium/steel: challenges and opportunities,” *Materials Science and Technology*, vol. 33, no. 15, pp. 1705–1712, 2017.
- [9] S. M. Arbo, T. Bergh, H. Solhaug, I. Westermann, and B. Holmedal, “Influence of thermomechanical processing sequence on properties of AA6082-IF steel cold roll bonded composite sheet,” *Procedia Manufacturing*, vol. 15, pp. 152–160, 2018.
- [10] Ø. Grong, “Recent advances in solid-state joining of aluminum,” *Welding journal*, vol. 91, no. 1, pp. 26–33, 2012.
- [11] L. Sandnes, Ø. Grong, J. Torgersen, T. Welo, and F. Berto, “Exploring the hybrid metal extrusion and bonding process for butt welding of Al–Mg–Si alloys,” *The International Journal of Advanced Manufacturing Technology*, vol. 98, no. 5, pp. 1059–1065, 2018.

-
- [12] Ø. Grong, L. Sandnes, and F. Berto, “A Status Report on the Hybrid Metal Extrusion & Bonding (HYB) Process and Its Applications,” *Material Design & Processing Communications*, p. e41, 2019.
- [13] F. Berto, L. Sandnes, F. Abbatalini, Ø. Grong, and P. Ferro, “Using the Hybrid Metal Extrusion & Bonding (HYB) Process for Dissimilar Joining of AA6082-t6 and S355,” *Procedia Structural Integrity*, vol. 13, pp. 249–254, 2018.
- [14] M. Manfrotto, “Characterization of AA6082-T6 Aluminium alloy and S355 steel welding achieved with the hybrid metal extrusion & bonding [HYB] process,” Master’s thesis, Norwegian University of Science and Technology, NTNU, 2018.
- [15] ABAQUS User’s Manual, “Version 6.11,” *Dassault Systemes Simulia Corp, Rhode Island, USA*, 2012.
- [16] W. D. Callister and D. G. Rethwisch, *Materials science and engineering*, 9th ed. New York: Wiley, 2014.
- [17] G. Mathers, *The Welding of Aluminium and Its Alloys*. Amsterdam: Elsevier Science, 2002.
- [18] R. D. Joseph, *Aluminum and aluminum alloys*. Materials Park, OH: ASM International, 1993.
- [19] J. Dwight, *Aluminium Design and Construction*. Florida: CRC Press Inc - M.U.A., 2002.
- [20] I. N. Fridlyander, V. G. Sister, O. E. Grushko, V. V. Berstenev, L. M. Shevelova, and L. A. Ivanova, “Aluminum Alloys: Promising Materials in the Automotive Industry,” *Metal Science and Heat Treatment*, vol. 44, no. 9, pp. 365–370, 2002.
- [21] W. F. Hosford, *Mechanical behavior of materials*, 2nd ed. Cambridge: Cambridge University Press, 2010.
- [22] D. R. Jones and M. F. Ashby, *Engineering Materials 2: An Introduction to Microstructures and Processing*, 4th ed. Amsterdam: Elsevier Science, 2012.
- [23] Ø. Grong, *Metallurgical modelling of welding*, 2nd ed. London: Institute of Materials, 1997.
- [24] O. Myhr, Ø. Grong, H. Fjær, and C. Marioara, “Modelling of the microstructure and strength evolution in Al–Mg–Si alloys during multistage thermal processing,” *Acta Materialia*, vol. 52, no. 17, pp. 4997 – 5008, 2004.

-
- [25] S. Jindal, R. Chhibber, and N. Mehta, “Issues in welding of HSLA steels,” *Advanced Materials Research*, vol. 365, pp. 44–49, 2012.
- [26] R. Denys, “The effect of HAZ softening on the fracture characteristics to modern steel weldments and the practical integrity of marine structures made by TMCP steels,” *Proc. EVALMAT 89*, vol. 2, pp. 1013–1027, 1989.
- [27] S. Kumai, “Dissimilar-Metal Joining Using Several Types of High-Speed Solid-State Welding Methods,” *Materials Science Forum*, vol. 794-796, no. 1, pp. 357–364, 2014.
- [28] European Aluminium Association and others, “EAA Aluminium Automotive Manual-Joining: Joining dissimilar materials,” 2015.
- [29] F. Campbell, *Joining understanding the basics.*, 1st ed. S.l.: ASM International, 2011.
- [30] H. Ozaki and M. Kutsuna, “Dissimilar metal joining of zinc coated steel and aluminum alloy by laser roll welding,” in *Welding processes*. London: IntechOpen, 2012.
- [31] Ø. Grong, L. Sandnes, T. Bergh, P. E. Vullum, R. Holmestad, and F. Berto, “An analytical framework for modelling intermetallic compound (IMC) formation and optimising bond strength in aluminium-steel welds,” *Material Design & Processing Communications*, p. e57, 2019.
- [32] L. Wang, Y. Wang, P. Prangnell, and J. Robson, “Modeling of Intermetallic Compounds Growth Between Dissimilar Metals,” *Metallurgical and Materials transactions A*, vol. 46, no. 9, pp. 4106–4114, 2015.
- [33] M. Pourali, A. Abdollah-zadeh, T. Saeid, and F. Kargar, “Influence of welding parameters on intermetallic compounds formation in dissimilar steel/aluminum friction stir welds,” *Journal of Alloys and Compounds*, vol. 715, pp. 1–8, 2017.
- [34] E. Schubert, M. Klassen, I. Zerner, C. Walz, and G. Sepold, “Light-weight structures produced by laser beam joining for future applications in automobile and aerospace industry,” *Journal of Materials Processing Technology*, vol. 115, no. 1, pp. 2–8, 2001.
- [35] J. Wloka, H. Laukant, U. Glatzel, and S. Virtanen, “Corrosion properties of laser beam joints of aluminium with zinc-coated steel,” *Corrosion Science*, vol. 49, no. 11, pp. 4243 – 4258, 2007.

-
- [36] U. R. Aakenes, "Industrialising of the Hybrid Metal Extrusion & Bonding (HYB) Method—From Prototype Towards Commercial Process," Ph.D. dissertation, Norwegian University of Science and Technology, NTNU, 2013.
- [37] M. Potesser, T. Schoeberl, H. Antrekowitsch, and J. Bruckner, "The characterization of the intermetallic Fe-Al layer of steel-aluminum weldings," in *EPD Congress*, vol. 1, no. 2006. San Antonio Texas, USA, 2006, p. 167.
- [38] R. Cao, J. Sun, J. Chen, and P.-C. Wang, "Cold metal transfer joining of aluminum AA6061-T6-to-galvanized boron steel," *Journal of Manufacturing Science and Engineering*, vol. 136, no. 5, p. 051015, 2014.
- [39] Y. Zhang, "Arc physics of gas tungsten and gas metal arc welding," *Welding fundamentals and processes: ASM Handbook*, vol. 6, 2011.
- [40] S. Niu, S. Chen, X. Zhang, X. Guo, and G. Wang, "Microstructure and Properties of Lap Joint Between Aluminum Alloy and Galvanized Steel by CMT", journal="Journal of Materials Engineering and Performance," vol. 25, no. 5, pp. 1839–1847, 2016.
- [41] H. Lei, Y. Li, and B. E. Carlson, "Cold metal transfer spot welding of 1mm thick AA6061-T6," *Journal of Manufacturing Processes*, vol. 28, pp. 209 – 219, 2017.
- [42] H. Durmuş and N. Çömez, "Mechanical properties of AA5754 sheets welded by cold metal transfer method," *e-Journal of New World Sciences Academy*, vol. 12, pp. 170–177, 2017.
- [43] F. H. Tranø, "Corrosion Behaviour of Aluminium-Steel Welded Joints," Master's thesis, Norwegian University of Science and Technology, NTNU, 2018.
- [44] C. R. Breivik, "Mechanical Properties of Gas Metal Arc and Friction Stir AA6082-T6 Weldments," Master's thesis, Norwegian University of Science and Technology, NTNU, 2013.
- [45] M. Kang and C. Kim, "Joining Al 5052 alloy to aluminized steel sheet using cold metal transfer process," *Materials & Design*, vol. 81, pp. 95 – 103, 2015.
- [46] N. R. Mandal, "Solid state welding," in *Ship Construction and Welding*. Singapore: Springer, 2017, pp. 221–234.
- [47] K. Ramachandran, N. Murugan, and S. S. Kumar, "Friction stir welding of aluminum alloy AA5052 and HSLA steel: Mechanical and microstructural characterization of dissimilar friction stir welded butt joints," *Welding journal*, vol. 94, no. 9, pp. 291–300, 2015.

-
- [48] S. G. Sajan, M. Meshram, P. S. Pankaj, and S. R. Dey, "Friction stir welding of aluminum 6082 with mild steel and its joint analyses," *International Journal of Advanced Materials Manufacturing and Characterization*, vol. 3, pp. 189–193, 2013.
- [49] P. L. Threadgill, A. J. Leonard, H. R. Shercliff, and P. J. Withers, "Friction stir welding of aluminium alloys," *International Materials Reviews*, vol. 54, no. 2, pp. 49–93, 2009.
- [50] L. Sandnes, "Preliminary Benchmarking of the HYB (Hybrid Metal Extrusion & Bonding) Process for Butt Welding of AA6082-T6 Plates Against FSW and GMA," Master's thesis, Norwegian University of Science and Technology, NTNU, 2017.
- [51] T. Watanabe, H. Takayama, and A. Yanagisawa, "Joining of aluminum alloy to steel by friction stir welding," *Journal of Materials Processing Technology*, vol. 178, no. 1, pp. 342 – 349, 2006.
- [52] M. Ghosh, R. K. Gupta, and M. M. Husain, "Friction Stir Welding of Stainless Steel to Al Alloy: Effect of Thermal Condition on Weld Nugget Microstructure," *Metallurgical and Materials Transactions A*, vol. 45, no. 2, pp. 854–863, 2014.
- [53] S. A. Hussein, A. S. M. Tahir, and A. Hadzley, "Characteristics of aluminum-to-steel joint made by friction stir welding: A review," *Materials Today Communications*, vol. 5, pp. 32 – 49, 2015.
- [54] M. Dehghani, A. Amadeh, and S. A. Mousavi, "Investigations on the effects of friction stir welding parameters on intermetallic and defect formation in joining aluminum alloy to mild steel," *Materials & Design*, vol. 49, pp. 433 – 441, 2013.
- [55] G. E. Dieter, *Mechanical Metallurgy*, SI metric Ed ed. McGraw-Hill, 1988.
- [56] J. Blindheim, Ø. Grong, U. R. Aakenes, T. Welo, and M. Steinert, "Hybrid Metal Extrusion & Bonding (HYB)-a new technology for solid-state additive manufacturing of aluminium components," *Procedia Manufacturing*, vol. 26, pp. 782–789, 2018.
- [57] F. Abbatinali, "Characterization of AA6082-T6 Aluminium Alloy and S355 Steel Welding Achieved with the Hybrid Metal Extrusion & Bonding (HYB) Process," Master's thesis, Norwegian University of Science and Technology, NTNU, 2017.

-
- [58] H. Schreier, J. J. Orteu, and M. A. Sutton, *Image Correlation for Shape, Motion and Deformation Measurements: Basic Concepts, Theory and Applications*. Boston, MA: Springer US, 2009.
- [59] R. V. Kumar, M. Bhat, and C. Murthy, "Evaluation of kissing bond in composite adhesive lap joints using digital image correlation: Preliminary studies," *International Journal of Adhesion and Adhesives*, vol. 42, pp. 60 – 68, 2013.
- [60] E. Fagerholt, "Field measurements in mechanical testing using close-range photogrammetry and digital image analysis," Ph.D. dissertation, Norwegian University of Science and Technology, NTNU, 2012.
- [61] *ASTM E8/E8M-13 Standard Test Methods for Tension Testing of Metallic Materials*. West Conshohocken, PA: ASTM International, 2016.
- [62] K. Bell, *An engineering approach to finite element analysis of linear structural mechanics problems*. Trondheim: Akademika Publ, 2013.
- [63] Y. M. Desai, T. Eldho, and A. H. Shah, *Finite element method with applications in engineering*. Carmel: Pearson Education India, 2011.
- [64] O. Myhr and Ø. Grong, "Novel modelling approach to optimisation of welding conditions and heat treatment schedules for age hardening Al alloys," *Science and Technology of Welding and Joining*, vol. 14, no. 4, pp. 321–332, 2009.
- [65] X. Yun and L. Gardner, "Stress-strain curves for hot-rolled steels," *Journal of Constructional Steel Research*, vol. 133, pp. 36 – 46, 2017.
- [66] J. H. Hollomon, "Tensile deformation," *Aime Trans*, vol. 12, no. 4, pp. 1–22, 1945.
- [67] T. Anderson, "Fracture mechanics : fundamentals and applications," Boca Raton, Fla, 2017.
- [68] S. Kumar, I. Singh, and B. Mishra, "Numerical Investigation of Stable Crack Growth in Ductile Materials Using XFEM," *Procedia Engineering*, vol. 64, pp. 652 – 660, 2013.
- [69] M. Yilmaz, M. Çöl, and M. Acet, "Interface properties of aluminum/steel friction-welded components," *Materials Characterization*, vol. 49, pp. 421–429, 2002.
- [70] T. Berg, S. Arbo, I. Holmestad, and P. Vullum, "The interface between aluminium and steel joined by cold roll bonding and by hybrid metal extrusion and bonding," *Proceedings of the 19th International Microscopy Congress*, pp. 1–5, 2018.

- [71] M. Reza-E-Rabby, K. Ross, N. R. Overman, M. J. Olszta, M. McDonnell, and S. A. Whalen, “Joining thick section aluminum to steel with suppressed FeAl intermetallic formation via friction stir dovetailing,” *Scripta Materialia*, vol. 148, pp. 63 – 67, 2018.
- [72] V. Tvergaard, “Effect of pure mode I, II or III loading or mode mixity on crack growth in a homogeneous solid,” *International Journal of Solids and Structures*, vol. 47, no. 11, pp. 1611 – 1617, 2010.

Appendices

A Material certificates

AA6082 base metal (BM) certificate:

Chemische Zusammensetzung ([%] Gewichtsanteile) / Chemical composition ([%] weight proportion (OES))											
Guss Nr. / cast no.	material	Si	Fe	Cu	Mn	Mg	Cr	Zn	Ti	Sonst Einzel	Sonst Summe
01/0069540/5	EN AW 6082										
	spec. min.	0,7	-	-	0,40	0,6	-	-	-	-	-
	spec. max.	1,3	0,50	0,10	1,0	1,2	0,25	0,20	0,10	0,05	0,15
	actual	0,9	0,45	0,06	0,42	0,8	0,02	0,05	0,02	0,02	0,03

Zugprüfung LT / tensile test LT									
BNr/Los	Zustand	Richtung	Tests	Rm	Rp0.2	A50			
Lot/No.	temper	direction		[MPa]	[MPa]	[%]			
			spec.min.	310	260	10			
			spec.max.	-	-	-			
38911/01	T6	LT	2	from	329	273	18		
38911/01	T6	LT		to	335	277	18		

Sonstige Prüfungen / other tests
Maßkontrolle: OK. / Dimensional Check: OK.
Oberfläche: OK. / Surface inspection: OK.

Figure A.1: Material certificate for the AA6082-T6 aluminium used as base material.

nHZ1CSB eEkJv2CxeHDSstQJbSE9OpB8VQ6chemFRcs8 Page 3 of

SSAB ANALYSEBESCHEINIGUNG COMPOSITO CHIMICO CERTIFICAT СЕРТИФИКАТ АНАЛИЗА																	
										79734K-001	29.08.2016						
										Plavensdata Date Datum Data Data	MLK						
Substanz no. / Cast No. / Schmelzen Nr. / No de oxidan / No Pässe	Koe no. / Test No. / Prüf Nr. / No de oxidan / No Pässe	Profil Item / Pos. / Pos. / Pos. / Pos.	Calv. Ceq. / Ceq. / Ceq. / Ceq. / Ceq.	Analys % / Chemical composition % / Chemisch Zusammensetzung % / Composition Chimique % / Amino massu % / (%)								30.08.2016	MLK				
39204	010	20	067	02	069	010	005	040	014	008	001	028	065	065	009	005	0001

SSAB ANALYSEBESCHEINIGUNG COMPOSITO CHIMICO CERTIFICAT СЕРТИФИКАТ АНАЛИЗА																											
										79734K-001	29.08.2016																
										Plavensdata Date Datum Data Data	MLK																
EN 10 204-3.1 (2004)																											
HIGH STRENGTH FORMABLE STEEL MEETS REQ.OF EN10149-2 S355MC																											
Pos. Item	Substanz, Werkstoff / Cast, Test No.	1. Size / Code	Verfahren / Tempe test								Kalkulation / Eval. Impl.	Hum. No.	Plavens / Tempering														
010	39204	012	TM	K2	20	RP02 / MPa	RP05 / MPa	REL / MPa	REH / MPa	1	REL / MPa	2	3	A %	26	10	200	REH / RM	RM / AD	1	RAZ %	2	3	Kerkerno / Average	32	0	0
K2-32-CENTRE, LONGITUDINAL																											
K3-32-120 MM WIDE BEND TEST																											
TM-THERMOMECH TREATED																											

Figure A.2: Material certificate for the S355 structural steel used as base material.

AA6082 filler metal (FM):

Chemical composition

Si	Mg	Cu	Mn	Fe	Cr	Zr	Ti	B	Others	Al
1.11	0.61	0.002	0.51	0.20	0.14	0.13	0.043	0.006	0.029	balance

Casting method: DC casting

Homogenizing conditions:

Heating rate: ~200°C/h

Holding time at 540°C: 2h 15min

Cooling rate: ~300°C/h

Figure A.3: Material certificate for the AA6082-T4 aluminium wire uses as filler material.

B Results obtained from Matteo Manfrotto

Table 10: Tensile test results obtained from Matteo Manfrotto [14].

Tensile test results from Matteo Manfrotto			
Specimen	Area [mm ²]	Max load [kN]	UTS [MPa]
1	23.82	4.55	191.02
2	23.66	5.38	227.39
4	23.86	5.00	209.56
8	23.85	5.87	246.12
9	22.5	4.93	219.32
14	23.72	4.66	196.46
15	23.78	5.29	222.31

C Additional images of observed defects and steel fragments in the Al-Fe HYB joint

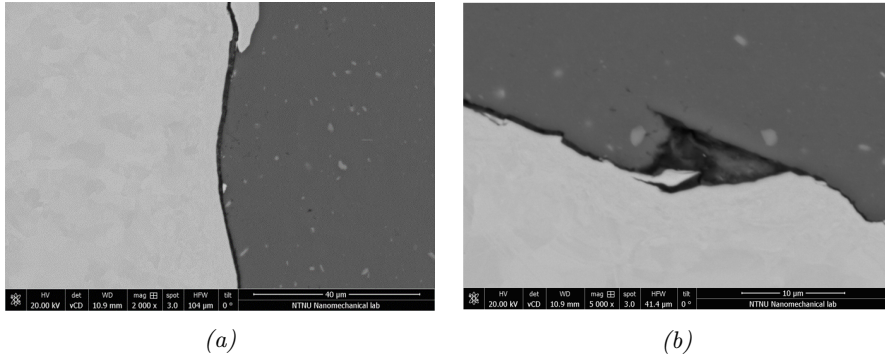


Figure C.1: Additional EBS images of a (a) crack and (b) tunnel defect observed in the Al-Fe HYB weld.

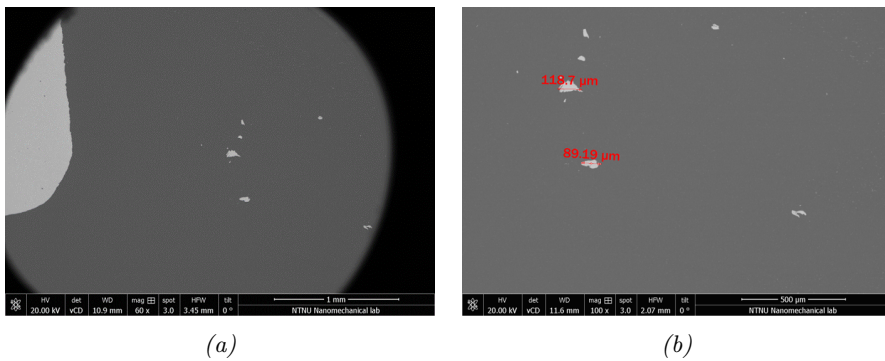


Figure C.2: Additional EBS images of observed steel fragments at (a) low (50x) and (b) higher (100x) magnification.

D Tensile properties

D.1 Global properties of the dissimilar Al-Fe HYB joint.

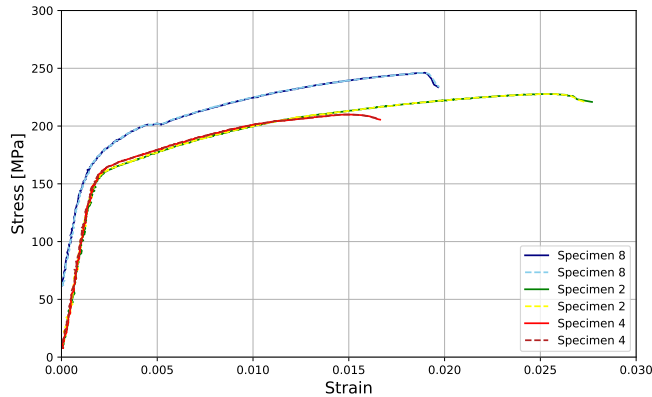


Figure D.1: Stress-strain curves from the DIC tensile testing for all virtual extensometers. These curves are used to calculate the global E -module and 0.2% offset yield strength of the dissimilar HYB joint.

Table 11: Calculated values for the E -module of the Al-Fe HYB joint.

Modulus of Elasticity	
Specimen	E [GPa]
2	80.16
4	90.60
8	77.42
Mean values	82.73

Table 12: Measured tensile properties of the Al-Fe HYB joint.

Tensile Properties [MPa]			
Specimen	Vector	Stress at offset yield	Tensile strength
2	V1	170.04	227.7
	V2	170.04	227.7
4	V1	173.13	210.0
	V2	173.13	210.0
8	V1	201.04	246.18
	V2	201.04	246.18
Mean values		181.4	227.96

D.2 Local properties of the HAZ

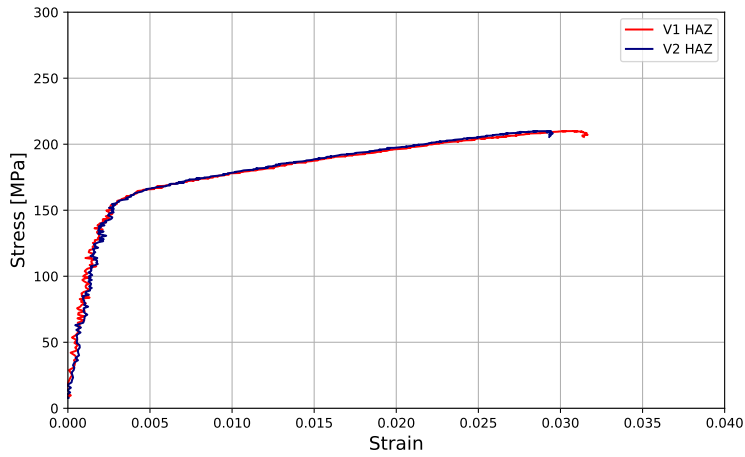


Figure D.2: Stress-strain curves for vectors positioned in HAZ obtained from Specimen 4.

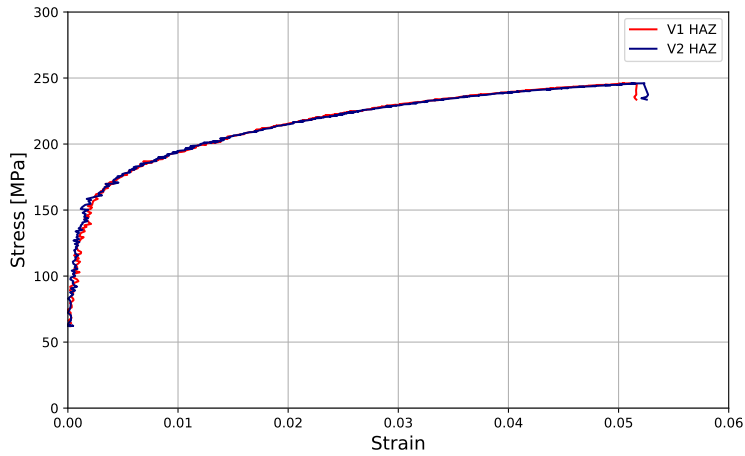


Figure D.3: Stress-strain curves for vectors positioned in HAZ obtained from Specimen 8.

Table 13: Measured tensile properties of the HAZ.

Tensile Properties [MPa]			
Specimen	Vector	Stress at offset yield	Tensile strength
2	V1	164.17	227.7
	V2	165.34	227.7
4	V1	168.85	210.0
	V2	167.76	210.0
8	V1	180.7	246.18
	V2	182.99	246.18
Mean values		171.64	227.96

Table 14: Calculated values for the E-module of the HAZ.

Modulus of Elasticity		
Specimen	Vector	E(GPa)
2	V1	43.87
	V2	42.46
4	V1	41.69
	V2	46.19
8	V1	43.89
	V2	42.70
Mean value		43.47

D.3 Interaction between the different weld zones.

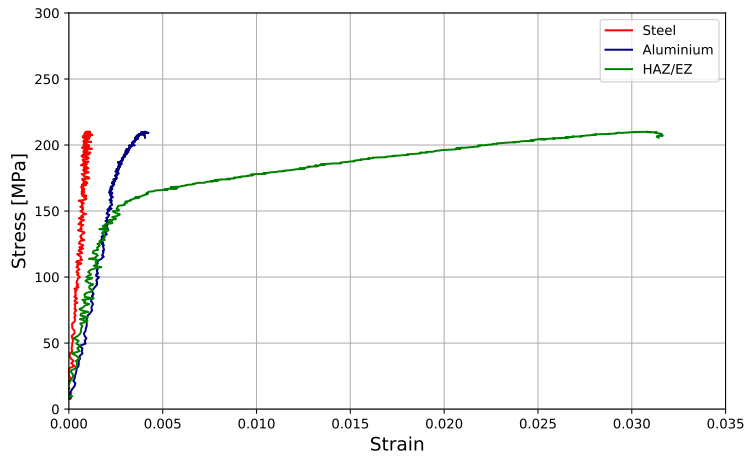


Figure D.4: Measured stress-strain curves during tensile testing of specimen 4, for extensometers positioned in the aluminium BM, EZ/HAZ and steel BM.

E Additional BSE images of the Al-Fe bond line

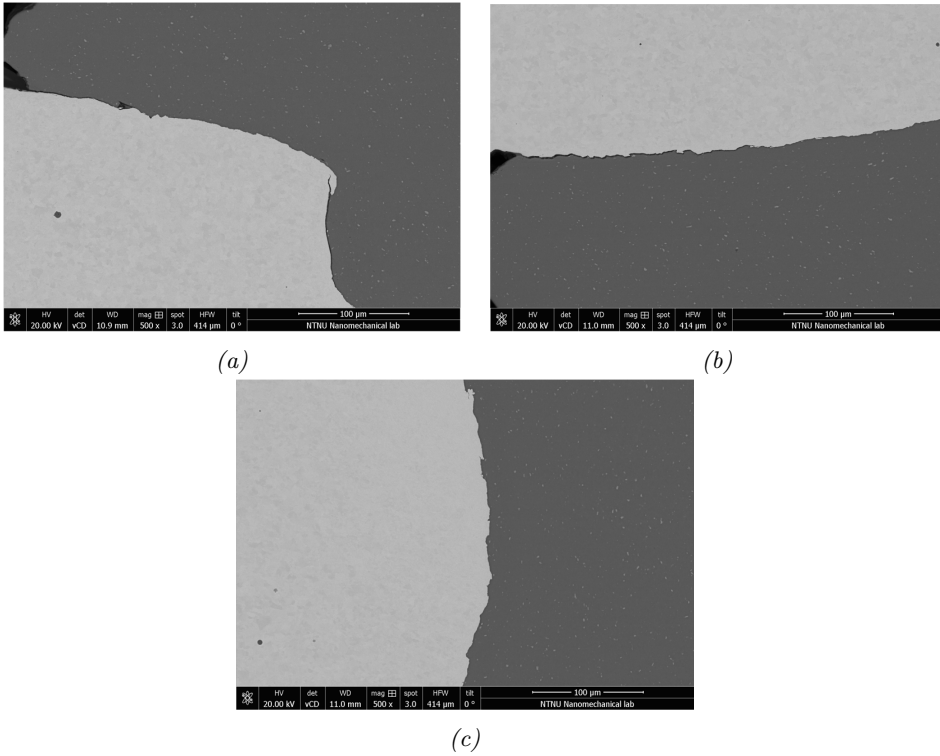
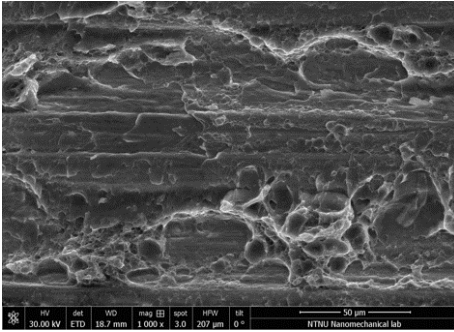
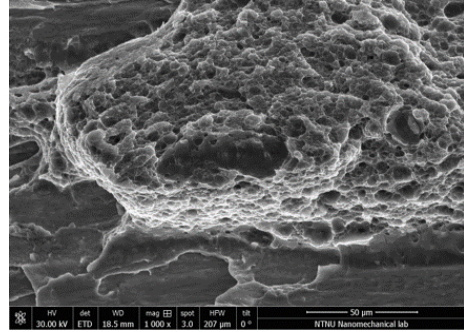


Figure E.1: Additional BSE micrographs at low magnification (500x), showing the (a) top, (b) bottom and (c) middle part of the Al-Fe bond line of the dissimilar HYB joint.

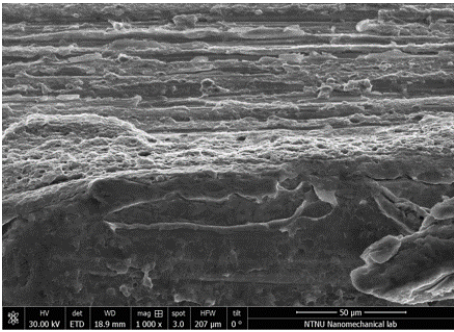
F Additional SEM fractographs



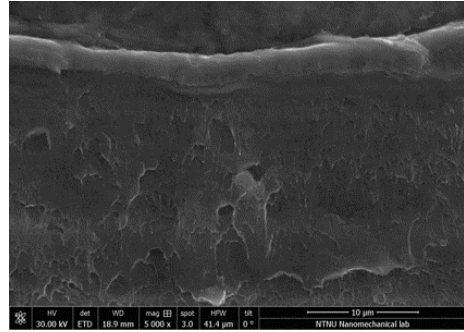
(a) Lower part of specimen 4.



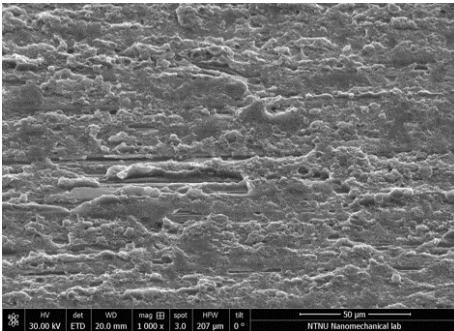
(b) Lower part of specimen 8.



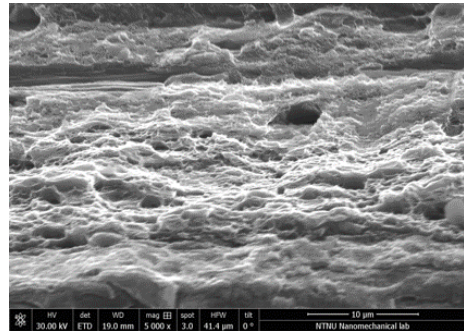
(c) Middle part of specimen 8.



(d) Middle part of specimen 8.



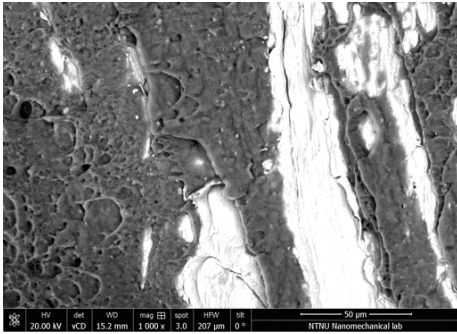
(e) Upper part of specimen 4.



(f) Upper part of specimen 8.

Figure F.1: Additional SEM images of the lower, middle, and upper part of the steel fracture surface at different magnifications.

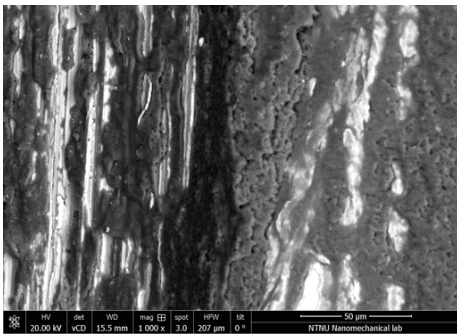
G Additional BSE fractographs



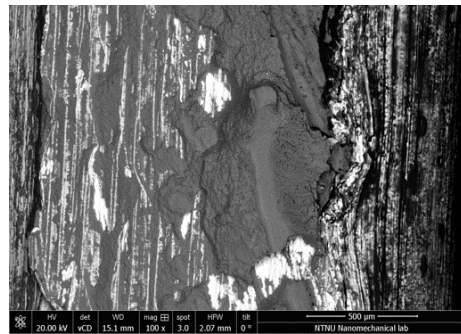
(a) Lower part of specimen 2.



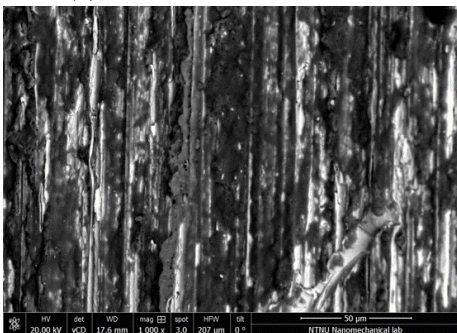
(b) Lower part of specimen 2.



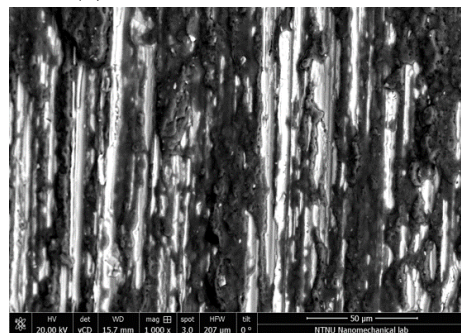
(c) Middle part of specimen 8.



(d) Middle part of specimen 8.



(e) Upper part of specimen 2.



(f) Upper part of specimen 2.

Figure G.1: Additional BSE images of the lower, middle, and upper part of the steel fracture surface at different magnifications.

H Study of crack positioning and crack domain in the FE analysis

The crack was wanted to propagate close to the Al-Fe interface in the aluminium FM, in a similar manner as seen from the DIC analyses and the fractographs of the fracture surface after tensile testing. Therefore, the position of the initial crack was studied to find an optimal distance from the Al-Fe bond line, where the crack propagated close to the interface without going into the steel side of the weld. Two studies regarding the positioning were executed with two different crack lengths. First, the crack size was chosen to 0.4 mm the same length as the element size used for the elements within the EZ, and close to the crack domain. The crack domain was wanted as small as possible and was, therefore, set to 0.4 mm into the aluminium side of the model from the Al-Fe interface. The results are summarized below.

At a distance of 0.1 mm and 0.15 mm away from the interface, as shown in pictures 1 and 2 in Figure H.1, the crack propagated into the steel side of the weld which resulted in extreme deformations of the part and no final fracture. At a distance of 0.2 mm, the crack did not propagate into the steel, but due to the finite crack domain, the element at the top of the model experienced large deformations and no failure, as shown in picture 3. The crack domain was therefore increased to 0.8 mm and resulted in a clean fracture when the crack was positioned 0.2 mm from the Al-Fe interface, picture 3.

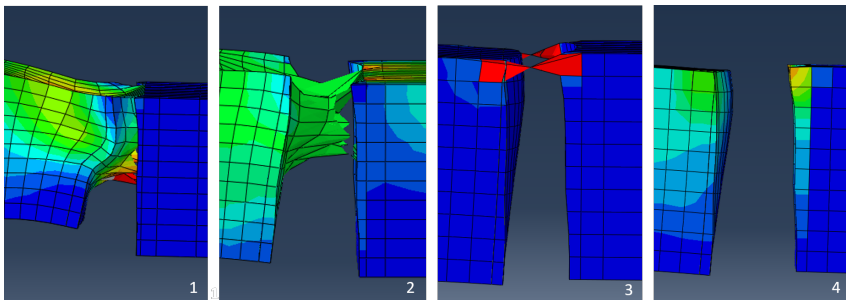


Figure H.1: Crack positioned at different distances from the Al-Fe bond line. 1) 0.1 mm, 2) 0.15 mm, 3) 0.2 mm and 4) 2 mm with increased crack domain.

These initial simulations indicate that the crack needs to be positioned at least 0.2 mm away from the Al-Fe interface. However, when introducing smaller cracks, this will affect the results, and a new study was, therefore, conducted with the same conditions as the previous simulations, but with a crack length of 0.1 mm. The

I. Simulated crack propagation and strain concentration of the Al-Fe HYB joint during tensile testing

results showed that a distance of 0.2 mm was not adequate to prohibit the crack from propagating into the steel, as shown in picture 1 in Figure H.2. 0.3 mm was tried with similar results, see picture 2. 0.4mm is not a possible positioning, as the crack would then be positioned in the element boundary which is not desired during XFEM analysis. At a position of 0.5 mm, the crack would not propagate properly through the surface, and the best location for further simulations was therefore chosen as 0.6 mm into the EZ from the Al-Fe bond line. The results for this position is shown in picture 4 in the figure.

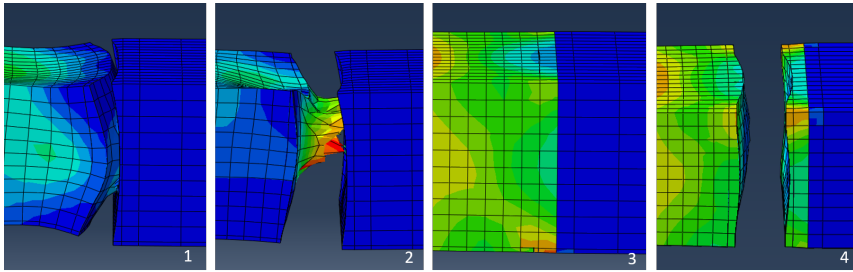


Figure H.2: Crack positioned at different distances from the Al-Fe bond line. 1) 0.2 mm, 2) 0.3 mm, 3) 0.5 mm and 4) 0.6 .

I Simulated crack propagation and strain concentration of the Al-Fe HYB joint during tensile testing

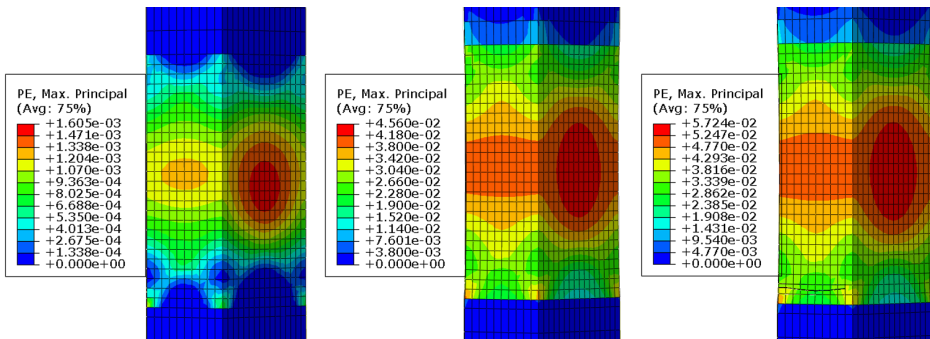


Figure I.1: Evolution of strain localization and distribution during simulation of the Al-Fe HYB joint with a crack size equal to 0.03 mm.

I. Simulated crack propagation and strain concentration of the Al-Fe HYB joint during tensile testing

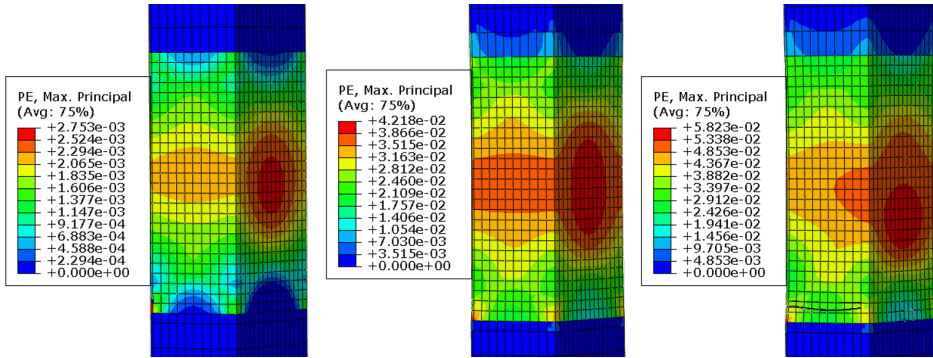


Figure I.2: Evolution of strain localization and distribution during simulation of the Al-Fe HYB joint with a crack size equal to 0.1 mm.

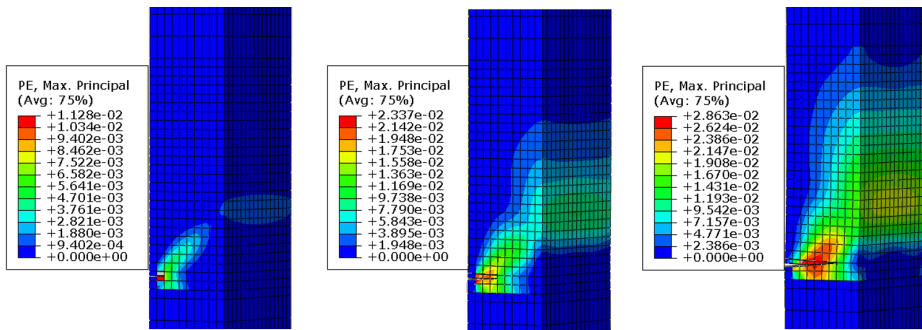


Figure I.3: Evolution of strain localization and distribution during simulation of the Al-Fe HYB joint with a crack size equal to 0.8 mm.

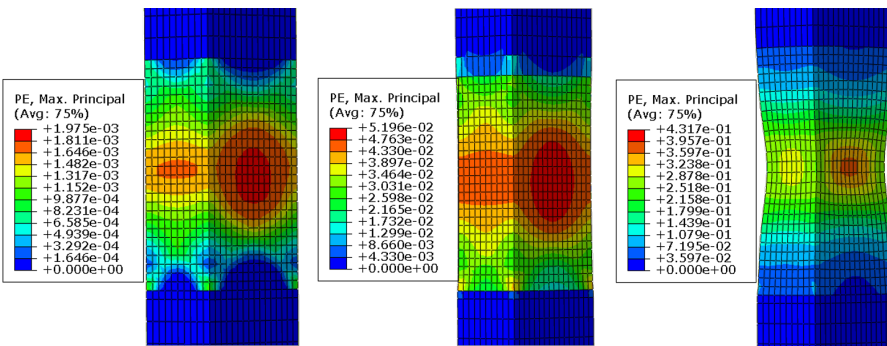


Figure I.4: Evolution of strain localization and distribution during simulation of the Al-Fe HYB joint without crack.

J Risk assessment

NTNU		Prepared by		Date	
		HSE section		09.01.2013	
HSE		Approved by		Replaces	
		The Rector		01.12.2006	
Hazardous activity identification process					



Date: 30.01.19

Unit: Department of Mechanical and Industrial Engineering

Line manager: Torgeir Welo


Participants in the identification process : Filippo Berto (supervisor) and Marie Mathiassen (student)

Short description of the main activity/main process: Master project for student Marie Mathiassen. Metallurgical Characterization and FEM Simulation of a dissimilar Hybrid Metal Extrusion & Bonding (HYB) joint of AA6082-T6 and S355.

Is the project work purely theoretical? (YES/NO): NO

Answer "YES" implies that supervisor is assured that no activities requiring risk assessment are involved in the work. If YES, briefly describe the activities below.

The risk assessment form need not be filled out.

Signatures: Responsible supervisor: 

Student: 

ID nr.	Activity/process	Responsible person	Existing documentation	Existing safety measures	Laws, regulations etc.	Comment
1	Matallurgical Lab.	M.M	Room card.	First aid kit, eye shower, protective gear, handbook.		
1a	Usage of grinding and polishing machines.	M.M	Machine's user manual.	Safety googles and plastic gloves.		
1b	Usage of cutting tools.	M.M	Machine's user manual.	Safety googles and plastic gloves.		
1c	Usage of chemicals.	M.M	Data sheet for chemicals.	Safety googles, plastic gloves and lab coat.		
1d	Usage of microscopes.	M.M	Machine's user manual.			
2	NanoLab.	M.M	Room card.	First aid kit, Protective gear, eye shower.		
2a	Usage of SEM.	M.M	Machine's user manual.	Training in usage of the machine.		

NTNU		Prepared by		Number		Date	
		HSE section		HMSRV2603E		04.02.2011	
HSE/KS		Approved by The Rector				Replaces 01.12.2006	
Risk assessment							
							

Unit: *Department of Mechanical and Industrial Engineering.*


Date: 30.01.19

Line manager: Torgeir Welo

Participants in the identification process: Filippo Berto (supervisor) and Marie Mathiasson (student)

Short description of the main activity/main process: Master project for student Marie Mathiasson. Metallurgical Characterization and FEM Simulation of a dissimilar Hybrid Extrusion & Bonding (HYB) joint of AA6082-T6 and S355.

ID nr:	Activity from the identification process form	Potential undesirable incident/strain	Likelihood (1-5)	Consequence:			Risk Value (human)	Comments/status Suggested measures
				Human (A-E)	Environment (A-E)	Economy/material (A-E)		
1	Metallurgical lab.	Fire	2	C	C	D	D	Locate fire hose, extinguisher, fire blanket, emergency exits. Follow the room rules and use Room card.
		Incorrect usage resulting in damage og equipment.	2	A	B	B	B	Follow the user manual/ machine card. Training an planning ahead.
1a	Usage of grinding and polishing machines.	Cuts on fingers or hand	3	A	A	A	A	Be alert when using the equipment. Be careful when grinding and use plastic gloves.
		Loosing the sample/ flying object	3	A	A	A	A	Same as above.
1b	Usage of cutting tools.	Burning fingers due to hot metal piece after cutting.	2	B	A	B	B	Wait before removing the metal piece after cutting. Always use adequate cooling (fluid) in the machine.
		Smaller cutting injury	3	A	A	A	A	Training and planning ahead. User manuals/machine card. Be careful when using the machines and locate first aid kit.
		Considerable cutting injury	2	C	A	A	C	Same as above.

NTNU		Risk assessment		Prepared by		Number		Date	
				HSE section		HMSRV/2603E		04.02.2011	
HSE/IKS				Approved by				Replaces	
				The Rector				01.12.2006	



1c	Usage of chemicals.	Spilling of dangerous chemicals	3	B	A	A	B	Use protective gear, and read the data sheets carefully. Locate eye shower and first aid kit.
1d	Usage of microscopes.							
2	NanoLab.	Fire	2	C	C	D	D	Locate fire hose, extinguisher, fire blanket, emergency exits. Follow the room rules and use Room card.
		Incorrect usage resulting in damage of equipment.	2	A	B	B	B	Follow the user manual/machine card. Training and planning ahead.
2a	Usage of SEM.	Electrical shock	1	B	A	A	B	Follow the user manual/machine card. Visually inspect the machine before use, and ask for help if uncertain.

Signatures: Responsible supervisor:

Student:

Likelihood, e.g.:

1. Minimal
2. Low
3. Medium
4. High
5. Very high

Consequence, e.g.:



- A. Safe
- B. Relatively safe
- C. Dangerous
- D. Critical
- E. Very critical

Risk value (each one to be estimated separately):

Human = Likelihood x Human Consequence

Environmental = Likelihood x Environmental consequence

Financial/material = Likelihood x Consequence for Economy/material

NTNU	Risk assessment			Prepared by	Number	Date
 HSE/IKS				HSE section Approved by The Rector	HMSRV2603E	04.02.2011 Replaces 01.12.2006
						

Potential undesirable incident/strain

Identify possible incidents and conditions that may lead to situations that pose a hazard to people, the environment and any materiel/equipment involved.

Criteria for the assessment of likelihood and consequence in relation to fieldwork

Each activity is assessed according to a worst-case scenario. Likelihood and consequence are to be assessed separately for each potential undesirable incident. Before starting on the quantification, the participants should agree what they understand by the assessment criteria:

Likelihood

Minimal 1	Low 2	Medium 3	High 4	Very high 5
Once every 50 years or less	Once every 10 years or less	Once a year or less	Once a month or less	Once a week

Consequence

Grading	Human	Environment	Financial/material
E Very critical	May produce fatality/fies	Very prolonged, non-reversible damage	Shutdown of work > 1 year.
D Critical	Permanent injury, may produce serious serious health damage/sickness	Prolonged damage. Long recovery time.	Shutdown of work 0.5-1 year.
C Dangerous	Serious personal injury	Minor damage. Long recovery time	Shutdown of work < 1 month
B Relatively safe	Injury that requires medical treatment	Minor damage. Short recovery time	Shutdown of work < 1week
A Safe	Injury that requires first aid	Insignificant damage. Short recovery time	Shutdown of work < 1day


The unit makes its own decision as to whether opting to fill in or not consequences for economy/materiel, for example if the unit is going to use particularly valuable equipment. It is up to the individual unit to choose the assessment criteria for this column.

Risk = Likelihood x Consequence

Please calculate the risk value for "Human", "Environment" and, if chosen, "Economy/materiel", separately.

About the column "Comments/status, suggested preventative and corrective measures":

Measures can impact on both likelihood and consequences. Prioritise measures that can prevent the incident from occurring; in other words, likelihood-reducing measures are to be prioritised above greater emergency preparedness, i.e. consequence-reducing measures.

NTNU		Risk matrix		Date	
				8 March 2010	
HSE/KS		prepared by		Number	
		HSE Section		HMSRV2604	
		approved by		Page	
		Rector		4 of 4	
				Replaces	
				9 February 2010	



MATRIX FOR RISK ASSESSMENTS at NTNU

		CONSEQUENCE									
Extremely serious	E1	E2	E3	E4	E5						
Serious	D1	D2	D3	D4	D5						
Moderate	C1	C2	C3	C4	C5						
Minor	B1	B2	B3	B4	B5						
Not significant	A1	A2	A3	A4	A5						
	Very low	Low	Medium	High	Very high						
	LIKELIHOOD										

Principle for acceptance criteria. Explanation of the colours used in the risk matrix.

Colour	Description
Red	Unacceptable risk. Measures must be taken to reduce the risk.
Yellow	Assessment range. Measures must be considered.
Green	Acceptable risk. Measures can be considered based on other considerations.